UNIVERSIDAD AUTONOMA DE NUEVO LEON

FACULTAD DE INGENIERIA MECANICA Y ELECTRICA

SUBDIRECCIÓN DE ESTUDIOS DE POSGRADO

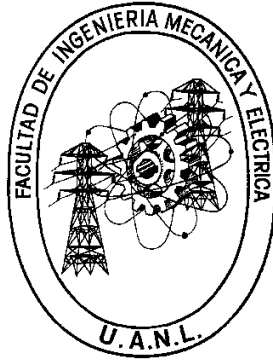**"OPTIMIZATION OF A BATTERY HOUSING AND BATTERY PACK IN AN ELECTRIC VEHICLE THROUGHOUT MULTIDISCIPLINARY ANALYSIS"**

Por:
JAVIER GONZALEZ GONZALEZ

EN OPCIÓN AL GRADO DE:
MAESTRÍA EN CIENCIAS DE LA INGENIERÍA AUTOMOTRIZ

SAN NICOLÁS DE LOS GARZA, NUEVO LEÓN   **[26/06/2025]**

UNIVERSIDAD AUTONOMA DE NUEVO LEON

FACULTAD DE INGENIERIA MECANICA Y ELECTRICA

SUBDIRECCIÓN DE ESTUDIOS DE POSGRADO

"OPTIMIZATION OF A BATTERY HOUSING AND BATTERY PACK IN AN ELECTRIC VEHICLE THROUGHOUT MULTIDISCIPLINARY ANALYSIS"

Por:
JAVIER GONZALEZ GONZALEZ

EN OPCIÓN AL GRADO DE:
MAESTRÍA EN CIENCIAS DE LA INGENIERÍA AUTOMOTRIZ

SAN NICOLÁS DE LOS GARZA, NUEVO LEÓN   **[26/06/2025]**

UNIVERSIDAD AUTÓNOMA DE NUEVO LEÓN
Facultad de Ingeniería Mecánica y Eléctrica
Posgrado

Los miembros del Comité de Evaluación de Tesis recomendamos que la Tesis "Optimization of a battery housing and battery pack in an electric vehicle throughout multidisciplinary analysis", realizada por el estudiante Javier González González, con número de matrícula 1889103, sea aceptada para su defensa como requisito parcial para obtener el grado de Maestría en Ciencias de la Ingeniería Automotriz.

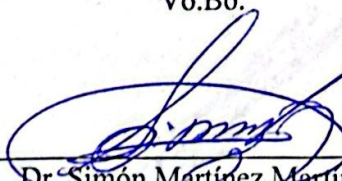**El Comité de Evaluación de Tesis**

Dr. Mario Alberto Bello Gómez
Director

Dr. Oscar Jesús Zapata Hernández
Co-director

Dra. Adriana Salas Zamarripa
Revisor

Dra. Tania Paloma Berber Solano
Revisor

M.C. Yussef Nesme Mendoza
Revisor

Vo.Bo.

Dr. Simón Martínez Martínez
Subdirector de Estudios de Posgrado

Institución ___190001___

Programa _554502_

Acta Núm. _4501_

Ciudad Universitaria, a Junio 2025.

I.   Acknowledgement

II. Dedication

This thesis is dedicated to my wife, Adriana, your unwavering love has been my anchor, your patience my refuge, and your faith in me a guiding light through every challenge. In moments of doubt, it was your belief that carried me forward. You have given me the strength to dream boldly and the courage to turn those dreams into reality. This thesis is as much yours as it is mine, a testament to everything we've built together.

To my family and friends, thank you for your encouragement and understanding. Your constant presence in my life has motivated me to push forward, and I am forever grateful for your love and support.

This work is also dedicated to those who believe in the power of knowledge and innovation, as well as to all those who continue to inspire and challenge me to achieve excellence in every endeavor.

III.   Table of Contents

IV. Figure Table

V. Table Index

VI.   Abstract

Electric vehicles (EVs) have emerged as a crucial solution to reduce environmental pollution and greenhouse gas emissions. However, challenges such as thermal management, structural integrity, and compliance with safety regulations hinder their broader adoption. This thesis focuses on the optimization of battery housing and battery packs in electric vehicles through a multidisciplinary design analysis and optimization (MDAO) approach. By addressing thermal insulation and crash safety concerns, the study develops innovative designs for battery housings that incorporate phase change materials (PCMs) for passive cooling and enhanced structural components for impact resistance. Comprehensive simulations, including finite element analysis (FEA) and design of experiments (DOE), validate the performance improvements. The research demonstrates significant advancements in thermal regulation, structural robustness, and compliance with safety standards, offering a pathway to safer and more efficient electric vehicles.

VII. Summary

The electrification of transportation represents a pivotal shift towards sustainable mobility. However, the design of electric vehicle (EV) battery systems faces significant challenges related to safety, thermal management, and regulatory compliance. This thesis addresses these challenges through the multidisciplinary optimization of battery housings and packs. The research identifies key issues in existing EV battery designs, including inadequate thermal insulation, susceptibility to fire hazards, and failure to meet crash safety standards. To resolve these issues, a design framework is developed that integrates MDAO techniques. The study focuses on optimizing four primary aspects:

1. **Safety Compliance**: Ensuring designs meet Mexican and international regulations.
2. **Weight Optimization**: Reducing the mass of battery housing while maintaining structural integrity.
3. **Mechanical Performance**: Enhancing the design to withstand crash tests and fatigue analysis.
4. **Thermal Management**: Incorporating passive cooling solutions using phase change materials.

The methodology involves reverse engineering of critical components, CAD modeling, and advanced simulation techniques, including FEA and DOE. Various design iterations are evaluated to achieve optimal results for both safety and efficiency. Simulations validate the designs, demonstrating improved thermal stability, impact resistance, and regulatory compliance.

This research contributes to the advancement of electric vehicle technology by providing a comprehensive approach to battery housing design. The findings have implications for manufacturers aiming to enhance the safety, performance, and marketability of electric vehicles while addressing specific regional regulatory and environmental challenges.

1. Introduction

An electric vehicle is a type of transportation powered by electricity, using rechargeable batteries and electric motors. These vehicles produce zero emissions and reduce their environmental impact, resulting in some countries proposing aid or subsidies to people willing to buy one. Due to this, the electric vehicle market is expanding and improving all over the world. This means that new technologies are being developed, increasing the value of electric vehicles, and making them better and more efficient. The other side of this context is that many companies are trying to develop and export much cheaper vehicles in the open market, however, they are taking advantage of the lack of regulations, loopholes in the law, and more tricks to build a much more inexpensive product. The problem arises when the batteries in the vehicles are poorly protected, have a lack of thermal insulation as well as an elevated risk of ignition as shown in many cases in social media. Making a bad reputation in the latest solutions that prevent global climate change, slowing the imminent transition from fossil fuels to electric-powered vehicles.

This thesis proposes a solution for the development of battery housing in a specific electric vehicle that falls into this sensitive category, challenging the actual regulations and laws. By taking advantage of the current technologies and methodologies in the multidisciplinary analysis and optimization area, a design of battery housing was developed, resolving the problem in the thermal management system alongside the safety targets that regulations require.

1.1 Problem

In Mexico, there is a significant challenge in the adoption of electric vehicles. In some cases, foreign models of electric vehicles fail to pass transit regulations, putting them in precarious circumstances. These electric vehicles are correctly categorized as motorcycles rather than cars since they do not meet national safety standards.

Serious issues in the electric vehicle's design are observed, especially in the placement of critical components and their structural elements failing to comply with crash test safety targets established by the Official Journal of the Federation. Furthermore, their maximum

speed of 60 km/h poses challenges to their viability in cities with highways with a 90 km/h limit.

The differences between Mexican regulations and international standards lead to discrepancies in the import and homologation of these electric vehicles. The previously mentioned challenges affect both their potential use and their ability to enter certain market segments, despite their benefits in reducing pollution and promoting sustainability.

For these reasons, research will be conducted to develop a battery housing and a battery pack having in mind 4 major pillars in this project; 1.- Mexican safety standards 2.- Weight optimization 3.- Improvement in mechanical results in simulations (Fatigue analysis, EURO-NCAP & IIHS) 4.- Improvement in current cooling system.

1.2 Hypothesis

By applying a multidisciplinary design analysis and optimization, the location and quantity of a phase change material will be reached alongside the geometry and thicknesses of material profiles in the battery housing structural components. This will improve the thermal management system by absorbing the heat of the batteries in any condition as a passive thermal solution side by side with the enhancement of the general safety of the vehicle.

1.3 Objectives

1.3.1 General objective

- Develop battery housing by using a multidisciplinary design and optimization methodology that integrates both safety and efficiency aspects to ensure the electric system operates within an optimal temperature range and effectively protects critical components.

1.3.2 Specific objectives

- Analyze and identify opportunities within national regulations on electric vehicles for regulated use.
- Reverse engineer most critical parameters and components before modelling the electrical vehicle in a CAD software
- Create a technological mapping of innovations in battery pack cooling systems.

- Determine and design rear, front, and bottom protection systems in the battery housing for the protection of the electric motor and electric vehicle battery.
- Propose a design for the battery pack, implementing a passive cooling system.
- Incorporate a passive temperature control system (BTMS) into the original design of the battery pack housing to complement the active cooling/heating system (PCM/MCF).
- Simulate the proposed design using software to estimate the temperature of LiFePO4 cells, the behavior of the MCF, and the safety of the battery housing/essential components.

1.4 Justification

Electric vehicles have immense long-term benefits for emission reduction policies, increased comfort, and even the improvement of city acoustics. For these vehicles to be implemented globally, they must be able to meet safety regulations and specific climatic conditions in each context they are used.

Regulations are essential for vehicle use and ensuring passenger safety in case of accidents, but they present challenges in design, as they involve increasing the vehicle's mass to absorb collision energy.

To integrate electric vehicles into Mexico's specific climatic conditions, a wide temperature range and extreme conditions must be considered, especially in ecosystems like San Luis Rio Colorado with maximum temperatures of 52.5°C and minimum temperatures of -7°C in states like Durango. This presents problems of thermal insulation and heat dissipation since both electric vehicle batteries and motors must operate within stable temperature ranges of 20°C - 30°C while driving and charging.

These contexts must be considered in the design proposal because, due to the vehicle's characteristics, the motor's capacity, along with the Mexican population's build, impacts the stability, comfort, and safety of the vehicle when traveling on wide avenues with allowed speeds of up to 90 km/h.

1.5 Methodology

The process that will be followed in this work is all aimed at the design and the correct development of battery housing. Starting with the background of the laws and local, federal, and national regulations will give the parameters that the design needs to successfully fulfil. Also, the context and research of the environment that the design will be faced need to be considered. It is included in a flow diagram in Appendix 1

After having the targets, parameters, context, and background in the design, the current technologies need to be researched. The structural components and geometry are crucial for the skeleton of the battery housing, as well as the materials in which each element can be manufactured and produced. This involves the general idea of the manufacturing process of structural pillars, sheet metal, and more components crucial for this product. In the context of the thermal management system, it needs to be researched and the most suitable option for the battery phase change material, considering the flammability, human hazard, and suffocating capabilities.

The preliminary design needs to be tested in a finite element analysis software and analyzed, the intended target is to accomplish the most favorable design by implementing the multidisciplinary design optimization making changes on thickness and materials. This first stage will give us the partial skeleton of the battery housing.

The next stage of the development of battery housing will be implementing the previously researched phase change material. By adding a more complex structure, designing elements capable of containing the phase change material and the best location for it to absorb the most heat and most versatile impact on the longevity and efficiency of the battery.

The final design will be tested in similar conditions for it to be closely analyzed separately from the multidisciplinary optimization methodology for it to be most suitable in the context of the current vehicle, Figure 1.1.
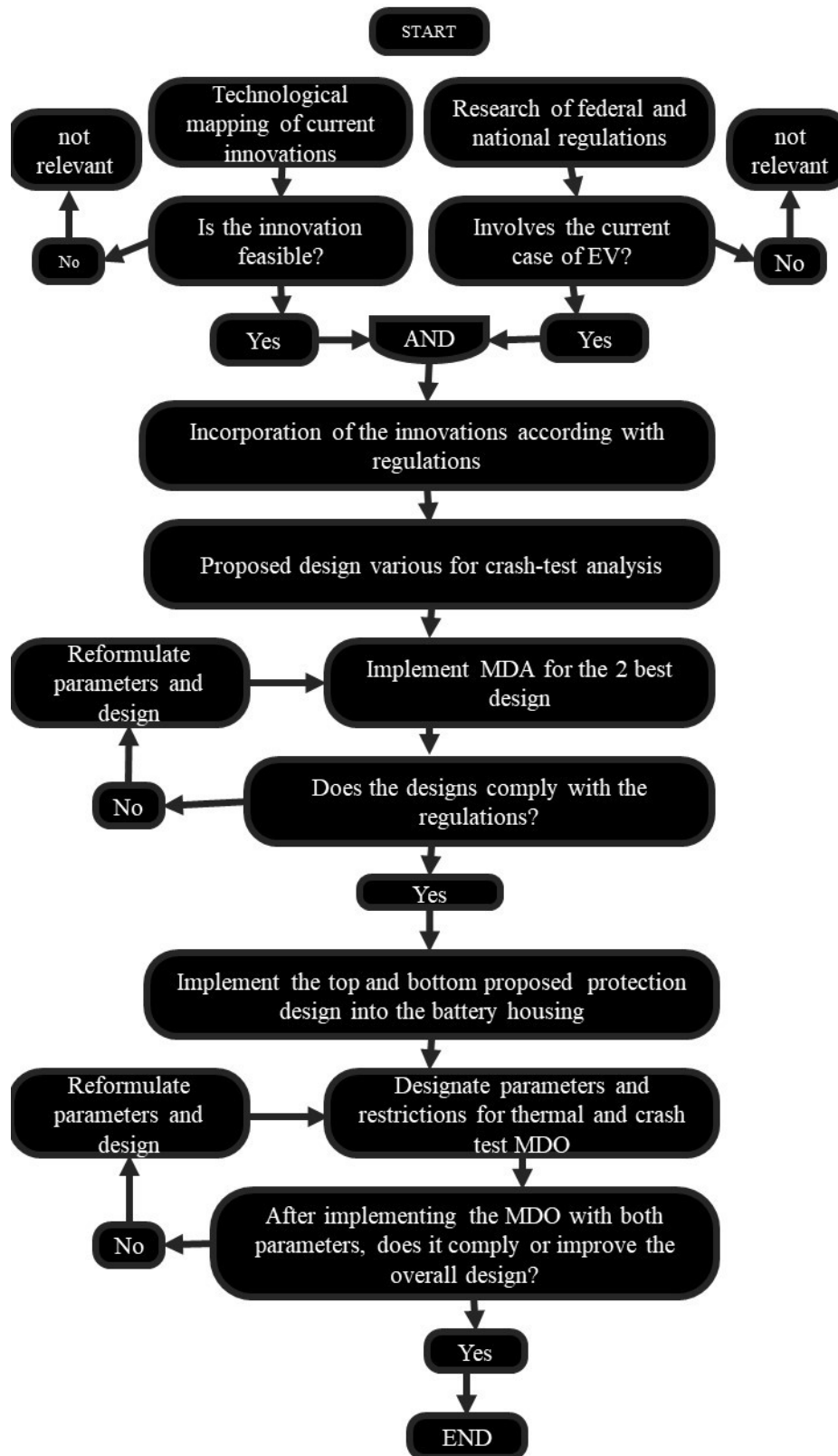
Figure 1.1 - Flow diagram of methodology

2. Conceptual Foundations of FEA, DOE, and MDAO for Electric Vehicle Design

2.1 Electric vehicle

An electric vehicle (EV) is a mode of transportation that relies on electricity as its primary source of power for propulsion, in contrast to traditional internal combustion engine vehicles that use gasoline or diesel. EVs are equipped with electric motors and rechargeable batteries or other energy storage systems to store and deliver electricity to the motor. When an EV is in operation, it draws power from its batteries or an external charging source to drive the wheels, producing zero tailpipe emissions. This shift from fossil fuels to electricity makes EVs more environmentally friendly, contributing to reduced greenhouse gas emissions and air pollution. Electric vehicles come in various forms, including battery electric vehicles (BEVs), plug-in hybrid electric vehicles (PHEVs), and hybrid electric vehicles (HEVs) [1].

2.2 Types

The main difference between electric vehicles on the market is the way the energy is stored or the level at which the electricity powers the vehicle, Figure 2.1 [1]
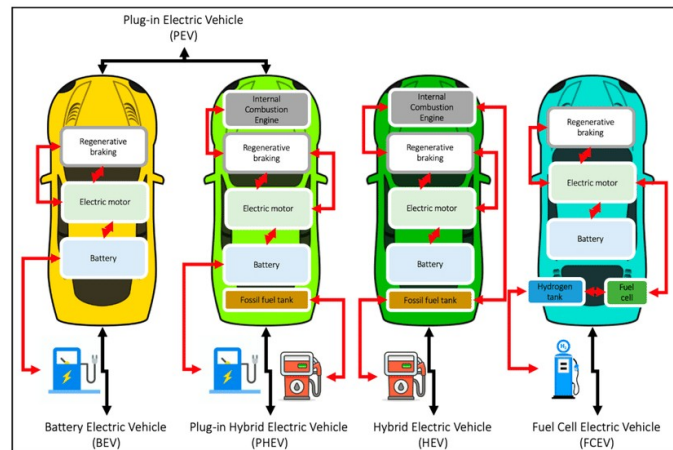
Figure 2.1 - Graphic representation of types of electric vehicles [1]

A Plug-in Electric Vehicle (PEV) is charged externally and can be recharged with a battery or refueled with gasoline or biodiesel depending on the type of engine. The Battery Electric Vehicle (BEV) is exclusively electric. The Plug-in Hybrid Electric Vehicle (PHEV) is

charged externally and can use gasoline or biodiesel. The Hybrid Electric Vehicle (HEV) combines an internal combustion engine and an electric motor. The Fuel Cell Electric Vehicle (FCEV) converts chemical energy into electricity through fuel cell technology.

2.3 Parts of an EV

Electric vehicles consist of several key components that work together to provide propulsion and enable their operation. While there are more than ten critical components, the predominant parts in this case are the following.

2.3.1 Battery Pack:

The battery pack is a collection of lithium-ion or other types of rechargeable batteries that store and provide electrical energy to power the electric motor. The size and capacity of the battery pack significantly influences an EV's range. Here are visual examples of current battery packs in the Audi e-tron Figure 2.2 [2], Chevrolet Bolt Figure 2.3 [3] and Tesla Model S Figure 2.4 [4].
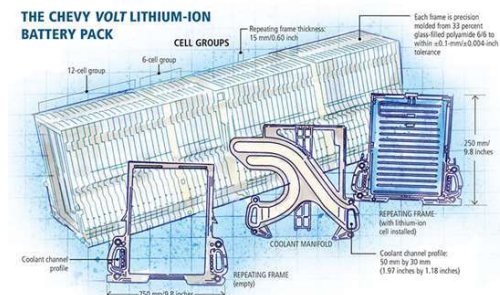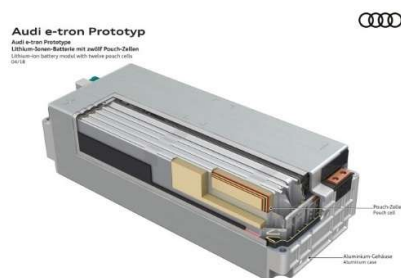
Figure 2.2 - Audi e-tron battery pack [2]   Figure 2.3 - Chevrolet Bolt battery pack [3]

Figure 2.4 - Tesla Model S battery pack [4]

❖ Batteries

Batteries are electrochemical devices that store and release electrical energy using chemical reactions. They consist of one or more electrochemical cells, each containing three primary components: an anode, a cathode, and an electrolyte.

The efficiency, capacity, and performance of batteries are determined by the specific materials used in their construction, the design of the battery, and the conditions under which they operate. Despite the high efficiency of current state-of-the-art batteries, the same problem arises, the thermal management and constant operating temperatures [5].

❖ Behavior of lithium-ion batteries during operating conditions

At the moment of charging, an electrochemical reaction is produced, this is an exothermic process. The heat emission during this process is the reason in most EVs during charging it is turned on the active cooling system, such as fans or other types of cooling. The amount of heat depends on many factors, including the type of battery, the geometry of battery packs, and the type of charging, it is all represented in Table 2.1 [6].

Table 2-1 - Charging types [6]

Power level	Charger location	Typical use	Typical power	Charging time	Connector
Level 1	On-board	Home	2 kW	4–11 h	SAE J1772
Level 2	On-board	Public	20 kW	1–4 h	SAE J1772
Level 3	Off-board	DC Fast	100 kW	< 30 min	CHAdeMO

Depending on the charging type and level it depends on how much thermal stress is applied in the battery cell [6]. As shown in the table, the power level can range from 2 kW to 100 kW. Having this wide range of energy creates a limitation on how much heat can be handled by the thermal management system. It is also worth noting that the time has also decreased from 660 minutes to just 30 minutes.

According to the National Renewable Energy Laboratory, a single cell with an applied voltage of .22 V can generate up to 12.3 W and reach a temperature differential of 12.1°C under 100 Amp discharge in Figure 2.5 [7].
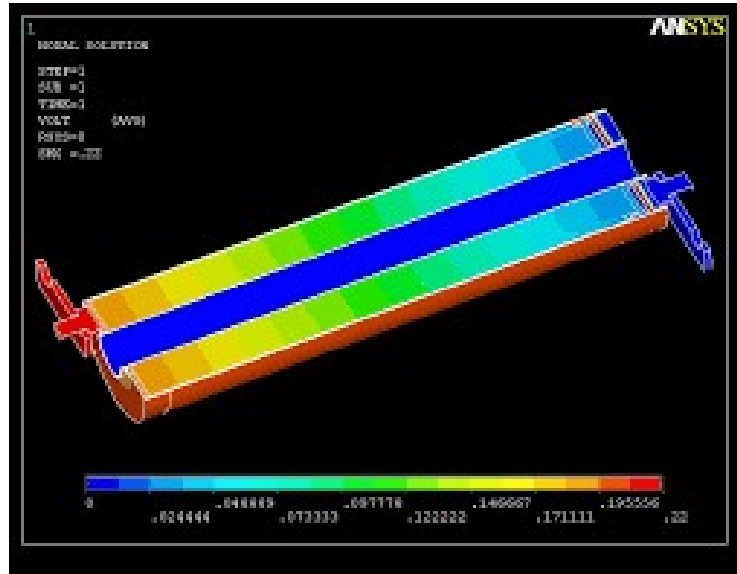
Figure 2.5 - Electrothermal reaction simulation of a lithium-ion battery [7]

This gives a special challenge to the battery thermal management system by adding more stress and requirements to the cooling process. Depending on the charge, as previously mentioned. The heat is generated by electrochemical reactions.

The phenomenon occurs with a similar context in the discharge operation Figure 2.6; however, the most critical and thermally consuming case is faced when the lithium-ion battery is charged in the DC Fast charging type [8].
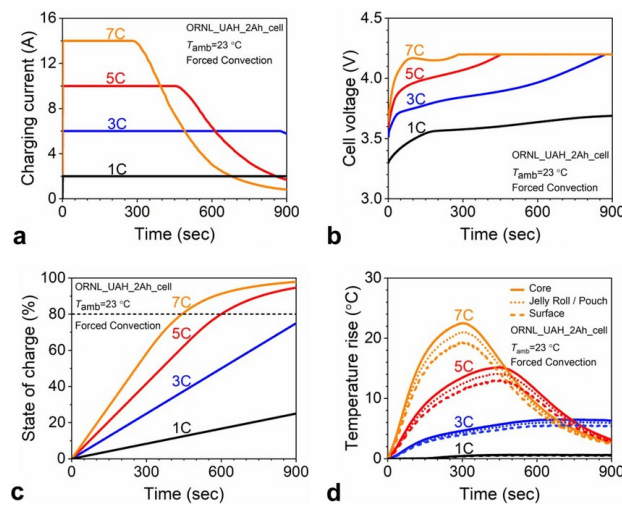
Figure 2.6 - Graphic results of the thermal behavior of a Lithium-ion battery [8]

The current leading solution for addressing the time it takes to charge an electric vehicle involves boosting the battery's energy capacity while minimizing charging durations. This emphasizes the critical importance of heat dissipation and transfer in the design of battery packs and housing.

➢ **Size and geometry**

Manufacturers have their geometry and size of the battery, impacting the overall size of the battery pack and the efficiency of each developer. Here are examples of it, a Tesla battery in Figure 2.7 [9], an Audi battery in Figure 2.8 [10], and in Figure 2.9 the study of cell pouches [11].

Figure 2.7 - Battery cell from Tesla [9]

Figure 2.8 - Battery cell from Audi [10]
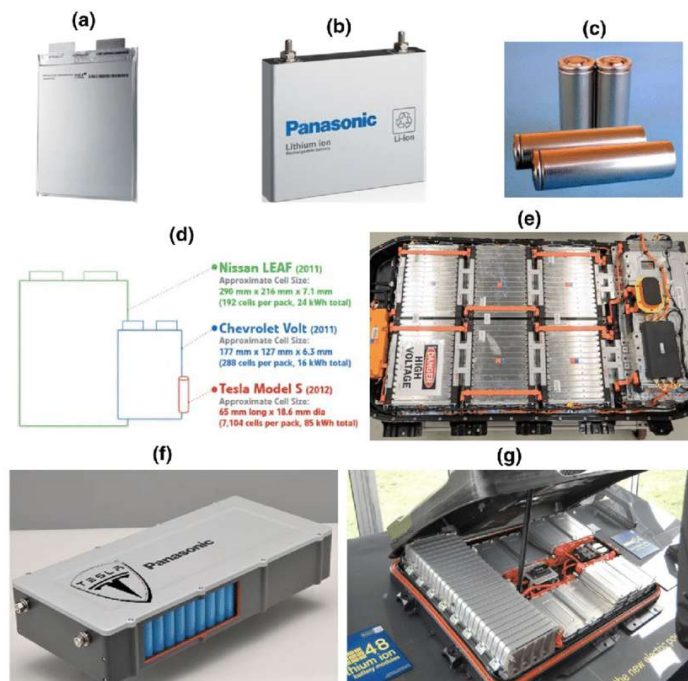
Figure 2.9 - a) Pouch cell b) Prismatic cell c) Cylindrical cell d) General size comparison of cells e) LG Chem in Korea f) Tesla battery pack g) Nissan LEAF battery pack [11]

2.3.2 EV platform:

In any car, two integral components are at the center of a balance in efficiency and safety standards. The body and the chassis need to work together for a vehicle to work efficiently and safely. The bodywork of a car encompasses its external structure, providing aesthetics and protection, while the chassis serves as the internal framework supporting mechanical components and influencing the vehicle's overall performance.

An Electric Vehicle platform is the foundational architecture or design upon which electric vehicles are built. It serves as the basis for constructing various models of electric cars and encompasses the key elements that define the vehicle's structure, performance capabilities, and adaptability to different body styles [12]. It can be divided into:

- Battery housing
- Chassis and frame
- Suspension system
- Axles and drivetrain
- Wiring and Control Units
- Braking System
- Mounting Points for Components

❖ Battery housing

The battery housing carries the task of holding and protecting the battery and electric components, from impacts in any direction. However, this component has more functionalities in the overall electric vehicle.

- Thermal management
- Protection from impacts
- Vehicle stability

❖ Thermal management

The thermal protection that the battery housing can give is by isolating the general process of charging and discharging faces from the battery cells to fully operate passively. If it is not considered, it will impact longevity and efficiency.

In another scenario, it also carries the task of protecting the passage of the vehicle in case of a fire hazard by containing the fire and in design helping extinguish the flames.

❖ Vehicle stability

One of the most impactful tasks is the structural stability that the battery housing gives to the electric vehicle. This directly relies on the manufacturer, depending on them to what degree it is going to give.

❖ Protection from collision

Protecting the battery and internal components from collisions is also critical for the design to be made, independently from the direction of the moving object relative to the vehicle. In the specific case of a frontal or rear impact, the chassis and bodywork of the vehicle will absorb the most energy.

However, a side impact on the vehicle will be the most critical scenario. As the NCAP test provides the constraints and environment on which the test is made, a side pole impact may affect critically the internal structure of a vehicle. In the case of an electric vehicle, battery housing takes a primordial role due to the robust structure and prevents more intrusion than a typical internal combustion engine vehicle, as in the example of Figure 2.10 [13].
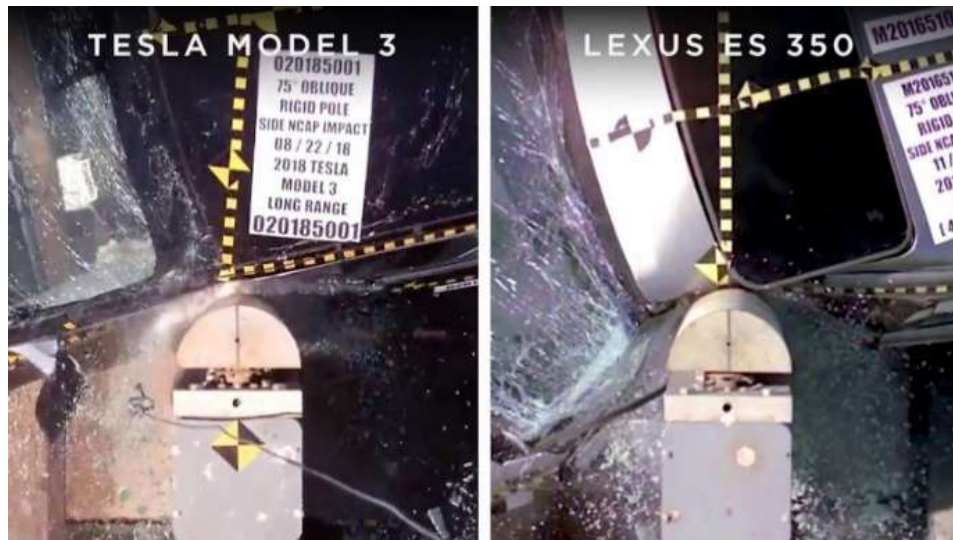
Figure 2.10 - Side-pole crash test comparison between a Tesla Model 3 and a Lexus ES 350 [13]

2.3.3 Skeleton

The skeleton of the battery housing can be split into components that will be developed and analyzed one at a time, as shown in Figure 2.11 [14], these are [15]:

- Upper protection
- Crash structure.
- Battery frame
- Lower protection
- Housing cover

Figure 2.11 - Audi Q4 40 e-tron 77kWh battery [14]

2.3.4 Thermal management system

The thermal management system in an electric vehicle (EV) is a critical component responsible for regulating and maintaining the proper temperature of various vehicle systems, most notably the battery pack. Effective thermal management is essential for the efficient and safe operation of an EV [16].

❖ Active thermal management system

An active thermal management system in an electric vehicle (EV) is a dynamic system that actively regulates the temperature of various vehicle components.

❖ Passive thermal management system

Passive thermal management systems in electric vehicles (EVs) rely on simpler and more passive methods to regulate the temperature of critical components. Mostly used as:

- Air Cooling: Many early and some budget-friendly EVs use air cooling for their battery packs. Air cooling involves using fans or natural convection to dissipate heat.
- Heat Sinks: Some EVs incorporate heat sinks, which are passive devices designed to absorb and distribute heat away from the battery cells.
- Thermal Insulation: Passive systems may include thermal insulation materials to retain heat during cold weather.

2.3.5 Phase change material

Phase change materials (PCMs) in the automotive industry enhance thermal management and energy efficiency. Common types include [17]:

- Paraffin Waxes: Paraffin-based PCMs are a popular choice due to their high latent heat of fusion, which makes them effective at storing and releasing thermal energy.
- Salt Hydrates: Salt hydrates, such as sodium sulfate decahydrate, have high thermal conductivity and can operate at a wide range of phase change temperatures.
- Organic Compounds: Organic PCMs, like fatty acids and alcohols, are known for their biodegradability and non-toxic nature [18].

2.4 Mathematical and numerical modeling

Mathematical and numerical modeling are powerful tools used to represent and analyze complex systems in a wide range of disciplines, from engineering and physics to biology and economics. These models provide a framework for understanding the behavior of systems, predicting their future states, and optimizing their performance. By translating real-world phenomena into mathematical language, we can use the precision and rigor of mathematics to gain insights that might be difficult or impossible to obtain through empirical observation alone.

Mathematical modeling involves the formulation of equations and relationships that describe the system under study. This process often begins with identifying the key variables and parameters that influence the system's behavior. Through a combination of theoretical analysis and empirical data, these relationships are then expressed in mathematical terms, typically as differential equations, algebraic equations, or other types of mathematical expressions.

Numerical modeling, on the other hand, focuses on the implementation of these mathematical models using computational techniques. Given that many mathematical models, especially those involving complex systems, do not have exact analytical solutions, numerical methods provide approximate solutions through computational algorithms. Techniques such as finite difference methods, finite element methods, and computational fluid dynamics are commonly employed to solve these models. Numerical simulations enable us to explore scenarios and perform experiments that would be infeasible or impractical in the real world.

This part of the chapter serves as an introduction to the fundamental concepts and techniques of mathematical and numerical modeling. We will explore the basic principles of model formulation, discuss the importance of model validation and verification, and examine various numerical methods used to solve mathematical models. By the end of this chapter, you will have a foundational understanding of how mathematical and numerical models are developed, analyzed, and applied to solve real-world problems.

2.4.1 Finite Element analysis (FEA)

Finite Element Analysis (FEA) serves as a cornerstone in the computational modeling of engineering systems, offering a robust framework for solving complex physical problems. Central to FEA is numerical modeling, which involves representing a real-world system mathematically to predict its behavior under defined conditions. This approach bridges the gap between theory and practice, allowing engineers to analyze structures, components, and materials without relying solely on experimental methods.

The methodology distinguishes between continuous and discrete systems. A continuous system, such as a beam or plate, is described by continuous functions that govern its behavior across its entire domain. In contrast, FEA discretizes these systems into smaller, finite elements interconnected at nodes, transforming the continuous domain into a discrete representation. This discretization enables efficient numerical computation while maintaining accuracy in approximating real-world phenomena.

A critical step in FEA is meshing, where the domain is divided into finite elements of specific shapes, such as triangles, quadrilaterals, tetrahedrons, or hexahedrons. The quality and refinement of the mesh significantly impact the accuracy and convergence of the analysis. Special attention is required for regions with complex geometries, high-stress concentrations, or rapidly changing gradients, where finer meshes may be necessary.

The analysis relies on governing equations, such as those derived from principles of mechanics (e.g., equilibrium, compatibility, and constitutive laws) or field equations (e.g., heat transfer or fluid dynamics). These equations, typically expressed in terms of partial differential equations (PDEs), describe the physical behavior of the system. Through FEA, these PDEs are converted into a set of algebraic equations, facilitating their numerical solution.

Boundary conditions and material properties play a vital role in defining the problem. Boundary conditions specify constraints on the system, such as fixed supports, applied loads, or thermal conditions, ensuring a realistic simulation of external influences. Material properties, including elasticity, plasticity, thermal conductivity, or density, define how the system responds internally to these external forces or conditions. Accurate representation of these properties is essential to ensure the veracity of the simulation.

2.4.2 Bases

This thesis delves into these fundamental aspects of FEA, exploring how the interplay of numerical modelling, discretization, governing equations, meshing, boundary conditions, and material properties contributes to the accurate and efficient analysis of thermal and crash simulations. By addressing these topics, the research aims to provide a comprehensive framework for leveraging FEA in solving engineering challenges.

Numerical modeling

In modern engineering, numerical simulation plays a critical role, providing solutions and predicting system behaviors without the need for physical experiments. Understanding discrete and continuous systems is essential. Numerical methods primarily rely on discrete models derived from continuous ones. Discretization, the process of transitioning from continuous to discrete systems, streamline computations by focusing on key points of interest [19].

This approach reduces computational complexity and facilitates more efficient analyses. Moreover, the integration of computer-aided engineering tools further enhances efficiency, allowing for the rapid execution of operations within tight timeframes. By leveraging numerical simulation techniques and discretization methods, engineers can tackle complex problems, optimize designs, and make informed decisions with confidence, advancing engineering practices across various domains.

Computational packages utilize numerical methods to solve problems, providing approximate numerical values with good precision, though not exact solutions. These methods employ arithmetic and logical calculations, including arithmetic operations, function calculations, etc. It is worth noting that the precision of the approximation improves as the number of discrete variables increases [20].

Continuous and discrete systems

To have good basic context of numerical modeling, it is necessary to have a solid understanding of discrete and continuous systems, with the discrete system being the one used by simulation methods in engineering as it is generated from continuous systems.

Researcher Alejo Avello from the University of Navarra, Spain, defines in his article titled "Theory of Machines" that discrete systems are those that can be defined by a finite number of degrees of freedom, while continuous systems are those that require an infinite number of degrees of freedom to be exactly defined. For example, the system in Figure 2.12 compares discrete and continuous system state variables. The left graph illustrates a discrete system, where the number of customers in line changes in distinct steps over time. In contrast, the right graph represents a continuous system, showing the smooth variation of water head behind a dam. Discrete systems are common in event-driven processes, while continuous systems describe gradual changes in physical phenomena. Understanding these differences is crucial for selecting appropriate modeling and control strategies. [21].
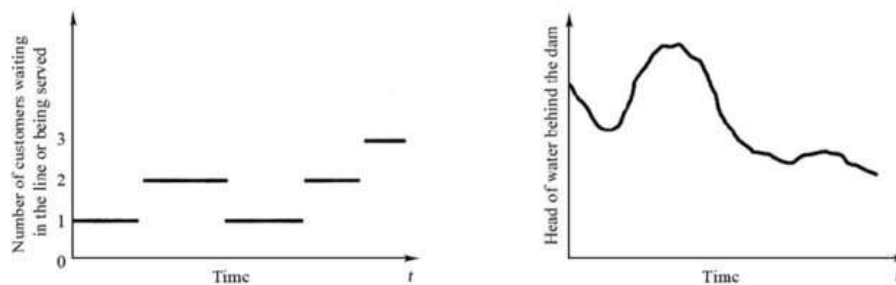
Figure 2.12 - Discrete versus continuous system state variable

In continuous systems, an analytical solution provides an indefinite number of possible solutions. Therefore, in search of a defined or final solution, it can be defined by a type of function which is possible to define a point or area in the domain and use it in a function created to reach a result. Discretization is defined as the process of generating a discrete system from a continuous system.

One of the great advantages of discretization is optimizing the time to carry out the calculations, where it is necessary to know the values of the defined system.

Process of a FEA

One of the main advantages of FEA is its ability to analyze complex geometry, as the elements adapt perfectly to geometry even if it has curvatures. This is the opposite in the Finite Difference Method, where capturing zones, especially curves, in complex geometries is challenging, rendering it inefficient in such cases [22].

Finally, the solution is obtained by solving the system of equations. As mentioned earlier, FEA also allows for the use of different geometries, such as triangles, quadrilaterals for two dimensions, and hexahedra and tetrahedra for three dimensions. This flexibility enables the adaptation of these elements to any geometry, regardless of its complexity[24].

Meshing

Meshing is a fundamental step in the Finite Element Analysis (FEA) process. It involves discretizing a continuous domain into smaller, finite elements to facilitate the numerical solution of complex engineering problems. The mesh represents the geometry of the structure and divides it into discrete parts, where the governing equations can be solved approximately. The accuracy, efficiency, and convergence of an FEA simulation heavily depend on the quality and type of mesh used [25].

The first step in the meshing process is geometry preparation, where the geometric model of the structure is prepared for analysis. This often involves simplifying the model by removing unnecessary features or irrelevant details, such as small fillets, holes, or text. These simplifications help reduce computational complexity while ensuring the results remain accurate. Next, the process involves mesh type selection, where the appropriate element types are chosen based on the geometry and analysis requirements. Common options include 1D elements for beams, trusses, or frames; 2D elements for thin-walled structures like shells or plates; and 3D elements for solid structures with complex geometries. The choice of element type significantly influences the analysis outcome[26].

In the element shape and size definition stage, the shape of the elements—such as triangles, quadrilaterals, tetrahedrons, or hexahedrons—and their size are specified. Fine meshes are used in areas with high stress gradients or intricate features, while coarser meshes may be applied in less critical regions. This balance helps minimize computational costs while maintaining accuracy. Mesh refinement and adaptivity are applied in areas of interest, such as stress concentrations, interfaces, or boundary layers. Adaptive meshing techniques can also be employed, where the mesh is iteratively adjusted based on the solution to improve accuracy in critical regions. This step ensures that areas requiring higher precision are adequately refined. Finally, an element quality check is performed to assess the mesh using metrics such as aspect ratio, skewness, and warping. Poor-quality elements can result in

inaccurate results or convergence issues, so the mesh is optimized to enhance its overall quality. This ensures the reliability and efficiency of the finite element analysis [26].

Types of Meshes

Meshes in finite element analysis (FEA) can be categorized into two main types: structured and unstructured. A structured mesh consists of elements arranged in a regular, grid-like pattern. This type of mesh provides better control over element size and distribution, making it suitable for simpler geometries. However, it can be challenging to apply structured meshes to complex geometries. On the other hand, unstructured meshes are composed of irregularly shaped elements, which allow for greater flexibility in meshing intricate geometries. Despite this advantage, unstructured meshes often require more computational effort to process effectively [27].

The impact of meshing on analysis is significant. Accuracy is directly influenced by the mesh density, as finer meshes provide a better approximation of the geometry and solution. Convergence is another crucial factor; a well-designed mesh ensures stable and convergent results throughout the simulation process. Additionally, the computational cost is heavily dependent on the mesh density, as denser meshes demand greater computational resources and longer processing times. Achieving a balance between accuracy and computational cost is critical for efficient and reliable simulations.

Modern FEA software, such as ANSYS, HyperMesh, and Abaqus, simplifies the meshing process through automated capabilities. These tools offer options for refining meshes, generating adaptive meshes, and evaluating mesh quality. By automating many aspects of mesh generation, engineers can focus on achieving their simulation objectives and interpreting results effectively.

In summary, meshing is a fundamental step that determines the reliability and efficiency of FEA. Proper mesh generation requires careful consideration of the geometry, analysis type, and areas of interest to produce accurate and computationally efficient solutions [27].

Fundamental Equations

Mathematical equations govern the behavior of heat transfer in various media. Key equations include [28]:

- Fourier's Law of Conduction: Describes the rate of heat transfer through a material due to a temperature gradient.

Fourier's Law of Conduction states that the rate of heat transfer through a material is directly proportional to the negative temperature gradient and the thermal conductivity of the material. In mathematical terms, it can be expressed as [29]:

$$q = -h\frac{dT}{dx}$$
<div align="right">Eq. 2.1</div>

Where q is the heat flux, k is the thermal conductivity of the material, T is the temperature, and $\frac{dT}{dx}$ is the temperature gradient (change in temperature per unit length)[30].

- Newton's Law of Cooling: Quantifies the heat transfer between a surface and a fluid by convection.

Newton's Law of Cooling describes the rate at which the temperature of an object changes due to heat loss or gain to its surroundings. It states that the rate of change of the temperature of an object is directly proportional to the difference between its temperature and the ambient temperature. Mathematically, it can be expressed as[30]:

$$q = -h(T - T_\alpha)$$
<div align="right">Eq. 2.2</div>

Where q is the heat flux, T is the temperature of the object, T_α is the room temperature, and h is the film coefficient.

- Stefan-Boltzmann Law: Relates the rate of thermal radiation emitted by a surface to its temperature and emissivity.

The Stefan-Boltzmann Law quantifies the total radiant energy emitted per unit area by a blackbody (perfect emitter and absorber of radiation) as a function of its temperature. It states that the total radiant flux emitted J is proportional to the fourth power of the absolute temperature T of the blackbody [31]:

$$J = \sigma T^4 \qquad \qquad \text{Eq. 2.3}$$

Where σ is Stefan-Boltzmann constant. This laws how all objects emit thermal radiation based on their temperature, influencing fields such as astronomy, climate science, and engineering of thermal radiation devices like infrared heaters and sensors [32].

Boundary Conditions

Thermal boundary conditions define the thermal environment surrounding the system under analysis. They include:

- Dirichlet Boundary Conditions: Specifying the temperature at boundaries or interfaces.

- Neumann Boundary Conditions: Prescribing the rate of heat transfer across boundaries.

- Convection Boundary Conditions: Describing the heat transfer coefficient and fluid properties for convective cooling.

- Radiation Boundary Conditions: Accounting for radiative heat exchange between surfaces.

Properly defining boundary conditions is crucial for accurately simulating real-world thermal behavior [33].

2.4.3 Linear analysis

Linear analysis is one of the foundational methodologies in Finite Element Analysis (FEA), providing a framework for solving problems where the relationship between applied loads and structural responses is linear. This type of analysis assumes that material properties remain constant and that deformations are sufficiently small, ensuring the governing equations do not change during the analysis. Such assumptions make linear analysis suitable for systems that operate within their elastic range, making it an essential tool in engineering and scientific studies [34].

The primary assumption of linear analysis is the linearity of material behavior, where the stress-strain relationship adheres to Hooke's Law, ensuring stress is directly proportional to strain within the material's elastic limit. Additionally, small deformations are assumed, implying that any geometric changes under loading do not significantly alter the structure's

stiffness matrix or the governing equations. Furthermore, boundary conditions and applied loads remain constant throughout the analysis, allowing the solution to be obtained in a single computational step without requiring iterative methods[34].

Linear analysis encompasses several specific types of studies. Linear static analysis focuses on systems subjected to steady or static loads, solving equations to determine displacements, stresses, and strains under these conditions. Modal analysis identifies the natural frequencies and corresponding mode shapes of a structure, ensuring that designs avoid resonance conditions. Harmonic analysis evaluates the response of structures to sinusoidal forces, making it particularly useful in vibration studies. Linear buckling analysis, on the other hand, predicts the critical load at which a structure becomes unstable under compressive forces, assuming ideal geometric conditions.

This approach has broad applications in various engineering fields. In structural design, linear analysis is used to evaluate stresses and deformations in buildings, bridges, and mechanical components under normal operating loads. In aerospace and automotive engineering, it ensures the safety and reliability of materials and systems under typical conditions. Civil engineers utilize it for analyzing foundations, towers, and other critical infrastructure, while mechanical engineers apply it to components like gears, shafts, and brackets[35].

Despite its wide-ranging utility, linear analysis has limitations. It cannot capture material nonlinearities such as plastic deformation, creep, or viscoelastic effects. Similarly, large deformations or rotations violate the assumption of geometric linearity, and changes in boundary conditions, such as those found in contact or friction problems, require nonlinear analysis. Furthermore, while linear dynamic analysis can address steady-state vibrations, it cannot effectively handle transient or shock-loading scenarios.

Modern FEA software, such as ANSYS, Abaqus, and NASTRAN, facilitates linear analysis by providing robust modelling, meshing, and solution capabilities. These tools streamline the process, enabling engineers to evaluate results such as stress distributions and deformation patterns efficiently[35].

Structural mechanics

Mechanical properties are the parameters that indicate their own characteristics of any material, such qualities are linked between the external loads or forces on themselves, this indicates if it can or cannot handle any specific application.

In the following pages, the description of the mechanical properties in metals such as steel and aluminum are found, this will help the better understanding of the general behavior of the general model.

Fundamentals of structural mechanics

Structural mechanics is the branch of mechanics that studies the behavior of structures under various loads and environmental conditions. It provides the theoretical foundation for analyzing and designing structures such as beams, trusses, plates, and shells to ensure their stability, strength, and durability. The core principles are based on equilibrium, compatibility, and material constitutive laws. Equilibrium ensures that the forces and moments act on a structure balance to prevent motion. Compatibility ensures that the deformation of the structure remains consistent with its geometry and boundary conditions. Material constitutive laws, such as Hooke's Law for elastic materials, describe the relationship between stresses and strains within the structure. By employing these principles, structural mechanics enables the calculation of key parameters such as stress, strain, displacement, and internal forces, ensuring structures can withstand their intended loads without failure. Analytical methods, along with numerical techniques like Finite Element Analysis (FEA), are used to solve complex structural problems, making structural mechanics indispensable in engineering disciplines such as civil, mechanical, and aerospace engineering [36].

Material

Mechanical strength is property determines the capacity of any material to support an external load or force without breaking. There are different types of mechanical strength, however the following types have special interest in this thesis:

Tensile Strength is the capacity of a material to handle an external force that stretches the material or to be under tension before breaking. The tensile strength is the required effort for a force or load to break a material, it can be calculated using the next equation 2.4[37]:

$$\sigma = \frac{F}{A}$$ Eq. 2.4

Here, σ (stress) is the force per unit area, F (force) is the applied load measured in Newtons (N), and A (area) is the cross-sectional surface over which the force is distributed, measured in square meters (m^2).

This material property can be found by developing controlled tests and pre-established norms. For this case and interest, the norm ASTM A370 [37], this norm establishes the criteria for the mechanical properties of materials used in the automotive industry for them to be reliable.

Poisson ratio

Poisson's ratio, given by the letter v is a measure of how a material contracts laterally compared to stretched longitudinally, or expands laterally when compressed longitudinally. It is defined as the ratio of transverse strain to axial strain [38].

It can be calculated using the next equation 2.5:

$$v = \frac{-\varepsilon_t}{\varepsilon_a}$$ Eq. 2.5

Elasticity

Elasticity is the property of a material to resist a load, for it to move or deform and after removing the load to recover the initial geometry.

Elasticity studies the relation between the loads applied in a body and the deformation it suffers. The theory on linear elasticity studies the relation between small deformations, applied on solid static elements where the deformation and displacements are lineal. When a static body has a load applied on it and the deformation behaves linearly to the load it is implied that it is a linear elastic behavior[39].

The measurement of this parameter is made by the modulus of elasticity, that is the stablished relationship between the stress and deformation on a material.
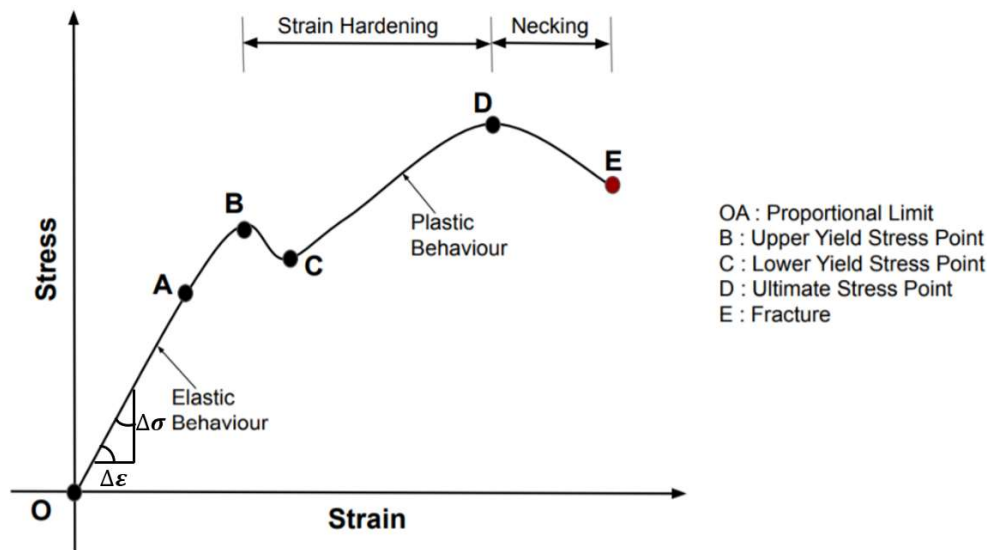
Figure 2.13 - Discrete and continuous systems comparison

A) Elastic modulus

This parameter is calculated through the linear elastic portion of stress against strain, as depicted by the stress-strain graph. However, in plastic materials, especially in rigid plastics, this parameter is difficult to identify directly on the graph, hence it is calculated by dividing stress (σ) by strain (ε). Figure 2.13 shows the straight slope on the elastic behavior, which represents the Young's modulus[40].

The theory of elasticity primarily studies the response of a deformed model under the application of loads or displacements. However, it is a mathematical framework that prevents exact solutions under certain conditions, hence the need for the implementation of approximate numerical methods.

B) Yield point

The yield point is a specific stress level at which a material undergoes a transition from elastic deformation to plastic deformation. It marks the onset of permanent deformation in the material.

Before reaching the yield point, the material deforms elastically, meaning it returns to its original shape when the applied stress is removed. However, once the yield point is exceeded,

the material begins to deform plastically, meaning it undergoes permanent changes in shape or size, even after the stress is removed[41].

C) Ultimate tensile strength (UTS)

The Ultimate Tensile Strength (UTS), also known as tensile strength. It represents the highest point on the stress-strain curve. At the UTS, the material experiences its maximum load-bearing capacity, and any further increase in stress leads to fracture or rupture of the material. UTS is a crucial mechanical property for assessing the strength of materials, especially in engineering and material design applications. It provides valuable information about a material's ability to withstand pulling forces without breaking and is essential for ensuring the structural integrity and safety of components subjected to tensile load.

The main objective of using elasticity theory is to describe the behavior of the deformable model based on a mathematical model that is constructed, with the fundamental unknowns being the displacements of the different points of the model.[42]

This theory is applied in various cases, especially where elementary methods of strength of materials are unable to obtain stress distribution in the analysis element.

D) Fracture point

At the fracture point, the material's internal structure becomes compromised, leading to the propagation of cracks and eventual separation of the material into two or more pieces. This marks the end of the material's ability to withstand further stress and signifies failure.

Stress and deformation.

This relationship between stress and deformations is based on physical experiments, such as tests which are linked to types of tension, compression, and torsion tests. At the beginning of this chapter, a stress-strain diagram was described in which each of the points is mentioned, including the proportional limit. Therefore, these values can be found at the mentioned limit usually when Hooke's law is satisfied, this law is described below in equation 2.6 [43]:

$$\sigma = E\varepsilon_x \qquad \text{Eq. 2.6}$$

The symbol E is known as the Young's modulus. The shear stress is obtained through the following equation 2.7 [44]:

$$\tau = G\gamma \qquad \text{Eq. 2.7}$$

According to the equation, the symbol τ is referred to as the shear stress, for shear deformation, the symbol γ is used, and the symbol G is considered the shear modulus. It is worth mentioning that the shear modulus is also called the rigidity modulus and is typically derived using equation 2.8 [44]:

$$G = \frac{E}{2(1+v)}$$ Eq. 2.8

Therefore, Hooke's law states that within the elastic limit, the deformation produced is proportional to the stress, and it is necessary to consider that this only applies to deformations considered as small strain, that is, until reaching the proportionality limit.[45]

Displacements and strain

The displacement components that occur in a system, the deformations at a point of the system are typically assigned with a series of symbols such as: *u, v, w* to work in conjunction with the *x, y, z* axes. These types of displacements are associated with strain created in the direction of the mentioned axes and shear or angular deformations [45], Figure 3.3.
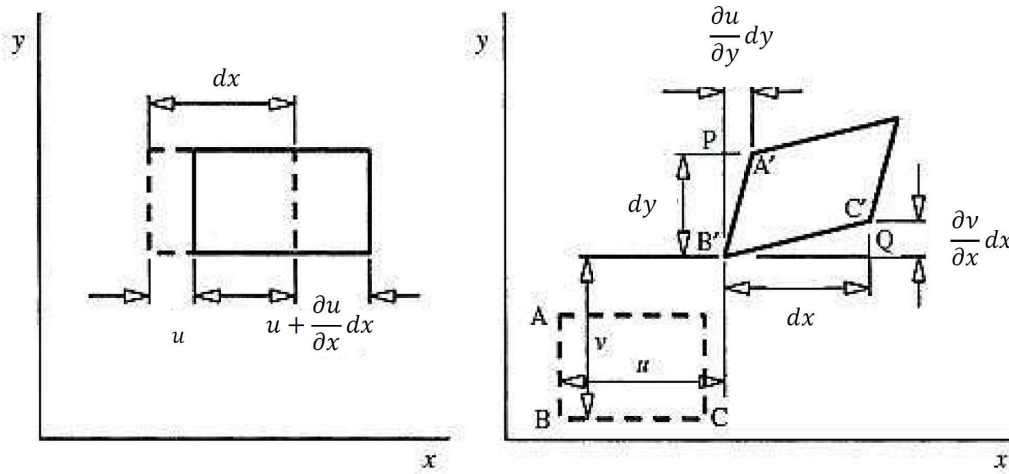
Figure 2.14 - Figure of unitary displacement and displacements

The elements are considered to have very small displacements, which are defined as *dx* and *dy*. The longitudinal displacement in the *x* direction of the element is symbolized by u, and it gradually increases up to $\partial u/\partial x$ in the longitudinal direction of the element, generating a longitudinal strain as shown in the following equation 2.9 [46]:

$$\varepsilon_x = \frac{\left(u+\frac{\partial u}{\partial x}dx\right)-u}{dx} = \frac{\partial u}{\partial x}$$ Eq. 2.9

Similarly, strain can be obtained for the two remaining directions, symbols *v* and *w*, as shown in the following equations [46].

$$\varepsilon_y = \frac{\partial v}{\partial y}$$
<div align="right">Eq. 2.10</div>

$$\varepsilon_z = \frac{\partial w}{\partial z}$$
<div align="right">Eq. 2.11</div>

On the other hand, for shear deformation, considering small angles, it can be described by the following equation 2.12 [46].

$$\gamma_{xy} = \frac{\left(\frac{\partial u}{\partial y}\right)dy}{\partial y} + \frac{\left(\frac{\partial u}{\partial x}\right)dx}{\partial x}$$
<div align="right">Eq. 2.12</div>

Finally, a type of shear deformation is obtained, which can be represented by equations [46], as shown below.

$$\gamma_{xy} = \frac{\partial u}{\partial y} + \frac{\partial v}{\partial x}$$
<div align="right">Eq. 2.13</div>

$$\gamma_{yz} = \frac{\partial v}{\partial z} + \frac{\partial w}{\partial y}$$
<div align="right">Eq. 2.14</div>

$$\gamma_{zx} = \frac{\partial w}{\partial x} + \frac{\partial u}{\partial z}$$
<div align="right">Eq. 2.15</div>

Failure criteria

In the development of failure criteria, it is essential to have knowledge of the properties of materials, for example: the type of geometry and strength. Therefore, material limits are known to estimate the type of stress they can withstand before fracture. Currently, there are failure theories with which permissible stresses in structures or machine components can be determined using formulas. For this, two types of materials are considered in failure theories [47]:

- Brittle materials: these are materials whose elastic deformation period is extremely short and tend to fracture directly upon failure.
- Ductile materials: these are materials that, when one or more forces are applied, tend to deform before failing.

Therefore, for ductile materials, there are two theories to calculate failure or rupture, which are mentioned below:

- Theory of maximum shear stress (Tresca).
- Theory of maximum distortion energy (Von Mises).

Both theories are described below:

The Theory of Maximum Shear Stress (Tresca)

It was developed by engineer Henri Tresca, who mentioned that materials will not yield in the area being analyzed as long as or during the maximum shear stress in the selected area does not exceed the maximum shear stress during a tensile test [48].

Therefore, it represents Tresca's criterion or viewpoint, Figure 2.15:
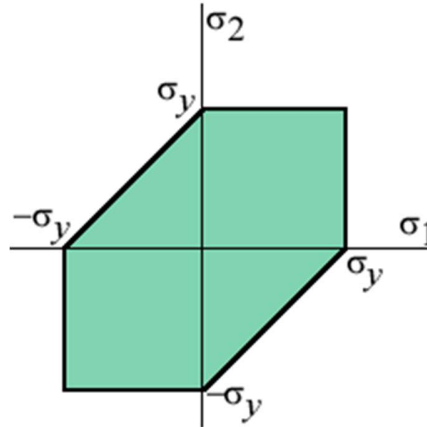
Figure 2.15 - Tresca's graphic representation on failure criteria [28]

Figure 2.15 shows the symbol σ_y, which can represent a yield limit generated by the tensile test, meaning that the material type can exceed the elastic limit based on the limits shown in the graph. It can also be said that these same limits can withstand stresses as long as they remain within the shaded area.

Therefore:

$$\tau_{max} \geq \frac{\sigma_y}{2} \qquad\qquad \text{Eq. 2.16}$$

$$\tau_{min} = \frac{\sigma_1 - \sigma_3}{2} \qquad\qquad \text{Eq. 2.17}$$

The symbol τ_{max} is considered the maximum shear stress of the area under consideration, the symbol σ_1 represents a maximum principal stress, and the symbol σ_3 defines a minimum principal stress [48].

The Theory of Maximum Distortion Energy (Von Mises)

Defined by physicist Richard Von Mises, this theory was developed for materials considered ductile, which can undergo tensile and/or compressive stress. This theory states that the material being used will not flow in the section or area under analysis as long as the distortion energy does not exceed the distortion energy generated by yielding during the tensile test [49]. The following Figure illustrates Von Mises' criterion.
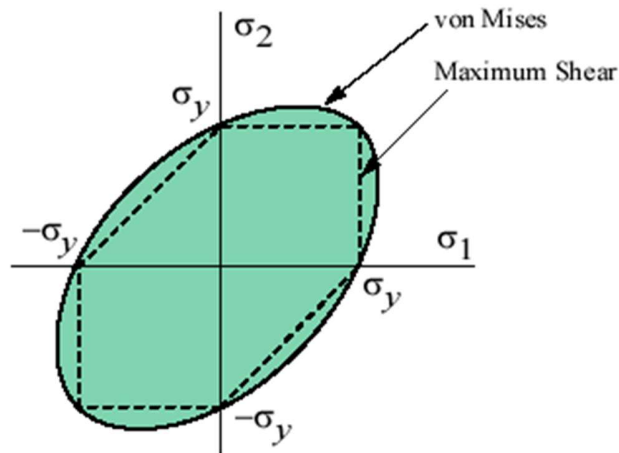
Figure 2.16 - Von Mises' graphic representation on failure criteria [29]

Therefore, the equivalent stress, also known as Von Mises stress, is represented by the following equation 2.18:

$$\sigma_{eq} = \sqrt{\frac{(\sigma_1 - \sigma_2)^2 + (\sigma_2 - \sigma_3)^2 + (\sigma_3 - \sigma_1)^2}{2}}$$ Eq. 2.18

Where:

- σ_{eq} = Equivalent stress or Von Mises stress
- σ_y = Yield stress or yield limit
- $\sigma_1 \geq \sigma_2 \geq \sigma_3$ = Principal stresses

As a reference, for brittle materials, two criteria can be considered, which are outlined in reference.

These are:

- The theory of maximum normal stress or Rankine criterion.
- Mohr's failure theory.
- Mohr – Coulomb

2.4.4 Thermal analysis

Thermal analysis is a crucial aspect of engineering and design across various industries, including aerospace, automotive, electronics, and energy systems. It involves predicting and understanding the behavior of materials and structures under different thermal conditions. Whether it is optimizing the cooling system of a computer processor or ensuring the structural integrity of a spacecraft during re-entry, thermal analysis plays a vital role in ensuring the performance, safety, and reliability of engineering systems [50].

Phase change materials

When a material undergoes phase transitions such as melting, freezing, or vaporization, its behavior and properties change significantly. Here are the fundamental topics regarding material properties for thermal analysis in phase changes:

- Latent Heat: Latent heat is the energy absorbed or released by a substance during a phase change at constant temperature. It represents the energy required to change the material's state without altering its temperature. Latent heat is crucial for understanding phase transitions and predicting the energy requirements for processes like melting, solidification, and vaporization.

- Melting Point and Freezing Point: The melting point is the temperature at which a solid material transitions to a liquid state, while the freezing point is the temperature at which a liquid material transitions to a solid state. These points are important indicators of a material's thermal behavior and stability during phase transitions.

- Boiling Point and Condensation: The boiling point is the temperature at which a liquid material transitions to a vapor state, while condensation is the reverse process where vapor transitions back to a liquid. Understanding these points helps predict how materials behave under heating or cooling conditions and is essential for processes involving evaporation and condensation.

- Heat of Vaporization and Heat of Fusion: These properties represent the amount of energy required to change a substance's state from liquid to vapor (heat of vaporization) or from solid to liquid (heat of fusion). They are critical parameters for calculating the energy requirements and heat transfer rates during phase transitions.

- Phase Diagrams: Phase diagrams illustrate the relationships between temperature, pressure, and the phase of a material. They provide valuable insights into a material's behavior under different conditions, including phase transitions and equilibrium states. Understanding phase diagrams is essential for interpreting thermal analysis results and predicting phase changes accurately.

By considering these properties in thermal analysis, engineers can effectively model and simulate phase transitions, predict material behavior during heating or cooling processes, and optimize designs for various applications, from manufacturing processes to environmental control systems[56] , [57].

Temperature distribution

Temperature distribution refers to the spatial variation of temperature within a material or a structure under thermal loading. Understanding temperature distribution is critical for predicting how different parts of a structure will behave thermally and for ensuring that materials and components perform safely and efficiently. This topic is central to thermal analysis because it provides insight into how heat flows through a system, affecting both its performance and its integrity.

In thermal analysis, the temperature distribution is typically obtained through solving the heat conduction equation 2.19 [58]:

$$\nabla \cdot (k\nabla T) + q = 0 \qquad \qquad \text{eq. 2.19}$$

where T is the temperature, k is the thermal conductivity, and q is the internal heat generation. The solution to this equation provides a map of how the temperature varies across the structure or material, which is crucial for understanding the thermal behavior of the system under consideration.

Heat flux

Heat flux is a critical output in thermal analysis that quantifies the rate of heat energy transfer per unit area. It is measured in watts per square meter (W/m^2) and represents the flow of thermal energy across a surface. Heat flux is essential for understanding the heat transfer

mechanisms in a system, such as conduction, convection, and radiation, and for designing thermal management systems.

Heat flux can be divided into three main types:

- **Conductive Heat Flux**: The transfer of heat through a material without any movement of the material itself. It is proportional to the temperature gradient within the material and its thermal conductivity.
- **Convective Heat Flux**: The heat transfers due to the movement of a fluid (gas or liquid) across a surface. It is characterized by the convective heat transfer coefficient and the temperature difference between the surface and the fluid.
- **Radiative Heat Flux**: The transfer of heat through electromagnetic radiation. This type of heat transfer does not require a medium and occurs across a vacuum. Understanding radiative heat flux is particularly important in systems where surface temperatures are high, such as in aerospace applications.

Heat flux is an essential output in thermal analysis because it provides information on how heat is distributed across the surface of components and helps in evaluating the effectiveness of heat dissipating mechanisms such as fins, heat sinks, or cooling systems. It also plays a crucial role in determining temperature gradients, thermal stresses, and the risk of failure in electronic components, machinery, and other thermal systems [59].

Phase change indicators

Phase change indicators are critical in thermal analysis, particularly for applications involving processes where materials undergo phase changes due to temperature variations. Phase changes, such as melting or solidification, alter the thermal properties of materials, making their behavior under thermal loading different from those that remain in a single phase. Recognizing and modelling phase changes is essential for accurately predicting temperature distributions and heat fluxes in applications like casting, welding, and battery operation.

The presence of phase changes introduces complexity into thermal analysis because the properties of the material change discontinuously during the phase transition. The heat required to change the phase is latent heat, which is not sensed as temperature change but as a shift from solid to liquid or liquid to solid. In thermal models, phase change can be

accounted for by introducing latent heat effects into the heat conduction equation. These indicators are especially important in simulations of materials where the phase change occurs over a significant temperature range, such as in alloys or phase-change materials used in thermal energy storage.

In modelling phase changes, enthalpy-based formulations are often used. The material is considered to have two phases (liquid and solid) within a specific temperature range. As the temperature crosses this range, the enthalpy in the model changes to account for the latent heat. The model can simulate melting and solidification processes, capturing the change in thermal properties and heat fluxes [60].

2.4.5 Non-linear analysis

Nonlinear analysis is an approach used in engineering and physics to study systems or materials where the relationship between input and output is not linear. In linear systems, the response is directly proportional to the input, following principles such as superposition and homogeneity. However, many real-world systems exhibit nonlinear behavior, where small changes in inputs can lead to disproportionately large changes in outputs, or where the relationship between inputs and outputs is not a straight line [61].

In structural analysis, for instance, linear analysis assumes that the material behaves linearly, following Hooke's Law, and that displacements are directly proportional to the applied loads. However, in many cases, such as when dealing with large deformations, nonlinear material behavior, or contact interactions, a linear analysis may not accurately represent the system's response [62].

Nonlinear analysis methods consider these complexities and deviations from linearity. They involve solving sets of nonlinear equations iteratively to determine the system's response under various conditions. Nonlinear analyses can be categorized into several types:

- Geometric Nonlinearity: This accounts for large displacements and rotations that may lead to changes in the system's geometry. It is crucial for analyzing structures subjected to significant deformations, such as those in buckling or large deflection problems.

- Material Nonlinearity: Materials often exhibit nonlinear behavior, such as yielding, strain hardening, or softening. Material nonlinearities must be considered when analyzing structures made of materials like plastic, rubber, or composites.

- Contact Nonlinearity: In systems involving multiple components or bodies in contact, such as assemblies of parts or mechanisms, nonlinearities arising from contact interactions must be addressed. This includes modeling friction, contact forces, and contact constraints.

- Boundary Nonlinearity: This involves considering nonlinearities at the boundaries or interfaces of a system, such as constraints, supports, or boundary conditions that may change with displacement or loading.

Nonlinear analyses are more computationally intensive than linear analyses due to the iterative nature of solving nonlinear equations. However, they provide a more accurate representation of real-world behavior and are essential for designing structures and systems subjected to nonlinear loading conditions or with nonlinear material properties [63].

2.4.6 Dynamic analysis

Dynamic analysis employs various techniques to study structural responses under time-dependent loads [64], [65]:

- Modal Analysis: Identifies natural frequencies, mode shapes, and modal damping ratios.

- Transient Analysis: Examines time-dependent responses to transient loads.

- Frequency Response Analysis: Evaluates structural behavior under harmonic excitations.

- Random Vibration Analysis: Assesses responses to stochastic excitations, such as environmental vibrations.

- Response Spectrum Analysis: Analyzes seismic or shock loads using response spectra.

Equations of Motion

Newton's second law governs dynamic analysis, where forces acting on a body equal its mass times acceleration. These equations are typically second-order ordinary differential equations (ODEs) or matrix equations solved numerically [66].

Key Factors in Dynamic Analysis

Dynamic analysis involves several key factors that determine how a structure or system responds to time-dependent forces.

- Inertial Effects: Mass and acceleration contribute significantly to dynamic response, represented in the mass matrix.
- Damping: Energy dissipation mechanisms, such as structural, material, and viscous damping, influence vibration reduction. Damping ratios quantify these effects [67].
- Time Integration Methods: Techniques like the Newmark and Central Difference methods discretize equations to solve transient responses incrementally [68], [69].
- Excitation Loads: Applied forces, displacements, velocities, or accelerations include harmonic, transient, seismic, impact, and random vibrations [70], [71].
- Response Quantities: Displacements, velocities, accelerations, stresses, and strains provide insight into structural integrity, performance, and safety.

Dynamic analysis is crucial in engineering design and structural assessment, enabling optimized performance and reliability under varying dynamic forces [72], [73].

2.5 Design of experiments (DOE)

The Design of Experiments (DOE) is a systematic and statistical methodology used to plan, conduct, analyze, and interpret controlled tests in order to evaluate the factors that influence a process or system. In the context of engineering and scientific research, DOE plays a pivotal role in optimizing processes, reducing uncertainties, and improving the quality and performance of designs. It is a key tool for making informed decisions when multiple variables are involved, especially when the relationships between these variables are complex and not easily predictable [74].

By utilizing DOE, engineers and researchers can efficiently explore the impact of different factors on system performance, minimizing the number of experiments needed to achieve

reliable results. This approach allows for the identification of significant factors, their interactions, and optimal operating conditions, leading to more effective problem-solving and innovation. DOE is particularly valuable in fields such as mechanical engineering, material science, and thermal analysis, where the interaction of variables like temperature, pressure, and material properties significantly influences system behavior. Its application spans across product design, manufacturing processes, and optimization studies, enabling a deeper understanding of how various factors contribute to system performance and reliability. Through DOE, engineers can validate theories, refine designs, and streamline processes to achieve desired outcomes efficiently[74].

2.5.1 DOE in engineering

DOE allows researchers and engineers to efficiently explore the effects of multiple factors and their interactions on the response variable of interest. By systematically varying the factors according to a predefined experimental design, DOE enables the identification of significant factors, the estimation of their effects, and the optimization of process or product performance.

MELS or "Minimum Levels of Experimental Settings," assumes significance as a foundational aspect in experimental design. Within the framework of DOE, experimental factors represent the variables manipulated deliberately to observe their impact on the response variable(s). These factors typically possess varying levels, indicative of distinct settings or values under examination. The determination of MELS involves establishing the minimum feasible levels at which each factor can be varied during the experiment. This crucial step ensures that the experimental design encompasses a range of variability that is both practically and scientifically meaningful. By defining MELS, researchers strive to strike a balance between the comprehensiveness of the experimental scope and the pragmatic constraints of resources and time. Thus, MELS serve as guiding parameters, facilitating the formulation of experiments that effectively elucidate the relationships between factors and response variables while optimizing the utilization of resources and minimizing experimental complexity [76].

Hammersley sequences represent a class of quasi-random sequences utilized for generating experimental designs. Unlike purely random sequences, Hammersley sequences are

constructed to exhibit low-discrepancy properties, distributing points in a manner that covers the experimental space more evenly. Named after John Hammersley, who introduced them in the context of Monte Carlo integration, these sequences offer advantages in reducing the integration error associated with numerical methods. In the context of DOE, Hammersley sequences find application in the generation of experimental designs, particularly for factorial designs and optimization studies. By employing Hammersley sequences, researchers aim to achieve more efficient and effective exploration of the experimental space, enhancing the statistical properties and robustness of the experimental design. Thus, Hammersley sequences represent a valuable tool in the arsenal of experimental design methodologies, offering enhanced precision and reliability in the pursuit of scientific inquiry and process optimization.

Latin Hypercube Sampling emerges as a powerful technique for efficiently exploring the parameter space of complex systems. This method, originating from Monte Carlo simulation, offers a systematic approach to generating experimental designs that cover the multidimensional input space in a well-balanced and representative manner. Unlike traditional random sampling methods, LHS partitions each input variable into equally probable intervals and then selects a single value from each interval to form a sample point. This ensures that each row and column of the resulting Latin Hypercube matrix contains exactly one sample from each interval, thereby reducing sampling variability and enhancing the coverage of the input space. Latin Hypercube Sampling finds wide application in sensitivity analysis, uncertainty quantification, optimization, and calibration of computational models across diverse fields such as engineering, environmental science, and finance. By leveraging the principles of stratification and randomness, Latin Hypercube Sampling offers researchers a robust and efficient means to explore high-dimensional parameter spaces, facilitating more informed decision-making and enhanced understanding of complex systems [75]

Types of DOE's

There are several types of Design of Experiments (DOE), each suited to different types of research questions and analyses. The main types of DOE include:

Factorial Design

Full Factorial Design: All possible combinations of factors and their levels are tested. This type provides a comprehensive view of all main effects and interactions [77].

$$E_A = \hat{Y}_{hig\ A} - \hat{Y}_{low_A} \qquad \text{Eq. 2.20}$$

Fractional Factorial Design: A subset of the full factorial design that tests only a fraction of all possible combinations to reduce the number of experiments while still providing sufficient information about the factors and their interactions.

Two-Level Factorial Design: Each factor is tested at two levels (low and high). It helps in studying main effects and interactions without the complexity of multiple levels.

Response Surface Methodology (RSM)

Central Composite Design (CCD): Combines factorial and fractional factorial designs with a center point to form a complete second-order model. Useful for finding optimal conditions in multi-factor problems [74].

$$Y = b_0 + \sum b_i x_i + \sum b_{ii} x_i^2 + \sum b_{ij} x_i x_{j_{eq}} \qquad \text{Eq. 2.21}$$

Box-Behnken Design: A type of RSM that allows for the estimation of curvature without having to test all combinations of factors, focusing on building a quadratic model.

$$Y = b_0 + \sum b_i x_i + \sum b_{ii} x_i^2 \qquad \text{Eq. 2.22}$$

Screening Design

Screening Design: Aims to identify the most significant factors among many by evaluating only a subset of factors. It often uses methods like Plackett-Burman designs.

Plackett-Burman Design: An efficient screening design used for identifying important main effects from a larger number of factors.

Taguchi Design

Orthogonal Arrays: A specific type of experimental design that allows the testing of multiple factors simultaneously using a limited number of experiments. It is especially useful for identifying optimal conditions in robust product and process designs.

Signal-to-Noise Ratios: In Taguchi's approach, the Signal-to-Noise (S/N) ratio is used to measure the effect of variability in the experiments, helping in improving product performance under noise conditions [74].

$$S/N = -10 \log_{10}\left(\frac{1}{n}\sum_{i=1}^{n} y_i^2\right)$$

Eq. 2.23

Mixture Design

Simplex-Lattice Design: Used for optimizing the mixture of ingredients. It can handle scenarios where the response depends on the proportions of ingredients.

$$Y = b_0 + \sum b_i x_i + \sum b_{ii} x_i^2 + \sum b_{ij} x_i x_j$$

Eq. 2.24

Simplex-Centroid Design: A type of mixture design that allows for the optimization of the proportions of ingredients to meet a specific response.

Each type of DOE has its own strengths and is chosen based on the research goals, the number of factors, and the level of detail required in the analysis.

2.6 MDAO

Multi-Disciplinary Analysis and Optimization (MDAO) is an advanced engineering methodology that integrates multiple disciplines and domains to achieve optimal performance across a wide range of engineering problems. In the context of complex systems, MDAO addresses the interdependencies and interactions between different physical phenomena, material properties, and system components. This integrated approach allows engineers to consider simultaneously the effects of structural, thermal, fluidic, and electromagnetic factors, among others, on the overall system behavior.

MDAO leverages computational tools and optimization algorithms to explore the design space, perform trade-offs, and identify the best solutions that satisfy multiple objectives and constraints. By simulating and analyzing the system holistically, MDAO helps in understanding the cumulative effects of individual design decisions on the performance of the system as a whole. This capability is crucial in fields like aerospace, automotive, and energy systems, where the interplay between different engineering domains significantly influences the design and performance outcomes. Through MDAO, engineers can achieve a balanced design that meets performance, safety, and cost requirements, thereby improving efficiency, reliability, and sustainability. The integration of MDAO into the design process allows for more informed decision-making and the ability to optimize complex systems with respect to multiple criteria [85].

2.6.1 Regression models

Regression models are crucial tools in data analysis, especially when dealing with complex, multidimensional systems. In HyperStudy, regression techniques are employed for tasks such as model selection, optimization, sensitivity analysis, and performance prediction. These methods allow engineers to approximate the relationship between input variables and system responses, enabling effective decision-making in the design and optimization of complex systems.

FAST (Fit Automatically Selected by Training): The FAST method is an advanced regression technique that utilizes machine learning to automatically select the best-fitting model for a given dataset. It is highly beneficial in streamlining the model selection process and automating the evaluation of different candidate models. This method minimizes prediction errors by assessing multiple models and choosing the one with the best fit, saving time and effort in manual model selection.

LSR (Least Squares Regression): Least Squares Regression (LSR) is a foundational method in statistical modelling that minimizes the sum of squared differences between observed and predicted values. It is particularly useful for modelling linear relationships and is often employed in sensitivity analysis and optimization tasks. The simplicity of LSR makes it computationally efficient, which is advantageous during the initial stages of modelling or when interpretability is crucial[79].

Simple Linear:

$$y = \beta_0 + \beta_1 x + \epsilon \qquad\qquad \text{Eq. 2.25}$$

$$\beta_1 = \frac{\sum_{i=1}^{n}(x_i - \bar{x})(y_i - \bar{y})}{\sum_{i=1}^{n}(x_i - \bar{x})^2} \qquad\qquad \text{Eq. 2.26}$$

$$\beta_0 = \bar{y} - \beta_1 \bar{x} \qquad\qquad \text{Eq. 2.27}$$

Multiple Linear:

$$y = \beta_0 + \beta_1 x_1 + \beta_2 x_2 + \cdots + \beta_k x_k + \epsilon \qquad\qquad \text{Eq. 2.28}$$

$$\hat{\beta} = (X^T X)^{-1} X^T y \qquad\qquad \text{Eq. 2.29}$$

MLSM (Moving Least Squares): Moving Least Squares is a local regression technique that fits the least squares polynomial to subsets of data within a moving window. Unlike global

methods like LSR, MLSM adapts to local variations in the data, making it ideal for situations where the data is noisy or exhibits irregularities. It is commonly used in response surface modeling and optimization, where accurate representation of local optima is important [80].

$$y = \sum_{j=0}^{m} c_j \phi_j(x) \qquad \text{Eq. 2.30}$$

Hyper Kriging (HK): Hyper Kriging is an advanced interpolation method that combines traditional Kriging, a geostatistical method, with machine learning techniques. It is particularly effective in capturing complex relationships and spatial dependencies within the data. This method is commonly used in optimization and sensitivity analysis tasks, as it allows for efficient exploration of complex design spaces with reduced computational effort [81].

$$\hat{y}(x) = \mu + \sum_{i=1}^{n} \lambda_i k(x, x_i) \qquad \text{Eq. 2.31}$$

RBF (Radial Basis Function): Radial Basis Function regression uses radial functions cantered around each data point to model relationships within the data. RBF is particularly effective for non-linear problems where the relationships between variables are complex and multi-dimensional. It is widely used in high-dimensional applications such as heat transfer, fluid dynamics, and structural mechanics, where the data patterns are intricate and challenging to model with traditional methods [82].

$$y(x) = \sum_{i=1}^{n} w_i \phi(\|x - x_i\|) \qquad \text{Eq. 2.32}$$

Each of these regression methods has its strengths and is suited to different applications based on the nature of the data and the goals of the analysis. By selecting the most appropriate regression model, engineers can enhance the efficiency and accuracy of their simulations and optimizations.

Several regression techniques are available, each with unique strengths and applications. Below is an overview of the primary regression models used in HyperStudy, along with a comparative summary of their key features, applications, and advantages [78].

Table 2-2 – Regression models used on the provided software.

Regression Model	Key Features	Applications	Strength
FAST	Automatic model selection using machine learning.	Model selection, optimization, and automated analysis.	Reduces manual effort, adapts to data, streamlines the process.
LSR	Minimizes the sum of squared errors between observed and predicted values.	Sensitivity analysis, optimization, and understanding linear relationships.	Simple, interpretable, and computationally efficient.
MLSM	Local regression technique fitting the least squares polynomial to subsets of data.	Response surface modelling, noisy/irregular data, local optima.	Adapts to local variations, handles noise well, avoids global overfitting.
Hyper Kriging	Combines Kriging with machine learning for advanced interpolation.	Sensitivity analysis, optimization, and handling spatially correlated data.	Handles spatial dependencies, accurate for complex design spaces.
RBF	Uses radial basis functions to model data based on distance from center points.	High-dimensional modelling, heat transfer, fluid dynamics, structural mechanics.	Flexible, handles non-linear relationships, effective for intricate patterns in data.

2.6.2 Required data.

To effectively utilize regression methods in HyperStudy and ensure robust predictive models, several conditions, assumptions, and best practices need to be considered. These aspects are fundamental in achieving accurate predictions and optimizing system performance across various engineering disciplines.

The quality of data is crucial in regression analysis. It is essential to work with complete and clean datasets, free from missing values, outliers, or noise, as these factors can distort the regression results. A balanced distribution of data is also important to avoid biases, while ensuring that multicollinearity is absent among the predictor variables. Multicollinearity, the correlation between independent variables, can undermine the model's reliability by inflating the variance of coefficient estimates, making it difficult to assess the true effect of each predictor.

Equally important are the assumptions underlying regression models. The relationship between the input variables and the response should ideally be linear, but for non-linear relationships, techniques like Hyper Kriging or Radial Basis Functions (RBF) can be used. Another assumption is that residuals, or errors, should be independent of each other, avoiding autocorrelation that could lead to biased estimates. The variance of residuals must remain constant across different levels of predictor variables—a condition known as homoscedasticity. Additionally, the errors should follow a normal distribution, which is essential for valid statistical inference and hypothesis testing.

When selecting a regression model, model complexity must be carefully considered. A model that is overly complex may overfit the data, capturing noise as signal, while a simpler model may not account for all the nuances in the data, leading to underfitting. Cross-validation serves as a vital tool to assess the model's ability to generalize to unseen data, while metrics such as R-squared, Mean Squared Error (MSE), and Root Mean Squared Error (RMSE) provide insight into the model's predictive accuracy.

Feature selection is another critical step, ensuring that only the most influential predictors are included in the model. Techniques like forward selection or stepwise regression help identify these key variables. If interactions between predictors influence the response variable, including interaction terms can significantly improve the model's performance.

To validate the assumptions of the regression model, model assumption validation becomes necessary. This can be done through residual analysis, using plots such as residual versus fitted plots and Q-Q plots to check for linearity, independence, homoscedasticity, and normality. Furthermore, sensitivity analysis should be performed to evaluate the impact of varying input parameters, identifying which factors are most influential in determining the model's outputs.

Incorporating advanced techniques such as FAST, Least Squares Regression (LSR), Multi-Level Sampling Methods (MLSM), Hyper Kriging, and Radial Basis Functions (RBF) in HyperStudy is crucial for optimizing complex systems. These methods not only streamline the analysis process but also enhance model performance by reducing computational costs and improving the accuracy of predictions. By intelligently selecting the best models and handling non-linear relationships, these techniques enable engineers to achieve more precise and efficient optimizations across diverse engineering applications [83].

3. Experimental Studies in Component Optimization

Pre-processing

The key components of MDAO include an interdisciplinary approach, mathematical modelling, design variables and objectives, optimization algorithms, constraints, sensitivity analysis, trade-off analysis, an iterative process, and the use of simulation and analysis tools. MDAO recognizes that many engineering systems are inherently complex and involve the interaction of multiple disciplines. For example, designing an aircraft involves aerodynamics, materials science, structural analysis, control systems, and more. MDAO brings experts from these disciplines together to collaborate on a holistic design. Mathematical models are developed to describe the behavior of the system across multiple disciplines. These models are typically represented by sets of equations, and they capture how the system's variables are interrelated. This is a crucial step because it allows engineers to quantify the impact of changes in one discipline on other disciplines. Engineers identify design variables that can be adjusted to improve system performance. Simultaneously, they establish objectives that define the system's desired performance metrics, such as minimizing weight, maximizing fuel efficiency, or minimizing cost. These objectives often conflict with each other, making optimization a complex task [86].

MDAO employs optimization algorithms to systematically explore the design space and find the best possible solution. These algorithms use mathematical models to predict how changes to the design variables impact the objectives. Various optimization techniques, such as gradient-based methods, genetic algorithms, and particle swarm optimization, can be applied depending on the complexity of the problem. In real-world engineering, various constraints must be satisfied during the optimization process. These constraints can include factors like safety regulations, budget limitations, and manufacturing constraints. MDAO ensures that the optimized solution adheres to these constraints. Engineers use sensitivity analysis to understand how slight changes in design variables affect the objectives and constraints. This insight helps them make informed decisions during the design process and ensures the reliability of the optimization results [87].

In many cases, optimizing one aspect of a design might come at the cost of another. MDAO enables engineers to explore these trade-offs and make informed decisions about design

compromises. MDAO is often an iterative process. Engineers refine the design by repeatedly running optimization analyses, adjusting design variables, and re-evaluating the results until an optimal solution is achieved. MDAO relies heavily on simulation and analysis tools to solve complex systems. These tools allow engineers to conduct virtual experiments to understand how different design variations will perform [88].

MDAO is an invaluable approach in modern engineering and plays a pivotal role in creating innovative, high-performance products and systems. It not only streamlines the design process but also contributes to cost reduction, improved efficiency, and environmentally friendly solutions. Its applications continue to expand as industries strive for more sophisticated and sustainable designs.

HyperStudy plays a pivotal role in Multi-Disciplinary Analysis and Optimization by significantly enhancing the efficiency and effectiveness of the optimization process across various engineering disciplines. Its seamless integration with simulation and analysis tools enables engineers to systematically explore complex design spaces and identify optimal solutions.

One of HyperStudy's key functions is its ability to facilitate comprehensive design space exploration. By efficiently varying design variables and evaluating their impact on performance metrics, HyperStudy assists in identifying promising design configurations that balance conflicting objectives. This capability is crucial in achieving high-performance and cost-effective designs in industries such as aerospace, automotive, and civil engineering.

Moreover, HyperStudy interfaces with a diverse range of simulation software, automating the iterative process of running simulations for each design iteration. This integration not only saves time but also reduces manual effort, allowing engineers to focus more on analyzing results and refining designs.

HyperStudy leverages advanced optimization algorithms such as genetic algorithms, response surface methods, and stochastic approaches. These algorithms enable engineers to navigate intricate design landscapes, iteratively refining designs based on simulation feedback to converge towards optimal solutions.

Sensitivity analysis capabilities within HyperStudy provide engineers with insights into how variations in design variables impact performance metrics and constraints. This analysis is

essential for understanding design robustness and making informed decisions throughout the optimization process.

In practical applications, HyperStudy accelerates the design cycle by automating tasks, enhancing collaboration among interdisciplinary teams, and facilitating the exploration of innovative design solutions. Its user-friendly interface simplifies setup and management of optimization studies, ensuring robust and reliable MDAO processes that meet the demanding requirements of modern engineering challenges following the designated steps for it to be implemented correctly.

3.1 Benchmark

Benchmarking plays a critical role in assessing and improving the performance and safety of electric vehicles (EVs). It provides a systematic approach to comparing key parameters against industry standards and competitor data. This chapter delves into the benchmarks established for crash analysis and thermal analysis of an electric vehicle, highlighting methodologies, findings, and their implications on design improvements.

Crash analysis benchmarking focuses on evaluating the structural integrity and passenger safety of EVs during various impact scenarios, such as frontal, side, rear collisions, and rollovers. These simulations are conducted using advanced tools like LS-DYNA, ANSYS, and HyperMesh, and adhere to international safety standards, including Euro NCAP, FMVSS, and IIHS. The parameters analyzed include energy absorption, deformation patterns, and occupant safety metrics such as Head Injury Criterion (HIC) and neck forces. A significant aspect of crash analysis for EVs is ensuring the safety of high-voltage battery packs and mitigating risks associated with thermal runaway during impact. Compared to traditional internal combustion engine vehicles, EVs present unique challenges due to the placement and structural integration of the battery pack. The findings from benchmarking reveal areas requiring structural reinforcements, such as crumple zones and protective casing for batteries, to enhance crashworthiness.

Thermal analysis benchmarking addresses the critical need for effective thermal management in EVs, focusing on battery performance, safety, and vehicle efficiency. This analysis evaluates scenarios like battery cooling, heat dissipation, and thermal runaway prevention under various operating conditions, including extreme climates. Computational tools like

ANSYS Fluent and experimental methods, such as thermal imaging, are employed to study temperature distribution, heat flux, and cooling efficiency. One of the primary challenges is ensuring that the battery system maintains optimal temperature ranges while balancing aerodynamic efficiency and weight constraints. The benchmarking process highlights innovative solutions such as advanced cooling mechanisms, the use of thermal insulators, and design adaptations to manage heat more effectively. These findings are compared to industry standards, revealing competitive advantages or areas needing further development. The benchmarking results are compared against established industry norms to assess the EV's performance comprehensively. These comparisons provide valuable insights into gaps and opportunities for design enhancements. For instance, findings from crash analysis led to the introduction of reinforced materials in critical structural components and optimized battery placement to improve energy absorption during collisions. Similarly, insights from thermal analysis informed the design of more efficient cooling systems and better material selection for thermal insulation, thereby enhancing overall vehicle safety and efficiency.

These benchmarks significantly influenced the EV's design iterations, leading to notable improvements in safety and performance. Structural reinforcements and optimized component placement emerged as direct outcomes of crash analysis. Thermal analysis results guided the development of innovative cooling solutions, ensuring that the vehicle meets stringent safety standards while maintaining high efficiency. This iterative process underscores the importance of benchmarking in advancing EV technology.

Future research and development in EV benchmarking can explore emerging technologies like solid-state batteries and advanced cooling materials. These innovations have the potential to address current limitations and further enhance safety and performance metrics. Additionally, integrating machine learning and artificial intelligence in simulation processes can improve the accuracy and efficiency of benchmarking efforts.

3.1.1 Reverse engineering

Reverse engineering to analyze suspension assembly points and determine the center of gravity for a vehicle dynamics perspective involves a structured and meticulous approach. The process begins with the careful disassembly of the vehicle, focusing on exposing the suspension system's mounting points without causing damage to surrounding components.

This step ensures that the original geometry and assembly conditions are preserved for accurate analysis.

Once the suspension is accessible, precise measurements are taken using tools like calipers to capture the exact locations of the suspension assembly points. These measurements are crucial for retaining the suspension's intended functionality and alignment in future designs or modifications. The data is then digitized into CAD models, allowing engineers to document and analyze the suspension system's original configuration.

Simultaneously, the center of gravity of the vehicle is determined to evaluate its influence on vehicle dynamics. This involves conducting static balance tests or employing mass distribution analysis, where the weight and balance of individual components are calculated to locate the overall center of gravity. This information serves as a foundational reference when integrating additional components, such as a battery housing, ensuring that the overall design maintains stability and optimizes vehicle handling.

Although the concept of suspension assembly points and center of gravity is distinct from that of a battery housing, these elements serve as critical starting points for designing a functional system. Understanding the suspension's mounting and the vehicle's mass distribution helps engineers assess how a battery housing can be incorporated without negatively impacting the vehicle's dynamics.

The final step integrates the collected data into dynamic simulations using software tools. These simulations help validate the suspension's design and evaluate its interaction with the vehicle's dynamics. By reverse engineering and analyzing these critical parameters, engineers can ensure that the redesigned or modified vehicle retains optimal performance characteristics while accommodating additional design elements such as a battery housing, all while meeting safety and design standards.
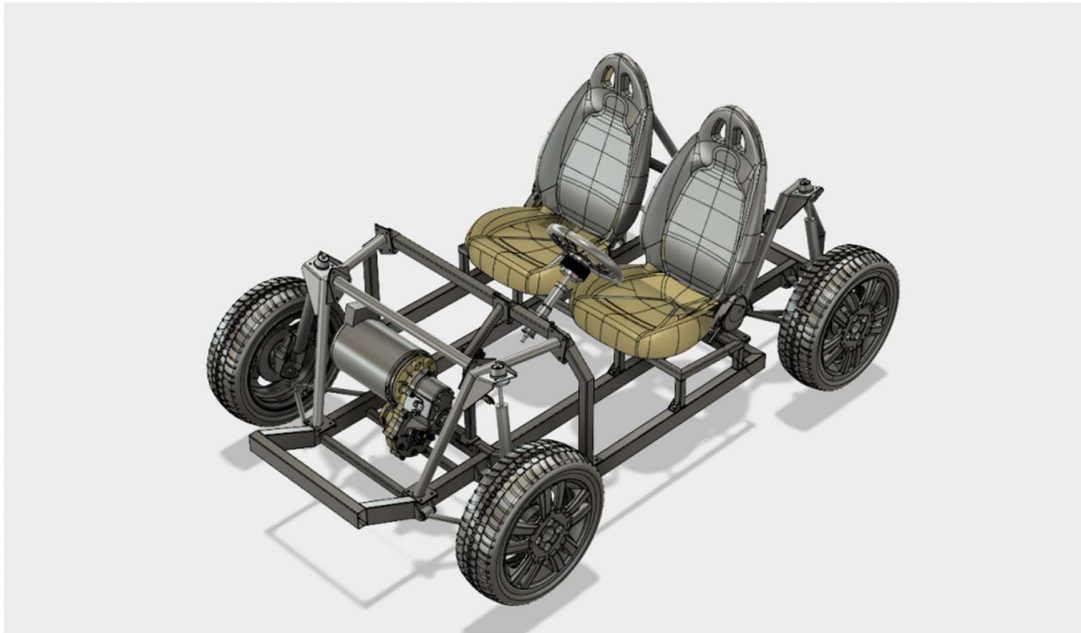
Figure 3.1 - Reverse engineering of tabby EVO

3.1.2 CAD model

After conducting the reverse engineering process, the next crucial step involves creating an accurate CAD model based on the collected data. This phase is critical as it transforms the physical measurements into a detailed digital representation of the suspension system and its components. Using the precise measurements obtained from tools like calipers, the suspension assembly points are accurately reconstructed in a CAD environment. Each component, including mounting brackets, joints, attachment points, and structural elements, is modelled to reflect their original positions and configurations as identified during disassembly.

The CAD model acts as a comprehensive digital blueprint that captures the exact geometric relationships between these components. It includes the positioning of suspension mounting points, the integration of components like control arms, and the attachment of bushings and fasteners. This digital model not only preserves the original design intent but also provides a valuable tool for visualizing and understanding the suspension system's overall architecture. It enables engineers to document the as-built conditions of the vehicle, which is essential for making informed design decisions for potential improvements, modifications, or repairs.

Moreover, the CAD model serves as the basis for advanced simulations. Engineers can perform static and dynamic analyses to evaluate the structural integrity, stress distribution, and load paths within the suspension system. By integrating the physical measurements into the CAD model, it allows for precise simulations of the vehicle's behavior under different operating conditions, such as cornering, braking, and acceleration. These simulations help identify any design weaknesses, validate the performance of the suspension components, and ensure that modifications made for weight reduction, improved handling, or enhanced safety are effective and aligned with the original design criteria.

Although the suspension assembly points and center of gravity analysis are distinct from battery housing, they serve as foundational parameters for designing a functional vehicle system. Understanding the vehicle's suspension geometry and mass distribution is crucial for ensuring that additional elements like battery housing are incorporated without negatively affecting handling or stability. The CAD model becomes an essential tool not only for reverse engineering but also for subsequent design optimization, ensuring that the final product meets performance, safety, and integration standards.

3.1.3 Pre-processing for CAE

Following the creation of the detailed CAD model, the next crucial step involves preprocessing the model in a CAE (Computer-Aided Engineering) software environment. This phase is essential for preparing the model for subsequent simulations and analyses. The CAD model, which accurately captures the suspension assembly points and the center of gravity, is imported into the CAE software, serving as the foundation for the analysis process. During preprocessing, the model undergoes several key steps to set it up for various simulations.

First, the material properties are defined based on the reverse-engineered measurements and the original design specifications. This involves specifying the type of material used for each component, such as aluminum alloys, steel, or composites, along with their respective mechanical properties like modulus of elasticity, yield strength, and density. These material definitions are crucial for accurately simulating the mechanical behavior of the suspension system under different loads and conditions.

Next, boundary conditions and loading scenarios were applied to the model. Boundary conditions define how the passive battery thermal management system is physically constrained, typically through fixed supports or rigid body constraints, reflecting the system's mounting points on the vehicle chassis. Loading scenarios are defined to replicate real-world conditions, such as vertical loads due to vehicle weight, lateral loads from cornering, and dynamic loads during braking and acceleration. These scenarios are based on the reverse-engineered data, ensuring that the CAE model accurately represents the suspension system's operational environment.

The model is then discretized into finite elements, which are the building blocks for the simulations. Meshing is a critical preprocessing step, where the CAD model is divided into smaller elements, such as shell elements for thin-walled structures or solid elements for more complex parts. The mesh quality is carefully controlled to balance accuracy and computational efficiency. A finer mesh is used in areas with high stress concentrations, such as near mounting points or joints, to capture local effects accurately. Conversely, coarser meshes are used in areas where the stress distribution is more uniform, which reduces computational demands.

The preprocessing phase also includes the definition of element types and material models within the CAE software. Different element types, such as tetrahedral, hexahedral, or shell elements, are selected based on the component's geometry and the type of analysis required. For instance, shell elements are used for the suspension components to simulate their thin-walled nature, while solid elements are used for more robust parts like the chassis brackets. Material models, which describe the relationship between stress and strain for each component, are defined based on the reverse-engineered measurements and the physical properties specified earlier. These models ensure that the simulations reflect the true behaviour of the suspension system under load.

Finally, the preprocessing stage includes setting up analysis parameters. This involves defining the type of analysis to be conducted, such as static, dynamic, or modal analysis. For example, static analysis might be used to evaluate the passive battery thermal management system's ability to withstand various loading conditions, while dynamic analysis can simulate the vehicle's response to road inputs or impacts. Modal analysis is used to determine the

natural frequencies and vibration modes of the suspension components, which is critical for identifying potential resonance issues.

Although these preprocessing steps are specific to the passive battery thermal management system, understanding the vehicle's suspension geometry and mass distribution is essential when integrating additional components like a battery housing. Proper mass distribution and load path definition help ensure that modifications, such as a new battery housing, do not compromise vehicle handling, safety, or performance. By translating the reverse engineering findings into the CAE model and completing the preprocessing steps, engineers can effectively simulate and validate the suspension system's behaviour, ensuring that it aligns with both the original design parameters and any additional modifications required for system integration.

Thermal

Preprocessing for a thermal simulation involves preparing a CAE (Computer-Aided Engineering) model to accurately simulate heat transfer and temperature distributions within the components of the passive battery thermal management system. This phase is essential for assessing thermal performance, ensuring components operate efficiently under thermal loads, and preventing issues such as thermal fatigue or overheating.

Model set-up

The first step in the process is importing the CAD model. The detailed CAD model, derived from the reverse engineering process, serves as the foundation for thermal simulation. This model includes all passive battery thermal management system components, their attachment points, and other critical elements that will be subjected to thermal loads. The import process is critical, as it establishes the baseline for all subsequent analysis. The model is brought into the CAE software with careful attention to preserving the accuracy of its geometry and features, ensuring that the physical components are faithfully represented. This step also includes validating the model's alignment, ensuring that complex assemblies are correctly positioned, and verifying that any additional data, such as material properties or boundary conditions, is compatible with the software. Any necessary adjustments are made at this stage to maintain design integrity under thermal loading conditions. These adjustments might

include modifying small fillets, simplifying intricate features that do not influence thermal behavior, or ensuring smooth transitions between component surfaces to reflect realistic thermal conduction.

Once the CAD model is imported, geometry cleanup is performed to prepare the model for thermal analysis. This involves eliminating unnecessary surfaces, gaps, or non-essential features to create a clean, watertight model suitable for meshing. The cleanup process ensures that only relevant features directly influencing thermal behavior are retained. Redundant features that do not contribute to the thermal simulation, such as internal voids unaffected by heat or small decorative elements, are removed. Special attention is given to ensuring the continuity of surfaces and connections between components to avoid mesh errors or inaccuracies during simulation. This step reduces computational costs by streamlining the model, which is particularly important for large or complex assemblies. By simplifying the geometry and resolving potential issues early, the cleanup process not only optimizes simulation performance but also enhances the accuracy and reliability of the results, providing a solid foundation for detailed thermal analysis.

Material Definitions

To simulate the thermal behavior of a passive battery thermal management system accurately, specifying the thermal properties of each component is a critical step. These properties are defined based on reverse-engineered measurements and material specifications, ensuring that the simulation reflects real-world conditions. Key thermal properties include thermal conductivity, specific heat capacity, and density.

Thermal conductivity determines how efficiently a material conducts heat, directly affecting the rate of heat transfer through the suspension components. Specific heat capacity measures the amount of heat a material can store, influencing how components respond to temperature changes over time. Density plays a vital role in calculating heat storage, as it relates to the material's mass and its ability to absorb and retain heat.

For the battery thermal management system, materials such as steels, aluminum alloys, or composites are commonly used. Each material has unique thermal properties that must be accurately defined to capture realistic heat transfer and thermal gradients within the system. By specifying these properties with precision, engineers ensure the thermal simulation

provides reliable insights into the performance and durability of the battery thermal management system components under various scenarios.

Meshing

The discretization of the model into finite elements is a crucial step in preparing for thermal simulations, as it directly impacts the accuracy of temperature and heat flux predictions. The type and quality of elements used significantly influence the reliability of the analysis results. Thin-walled structures, such as certain passive battery thermal management system in the bracing on the structure such as brackets, are typically modelled with shell elements, which are efficient for capturing heat transfer across thin geometries. Thicker components, such as solid mounts or fixtures, require solid elements to accurately represent their three-dimensional thermal behavior, ensuring realistic modelling of heat conduction and storage within these components.

Mesh quality is particularly critical in areas with high-temperature gradients or significant thermal stresses. For example, regions around fasteners, joints, or interfaces between dissimilar materials often experience complex thermal interactions due to differences in thermal expansion and conductivity. A finer mesh in these areas ensures that the simulation captures precise temperature distributions and potential thermal stress concentrations. In contrast, regions where heat transfer is relatively uniform, such as simple solid blocks or homogeneous areas, can be modelled with coarser meshes to optimize computational efficiency.

The implications of these considerations for thermal analysis are significant. Poor element type selection or inadequate mesh refinement can lead to errors in predicting thermal behavior, such as overheating or uneven thermal expansion, which may cause component failure. Accurate meshing ensures that critical phenomena like localized hotspots, temperature gradients near joints, and thermal fatigue risks are captured, allowing engineers to evaluate and mitigate potential issues. For example, refining the mesh around welds or mounting points ensures the accurate calculation of thermal stress concentrations that could lead to material fatigue or failure over time. These insights are crucial for validating the design and ensuring the durability and safety of the suspension components under real-world operating conditions.

Boundary Conditions and Loading

Defining thermal loads is a critical step in simulating the thermal behavior of the passive battery thermal management system components, as it establishes the boundary conditions and heat sources that mimic real-world operating environments. Boundary conditions are applied to the model to simulate external and internal thermal influences. These include environmental temperature boundaries, thermal contacts with adjacent components, and convective heat transfer between the components and surrounding air. By incorporating these factors, the simulation accounts for realistic thermal interactions experienced during operation.

Thermal loading scenarios are tailored to represent specific operational conditions. For instance, the heat generated from friction during braking systems or engine heat dissipation can significantly impact nearby suspension components. Similarly, ambient temperature variations, such as exposure to extreme cold or heat, must also be considered. These scenarios simulate the heat flux through the suspension system, enabling engineers to predict temperature distribution, thermal expansion, and stress levels accurately.

Heat sources and heat flux play a pivotal role in capturing localized thermal effects. Specific heat sources. The locations, intensities, and durations of these heat sources are determined based on reverse-engineered data and real-world operating conditions. Accurate definition of these sources is essential for understanding how heat propagates through the suspension system and affects its performance.

For example, improperly defining a heat source's intensity or location could lead to incorrect predictions of thermal gradients, which might result in overlooked areas of thermal stress or expansion. Conversely, well-defined heat sources enable engineers to identify potential problem areas, such as hotspots that could weaken materials or cause thermal fatigue. These insights are critical for optimizing the suspension system's design to withstand thermal loads, maintain performance, and ensure durability under diverse operating conditions.

Crash

Preprocessing for a crash simulation involves a series of critical steps to set up the model accurately for dynamic analysis. This phase is crucial to ensure the CAE model accurately represents the physical behavior of the battery housing system and surrounding structures

during a crash scenario. The goal is to simulate the vehicle's response to impact, including the deformation and energy absorption characteristics of components.

Model Preparation

The detailed CAD model from the reverse engineering process is imported into the CAE software. This model serves as the starting point for the crash simulation. It should accurately represent the suspension components, their attachment points, and the overall vehicle structure. The model is checked for completeness and accuracy, ensuring that all important features, such as mounting brackets and joints, are included.

Material Definitions

The material properties of each component within the battery housing system are defined based on reverse-engineered data and physical testing results. For a crash simulation, materials are often modelled with nonlinear stress-strain curves to account for large deformations and plasticity. This might include properties like yield strength, ultimate tensile strength, and strain hardening behavior. Materials such as high-strength steels, aluminum alloys, or composites are typically used in suspension components due to their strength-to-weight ratios and energy absorption capabilities.

Meshing

The model is discretized into finite elements suitable for crash simulations. Shell elements are commonly used for thin-walled structures like the suspension arms and brackets, while solid elements are used for thicker components such as chassis members. The mesh quality is crucial; elements should be fine enough to capture localized deformations and stress concentrations accurately. This involves creating a high-density mesh in areas where significant plastic deformation is expected, such as near mounting points and joints. The elements must also be sufficiently refined around critical interfaces like welds or bolt connections to capture their influence accurately.

Contact Definitions

In a crash simulation, it's vital to define interactions between various parts of the model. This includes setting up contact surfaces to simulate the engagement between the vehicle body, battery housing components, and any other parts that may come into contact during the impact. Contact types include frictional (where two surfaces slide against each other) and hard (where surfaces penetrate but do not separate) contacts. These contacts simulate the physical interactions that occur during a crash, such as the battery housing system contacting the vehicle frame or other components.

Boundary Conditions and Loading

Boundary conditions are applied to simulate the crash scenario. This involves setting up the initial position and velocity of the vehicle. For instance, the vehicle may be simulated as hitting a fixed barrier or another moving vehicle at a specific impact speed and angle. The loading conditions are defined to represent realistic crash scenarios. This could include the impact speed, direction, and the load applied to the battery housing system. The objective is to replicate the dynamic forces experienced during a collision accurately.

3.2 FEA

The preprocessing stage of this thesis serves as the foundational step in the integration of multidisciplinary analyses into the design process of an electric vehicle's suspension system. This stage involves the careful preparation and setup of CAE (Computer-Aided Engineering) models to accurately represent the mechanical and thermal behaviors of components under various operational conditions. The primary objective during preprocessing is to ensure the fidelity and accuracy of the simulation results, which are crucial for subsequent Multidisciplinary Design Analysis and Optimization (MDAO) processes. This thesis explores the integration of base analyses for crash simulation and thermal simulation into the MDAO framework. The crash simulation setup aims to evaluate the dynamic responses of the battery housing system during collision events, focusing on energy absorption and component integrity. Concurrently, thermal simulation prepares the model for assessing heat transfer and temperature distributions within the suspension components, considering realistic thermal loading scenarios. By addressing these two critical aspects during preprocessing, this thesis lays the groundwork for a comprehensive MDAO, enabling the optimization of the suspension system's performance and safety characteristics.

3.2.1 1st Case - Crash Analysis

The NOM-194-SE-2021 is the official regulation in with states that the standard for a vehicle to be able to transit in Mexico is to pass the regulation UN R94 for a frontal impact and UN R95 for a lateral impact and UN R135 for a side pole impact, in which the norm UN R135 is the toughest to pass for a battery housing due to the area of the impact.

The homologation procedure mandates the testing of a prototype vehicle representative of the desired approval category. Employing an adult male WorldSID dummy, renowned within the industry for its fidelity to human anatomical characteristics, these tests subject the dummy to various collision scenarios, furnishing invaluable insights into the vehicle's occupant protection capabilities.

Central to these evaluations is the vehicle's performance in pole impact tests, typically conducted on the driver's side, barring exceptional circumstances. This direct assessment method facilitates an appraisal of the vehicle's protective structures in a commonplace collision scenario.

The acceptability of test outcomes hinges upon their alignment with meticulously outlined criteria. These criteria, categorized according to specific aspects of dummy behavior, encompass critical parameters including head injury criteria, shoulder force, thoracic and abdominal deformations, as well as pelvic behavior. Each criterion delineates thresholds that the dummy must not surpass for the vehicle to be deemed safe.

For instance, with regards to head injuries, the Head Injury Criterion (HIC) stipulates that the head injury criterion must not exceed 1,000, thereby ensuring that the risk of severe head trauma remains within acceptable limits even under extreme collision conditions. Analogously, prescribed limits for maximum shoulder force or thoracic rib deformation establish stringent benchmarks to safeguard occupant well-being during collisions.

In addition to assessing dummy behavior, exacting standards are imposed on the integrity of vehicle systems such as closure mechanisms, hinges, and fuel systems. Notably, vehicle doors must withstand impacts and retain the integrity of their closure and hinge systems post-collision. Similarly, stringent thresholds govern fuel leakage, ensuring minimal post-impact leaks to mitigate any additional risks to vehicle occupants.

For simplification of the analysis and the resources this thesis will not have a crash dummy of any sorts, however the implementations of sensors, indicators, and more tools available in HyperMesh will give us an estimate of the deceleration from selected points. The intention of these measurements is not for the model to predict an injury in a passenger but to have an overall picture of the deceleration of the battery housing only.

The base analysis for the first case is the simulation of a side pole crash test, according to NCAP the vehicle will have a velocity of 32 km/h and tilted 15°. The impact will be made to a circular metal tube of 254 mm in diameter as can be appreciated on Figure 3.1 the upper view of the first case.
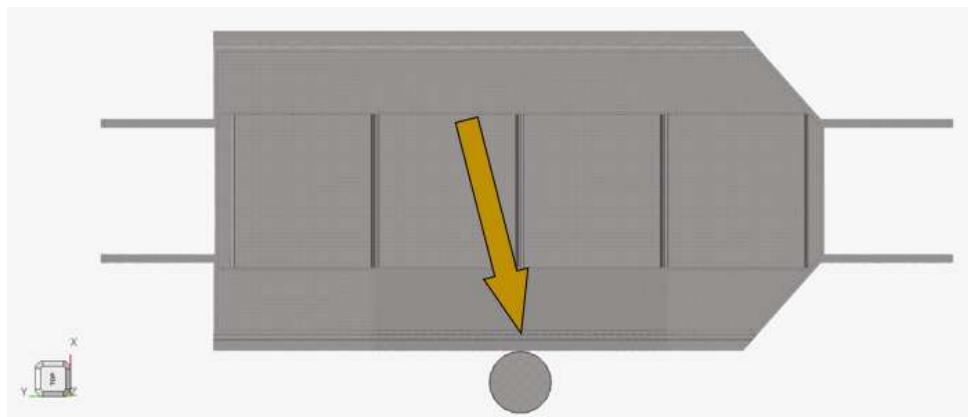
Figure 3.2 - Upper view of base model representing initial velocity.

Set-Up

The setup of the first case in which the MDAO will be analyzed upon has the same bases as the development of any study, geometric restrictions, properties on the elements used, meshing and the materials that are seen and used in the model.

❖ Loads and constraints.

In Figure 3.2 it can be seen the model where the rigid pole is located and is restricted in all 6 degrees of freedom, this implies that the nodes and elements will not move or have any deformation. The area surrounded by the doted lines are the elements which have the added mass of the rest of the electric vehicle and have an initial velocity of 32 km/h in the direction indicated on the right Figure 3.3.
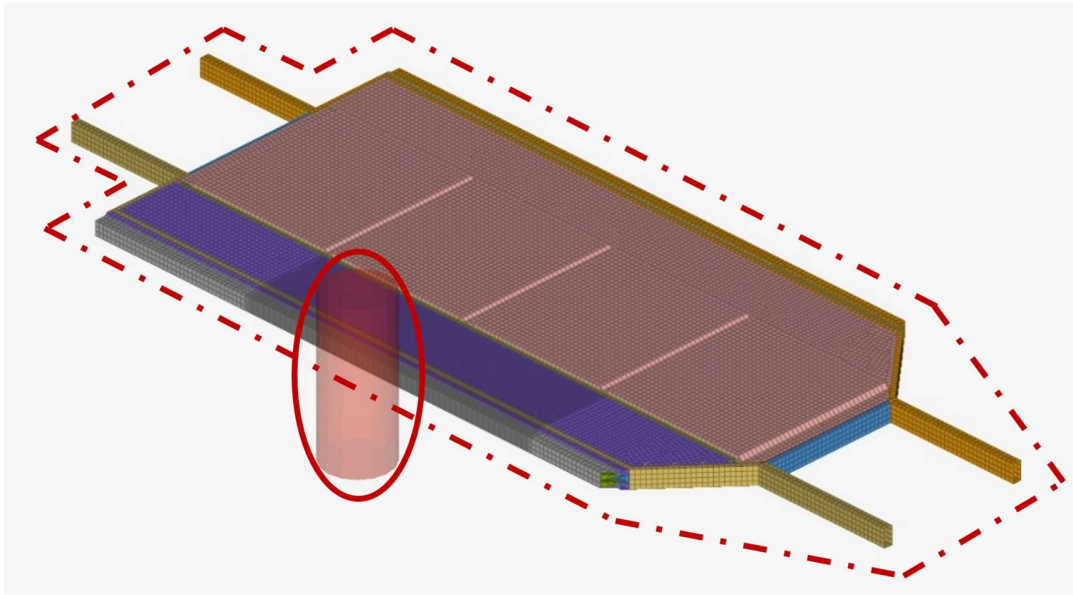
Figure 3.3 - Initial conditions and velocity in the model
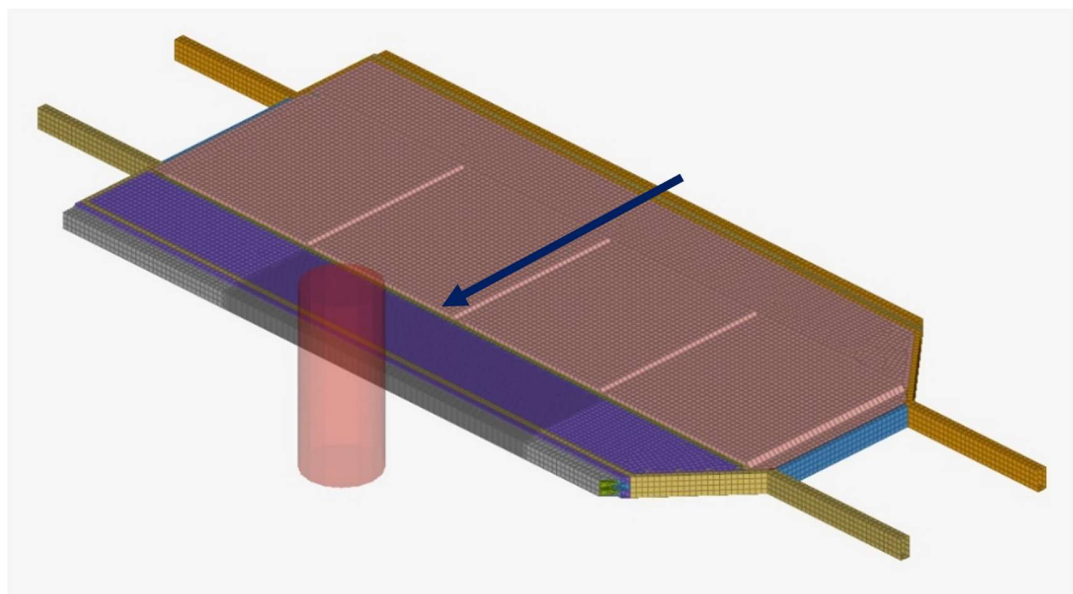
Figure 3.4 - Direction of the initial velocity of 32 km/h

❖ Properties and materials

The materials used in the study are steel and aluminum and the parameters can be looked at in table 3.1 and the application to each element in Figure 3.4. The properties for each shell

element were introduced in table 3.2 where it can be appreciated the different thicknesses and the individual application depending on the color and if there will be considered as a variable on Figure 3.5.

Table 3-1 - Characteristics used in the simulation [74]

	Rho (gr/cm3)	E (Mpa)	υ	Sy (MPa)	Su (MPa)
Steel	7.85	21000	0.33	900	1180
Aluminium	2.75	68000	0.33	276	310

Table 3.2 outlines the mesh properties used in the base analysis, specifying the thickness and assigned colors for different components. All components have a uniform thickness of 3 mm, while colors range from light pink to dark red for BHSP elements and grey for EXT-SH, aiding in visualization and differentiation during analysis.

Table 3-2 - Properties of mesh used in the base analysis.

	Thickness	Color
BHSP-1 (mm)	3	Light pink
BHSP-2 (mm)	3	Pink
BHSP-3 (mm)	3	Red
BHSP-4 (mm)	3	Darck red
EXT-SH (mm)	3	Grey
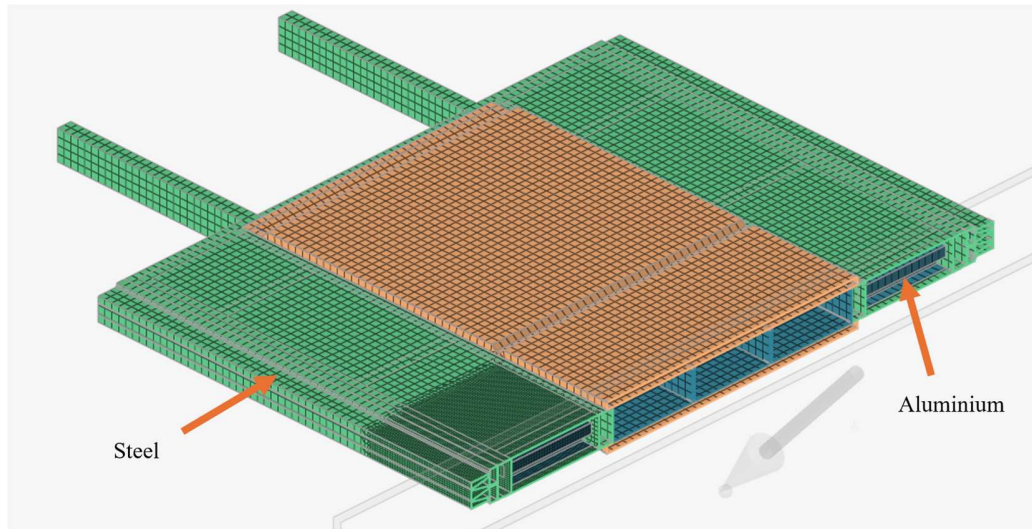
Figure 3.5 - Cross section of isometric view of battery housing showing the different materials.
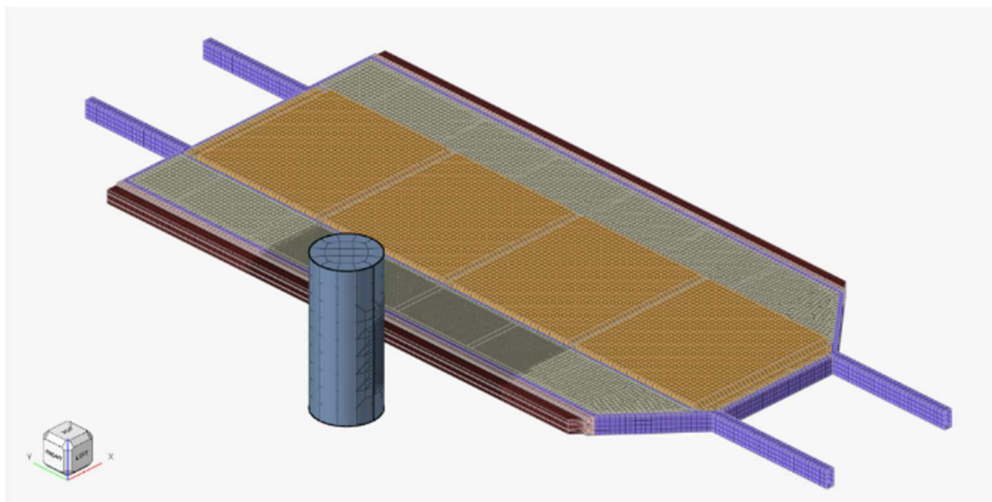
Figure 3.6 - Cross section of isometric view of battery housing showing the different materials.

3.2.2 2nd Case – Thermal analysis

The thermal analysis developed for the proposed battery housing considered the specific properties of the Winston batteries already integrated into the electric vehicle. Given the challenging weather conditions of the northern part of Mexico, where temperatures can exceed 45 degrees Celsius, the thermal analysis needed to address extreme heat scenarios.

To achieve this, the parameters used were based on the detailed thermal characteristics provided by the manufacturers' datasheets, which outline the thermal conductivity, specific heat capacity, and other material properties of the batteries. Additionally, the analysis considered the heat generated during battery discharge at its maximum value, which is a critical factor in maintaining efficient thermal management.

Furthermore, the setup incorporated the effects of wind beneath the vehicle to aid in cooling the bottom part of the battery housing. This aspect of the thermal analysis is particularly important for preventing overheating and ensuring that the batteries operate within safe thermal limits. The model also accounted for solar radiation, which can significantly influence the temperature of the vehicle's exterior surfaces and the suspension components. This included simulating the impact of direct sunlight on the vehicle's body and the consequent thermal strain on the suspension system. The environmental temperature fluctuations and their effects on the thermal expansion and contraction of materials were also considered.

By incorporating these loads and constraints into the thermal analysis, the model closely replicates real-world operating conditions, enabling accurate prediction of thermal behavior. This detailed approach allows for the optimization of the vehicle's thermal management system, ensuring efficient cooling of components, preventing thermal runaway, and improving overall safety and performance under various environmental conditions. The inclusion of these parameters from scientific simulations and datasheet data provides a robust framework for understanding and managing the thermal challenges faced by the suspension system in real-world scenarios.

Set-up

The setup of the second case in which the MDAO will be analyzed upon has the same bases as the development of any study, geometric restrictions, properties on the elements used, meshing and the materials that are seen and used in the model.

❖ Loads and constraints.

The total cases in which the design will be tested and analyzed are based on the ordinary used on an electric vehicle with 3 sets of temperatures. The base case will be set in an environment

of 25 °C, a low temperature case will be set at 0 °C and a high temperature case with 45 °C, Figure 3.6.

The operation of the batteries was also considered on the analysis corresponding the maximum heat flux of a prismatic battery of 956 W/m^2 in each face, Figure 3.7. A case in which the vehicle is moving with a convection value of the air cooling the bottom plate and a standing vehicle with no air cooling the bottom plate, figure 3.8 but the heat flux from the battery decrease significantly due to the lack of energy required from the batteries, Figure 3.9.
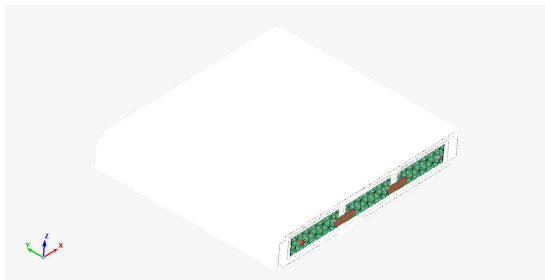
Figure 3.7 - Initial temperature in the thermal simulation.
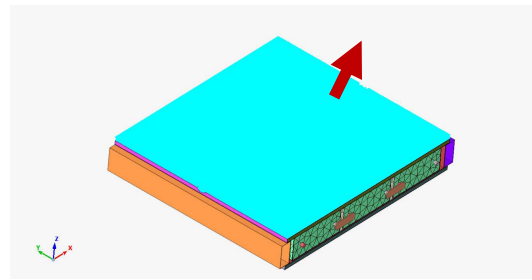
Figure 3.8 - Convection on the bottom cover of the battery housing.
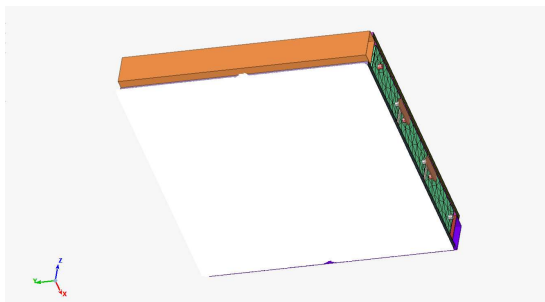
Figure 3.9 - Convection on the top cover of the battery housing.
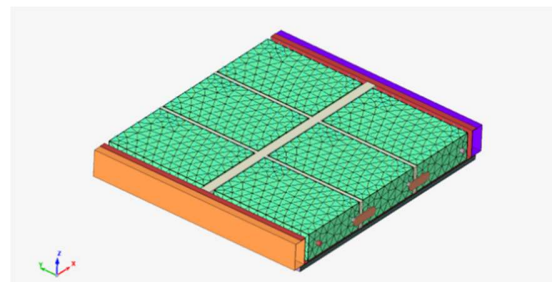
Figure 3.10 - Heat flux of batteries at a pick discharge in movement.

❖ Properties and materials

The materials used in the study are steel and aluminum and the parameters are shown in the table 3.3 and in the special case of the phase change material the tables 3.4 represent the values of the specific heat in the solid and liquid state with the necessary heat required for its transition from solid to liquid.

Table 3-3 - Characteristics used in the simulation.

Material	Thermal conductivity (W/mK)	Specific heat (J/kgK)	Density (kg/m^3)
Steel	49.81	500	7850
Aluminium	175	986	2770

Table 3-4 - Properties of Glauber's salt

Density (kg/m^3)	1485
Melting point (°C)	32
Specific heat as a solid (J/kgK)	1760
Specific heat as a fluid (J/kgK)	3320
Heat of fusion (kJ/kg)	254
Thermal conductivity (W/mk)	0.6

3.3 DOE

Design of Experiments (DOE) with HyperStudy optimizes engineering designs by simulating scenarios, varying parameters, and identifying key factors. This method is vital in automotive engineering, ensuring reliability and performance. By streamlining processes and enabling data-driven decisions, DOE with HyperStudy reduces development time and enhances product quality efficiently.

3.3.1 Set-up

The variables required for the design of an experiment to give us the correct and most efficient results are on table 3.5, where each design has its own variables just for the thicknesses, on the area of materials it will always remain the same.

Table 3.5 lists exported variables for three configurations (BH-1, BH-2, BH-3), defining structural parameters across bottom, base, and top sections. Components like PTR, BHSP, and PILAR are assigned variable values, influencing geometric and material properties. Negative values in shape indicate positional adjustments. These variables are essential for simulation and optimization.

Table 3-5 - Variables exported

BH-1					BH-2					BH-3				
Variable	Variable	Bottom	Base	Top	Variable	Variable	Bottom	Base	Top	Variable	Variable	Bottom	Base	Top
PTR	var_1	1	3	5	BHSP-1	var_1	1	3	5	PTR	var_2	1	3	5
BHSP-1	var_2	1	3	5	BHSP-2	var_2	1	3	5	BHSP-1	var_3	1	3	5
BHSP-2	var_3	1	3	5	BHSP-3	var_3	1	3	5	BHSP-2	var_4	1	3	5
BHSP-3	var_4	1	3	5	BHSP-4	var_4	1	3	5	BHSP-4	var_5	1	3	5
BHSP-4	var_5	1	3	5	PILAR	var_5	1	2	5	BHSP-3	var_6	1	3	5
PILAR	var_6	1	2	5	EXT-SH	var_6	1	3	5	PILAR	var_7	1	3	5
EXT-SH	var_7	1	2	5	CENT-SH	var_7	1	3	5	EXT-SH	var_9	1	3	5
shape1.S	var_8	-1	0	1	CRASH	var_8	1	3	5	shape1.S	var_12	-1	0	1
shape2.S	var_9	-1	0	1	shape1.S	var_9	-1	0	1	shape2.S	var_13	-1	0	1
shape4.S	var_10	-1	0	1	shape2.S	var_10	-1	0	1	shape3.S	var_14	-1	0	1
shape3.S	var_11	-1	0	1	shape3.S	var_11	-1	0	1	shape4.S	var_15	-1	0	1
					shape4.S	var_12	-1	0	1	shape5.S	var_16	-1	0	1
					shape5.S	var_13	-1	0	1	shape6.S	var_17	-1	0	1
					shape6.S	var_14	-1	0	1	shape7.S	var_18	-1	0	1
										shape8.S	var_19	-1	0	1

The output responses were placed after the test in table 3.6 with the name and corresponding initial value. Table 3.6 presents the output responses recorded after the test, listing each parameter alongside its corresponding initial value. These outputs include energy metrics (internal, kinetic, and total energy), mass, momentum, and acceleration values, providing key insights into the system's dynamic behavior during the analysis. The names of the variables were designated by the software, ensuring consistency in data tracking and interpretation.

Table 3-6 - Output values in test model

Internal Energy - MAX	m_1_r_1
Mass	m_1_r_3
X-Momentum - MAG	m_1_r_4
ACCEL CENTRAL MAX	m_1_r_5
ACCEL CENTRAL INTEGRAL	m_1_r_6
ACCEL CENTRAL RESULTANT	m_1_r_7
Kinetic Energy - MINN	m_1_r_8
ACCEL CENT MIN	m_1_r_2
TE-Total Energy - MAG	m_1_r_10
58623 - AX-X Acceleration	m_1_r_9
58623 - ACC-Resultant Acceleration	m_1_r_11

3.3.2 Selected DOE for analysis

The design of experiments used in the MDAO were the modified extensible lattice sequence, in every case analyzed the experiments of thermal and crash analysis it had the best response along the available on HyperStudy.

MELS assumes a critical role as a foundational element in experimental design. In the context of Design of Experiments (DOE), experimental factors are the variables intentionally adjusted to observe their impact on the response variable(s). These factors typically encompass varying levels, each representing distinct settings or values under scrutiny. Establishing MELS involves defining the lowest feasible levels at which each factor can be adjusted during the experiment. This pivotal process ensures that experimental design encompasses a meaningful range of variability, balancing practical and scientific relevance.

By determining MELS, researchers aim to achieve a harmonious blend of experimental comprehensiveness and the pragmatic constraints of resources and time. Thus, MELS serve as guiding parameters that facilitate the formulation of experiments capable of effectively revealing the relationships between factors and response variables, while optimizing resource utilization and minimizing experimental complexity.

3.4 MDAO

In this thesis the MDAO has been focused on two different cases, a crash test within the parameters of the Mexican regulations and a thermal analysis with the ambient temperatures in the northern part of Mexico, specifically in Monterrey Nuevo León México, and charging phases that a battery manufacturer recommends. For each case, a design is proposed reflecting the decrease in the temperature and increase of kinetic energy absorbed by the external frame.

For each specific case, thermal analysis and crash test, needs to have a base analysis that will have; 1) the required variables in which the MDAO software, HyperStudy, will determine the design of experiment (DOE) that needs to be runed, 2) the limits in which the variables will change for each iteration of the base model, 3) The measurement of the final values, maximum or minimum depending on the case, where the decrease of kinetic energy, intrusion on the overall battery housing or the maximum temperature reached will result in a measurable output.

In this thesis the option FAST was selected, according to tests made with the same values the option 3 has the least error and more reliability as it has a value of variance as it shown in the next table with every option available, this because of the integration of the selection of the best performing regression tool available on the software as we can see in the table 3.7.

Table 3-7 - Results according to value of R using regression methods.

R	Node Location	Accelerometer	Mass	Distance between nodes
FAST	0.565	0.907	1.000	0.826
LSR	0.432	0.748	1.000	0.649
MLSM	0.250	0.858	1.000	0.821
HK	-7.561	-0.241	1.000	-1.299

| RBF | -0.197 | 0.895 | .989 | 0.763 |

The reason is that, as HyperStudy dictates, R represents the percentage of explained variance. The value of R normally varies from 0 to 1 where between 1 and .9 indicates an excellent predictive quality, between .9 and .8 indicates good predictive quality with limited error, a value between .8 and .65 has moderate predictive qualities and their use needs the judgment of the user and less than .65 indicates poor predictive qualities. In this thesis the required values and the fitting algorithm will only be implemented when the value of R is above .85 and the values under it will not be considered.

With the mathematical model presented and with a reasonable value of X the optimization of the values for each variable can be conducted, for references it can be a feasible optimization if the value of iterations is close to two hundred. A significant reduction of computational energy is observed, the estimated time for the computer used in this thesis to six models runed at the same time was between 24 and 26 hours, with this methodology we can have an estimate result and behavior of the model within 10 to 15 minutes.

3.4.1 Variables in Crash

The variables in which the crash analysis will be set can be specified in 3 main parts that can be appreciated on Figure 3.11 with a section plane on the dotted line. 1) The external crash structure with the goal to absorb the kinetic energy in the model transforming it to deformation with a purple color, 2) the internal structure that consist in the pillars that will restrict the intrusion on the model with a red color and 3) the upper and lower covers that will continue to reduce the kinetic energy when the external crash structure can no longer absorb more with a green color in the Figure 3.10.
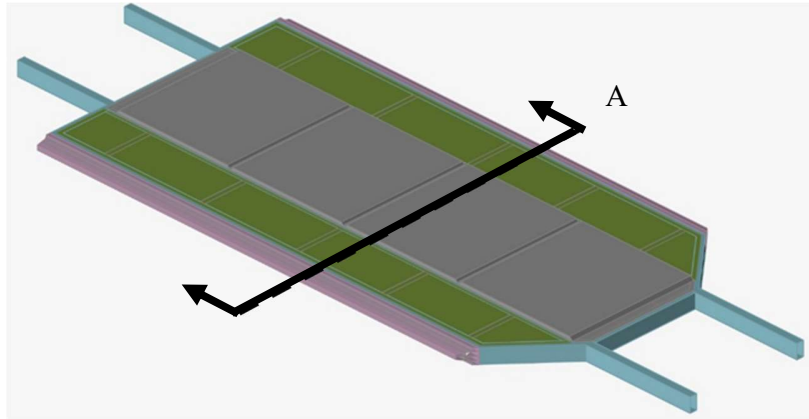
Figure 3.11 - Isometric view with cross section A
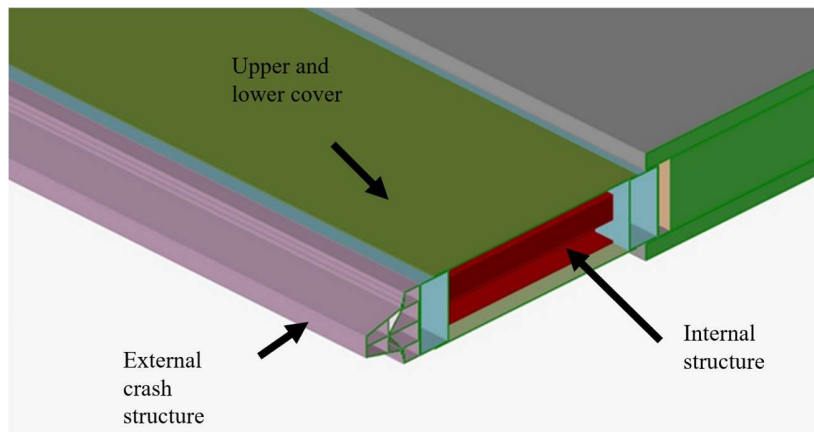
Figure 3.12 - Cross section of the isometric view of the model

❖ External crash structure

For the external crash structure there are three geometries of profiles, Figure 3.12. The profiles are named BHSP-1, BHSP-2, and BHSP-3 and for every single one of the sheet metals used the thickness is also taken as a variable.
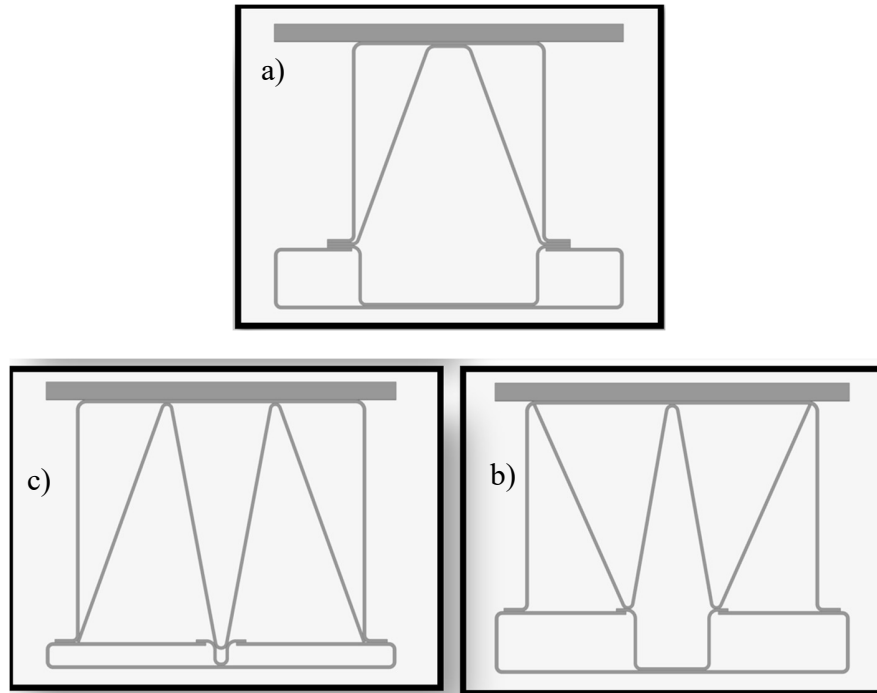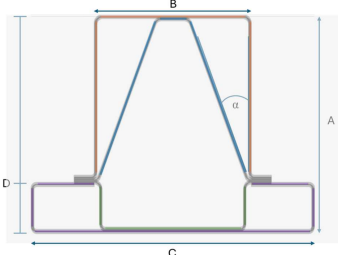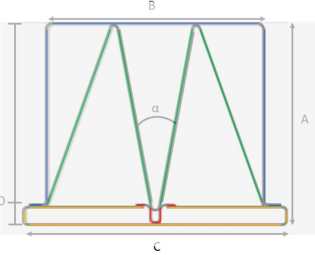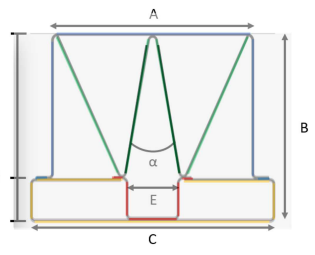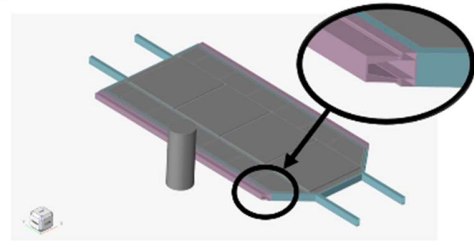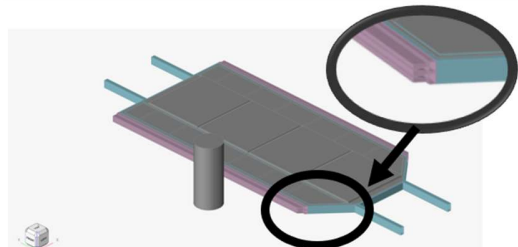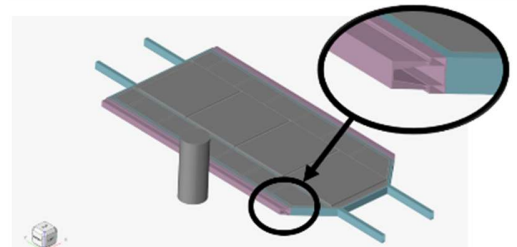
Figure 3.13 - Proposed designs for the external crash structure, a) BHSP-1 b) BHSP-2 c) BHSP-3

This change in the design pretends to decrease the kinetic energy of the vehicle after impact. From design #1 to design #3 is observed that volume increases alongside the change of the geometry and the resemblance to a cardboard internal structure in table 3.8.

Table 3.8 outlines the variables used in the proposed designs, detailing the sheet metal components and their assigned colors for identification. Each BHSP component has multiple design variations, labeled accordingly (e.g., BHSP-1-D1, BHSP-1-D2). Additionally, key geometric variables such as height, width, profile, internal width, and angle are defined with corresponding letter designations, ensuring clarity in parameter tracking and comparison across different design iterations.

Table 3-8 - Variables on proposed designs

BHSP-1		BHSP-2		BHSP-3	
Sheet metal name	Color	Sheet metal name	Color	Sheet metal name	Color
BHSP-1-D1	Orange	BHSP-1-D2	Blue	BHSP-1-D4	Blue
BHSP-2-D1	Blue	BHSP-2-D2	Green	BHSP-2-D4	Green
BHSP-3-D1	Green	BHSP-3-D2	Red	BHSP-3-D4	Red
BHSP-4-D1	Purple	BHSP-4-D2	Yellow	BHSP-4-D4	Yellow
Variable name	Letter	Variable name	Letter	Variable name	Letter
High	A	High	A	High	B
Width	B	Width	B	Width	A
Profile	D	Profile	D	Profile	D
Internal W	C	Internal W	C	Internal W	C
Angle	α	Angle	α	Angle	α

93

❖ Internal crash structure

The intention of the internal crash structure is to reduce the intrusion at the time when the external part of the battery housing absorbs the energy of the impact reaches the point that it can no longer be above more.

The first design will consist of six internal pillars in a longitudinal way for it to prevent intrusion, on the figure 3.13 it is enhanced with the color red of a better illustration. This design is proposed because the form has a different arrangement of material in the interior, in the figure 3.14 is a close-up in the geometry and each variable on the table 3.9.
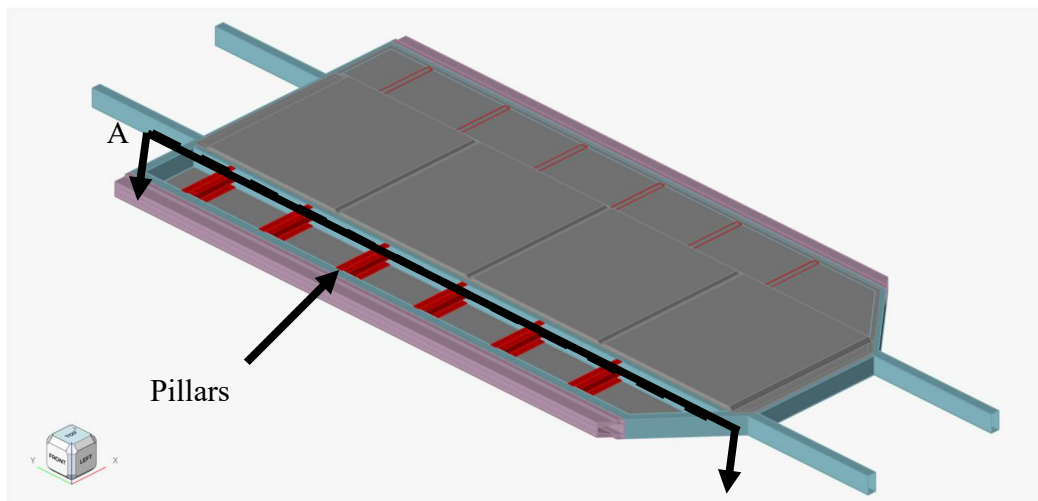
Figure 3.14 - Isometric view of the proposed design with a cross-section A
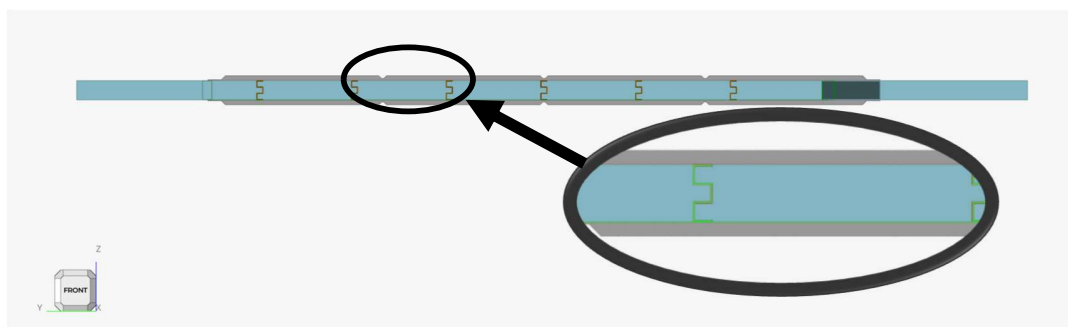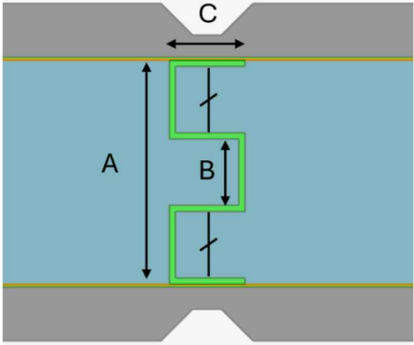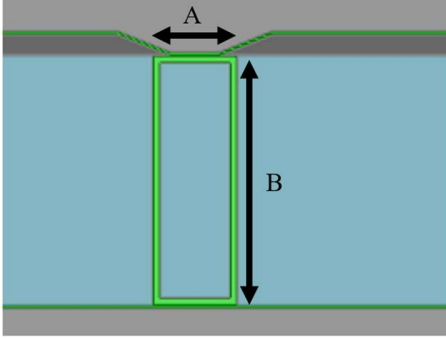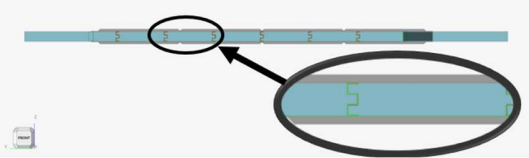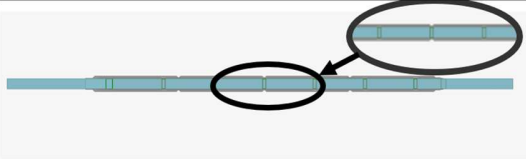
Figure 3.15 - Cross-section A with close-up for internal structure geometry

Table 3-9 - Proposed designs with variables on pillars

ICS-1		ICS-2	
Variable name	Letter	Variable name	Letter
Thickness	S	Thickness	S
High	A	High	B
Width	B	Width	A
Profile	C		

❖ Upper and Lower cover thickness

The intention of the upper and lower cover is to have a continuation in the absorption of energy throughout the entire crash time. This cover also contributes to the stability of the entire structure of the battery housing.

The first and second design analysis was just sheet metal without any modifications; the placement is shown in figure 3.16 and 3.17 with a green color. The thickness will vary from 1 mm to 5 mm on the side of the impact on the opposite side. One comment to be made is that all the sheet metals will increase or decrease their thickness at the same time and will not vary independently.

➢ ULC-1
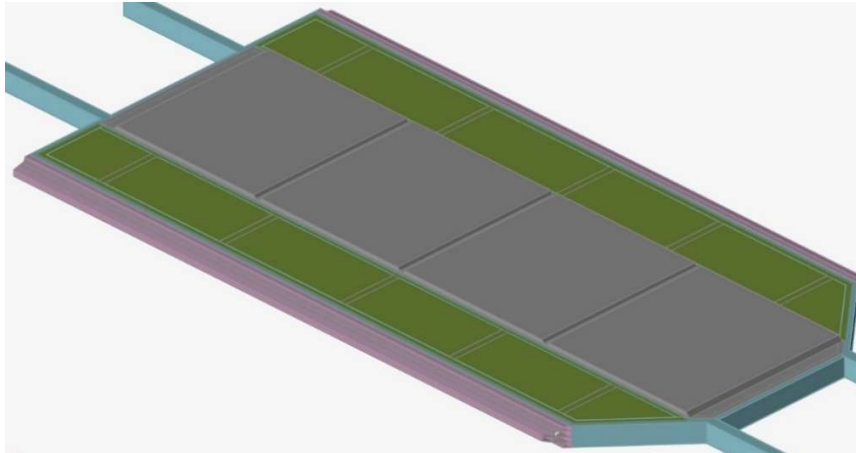
Figure 3.16 - First design of the upper and lower cover

➤ ULC-2
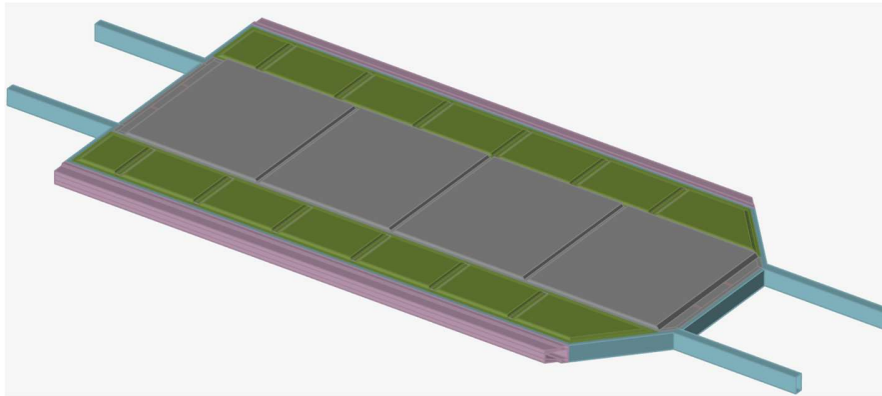
Figure 3.17 - Second design of the upper and lower cover

The only geometric variable on the second design in the lower and upper cover of the battery housing is to alter distance A in figure 3.18.
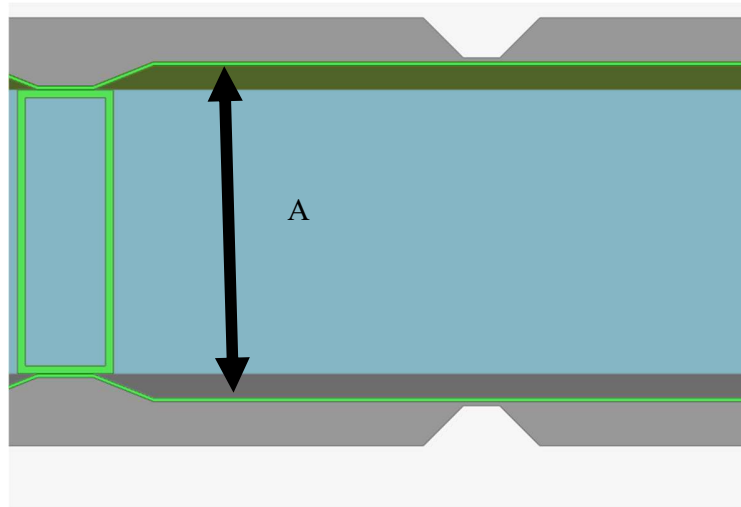
Figure 3.18 - Cross section and close-up of the internal geometry of the second design of the upper and lower cover

3.4.2 Outputs in Crash

The purpose of the specifications of the outputs in the base model is for the postprocessing of the analysis to be run automatically, in the case of the kinetic energy or the internal energy it is specified to take the maximum value, or the minimum value recorded along the time of the simulation.

The base model has three different nodes assigned, and each node has an accelerometer where it will record the acceleration in different places of the battery housing. Two of the accelerometers are placed on the sides to represent the decrease in velocity in the points farthest away from the crash point in the same initial plane, figure 3.19.
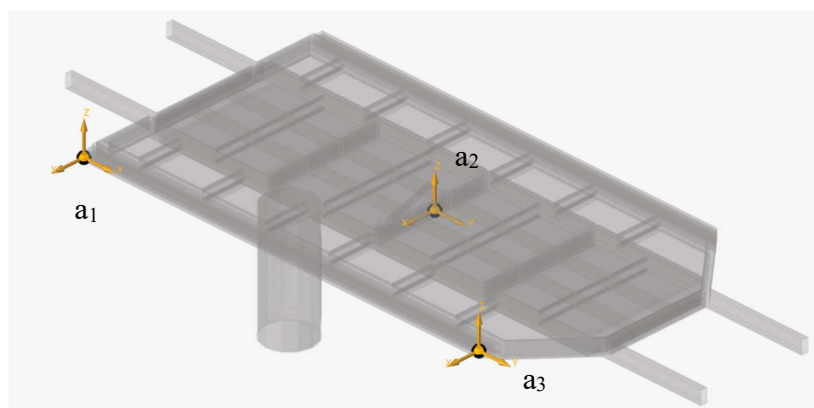
Figure 3.19 - Accelerometers placed on the model.

It has also been assigned the locations of four specific nodes, one in the middle, one in the exact point of contact and the two remaining at some distance from it. This is to be able to analyze the instruction with a reference point. The nodes can be found below in figure 3.20.
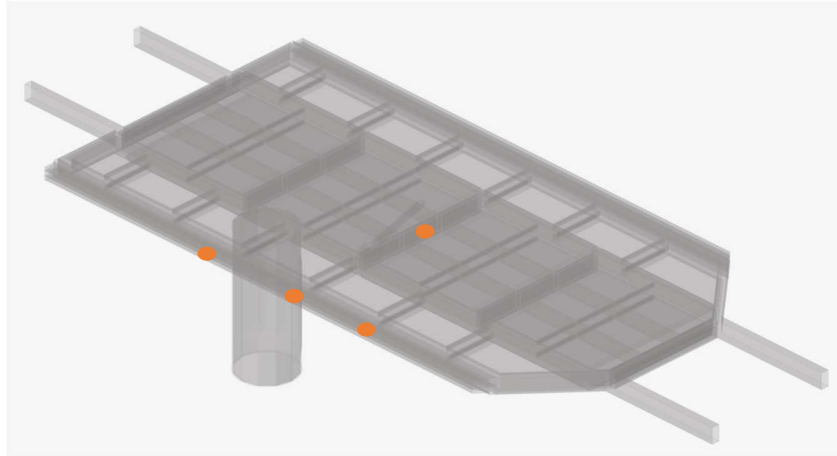
Figure 3.20 - Nodes to be traced in their location, acceleration, and placement.

The model has a recorded general data, these values represent the quantity of: internal energy, kinetic energy, hourglass energy, and the energy of the impact. The model gives these outputs as a reference point in which HyperStudy via a python script will read the generated data as requested and result in a single value on a desired point. It is also obtaining general data such as mass, inertia, global energy and more that are static on the overall run.

In the output file of every iteration, as a base result, exports the general and most common outputs in certain cases. In this analysis the outputs that will be focused on are the internal energy of the model, the kinetic energy, energy in the contact, the mass of the model and the momentum in every axis along with the displacements on the nodes.

3.4.3 Variables in Thermal analysis

The variables in which the crash analysis will be set can be specified in 2 main parts, the geometry on the top and bottom cover, the thickness in which the phase change material is enclosed.

❖ Geometry

The first geometric variable considered in this part of the MDAO consists of the distance D on the figure 3.20. This geometry will vary from figure 3.21 to figure 3.22, changing the area in which the air could have a cooling effect on the bottom and on the top of the battery housing.
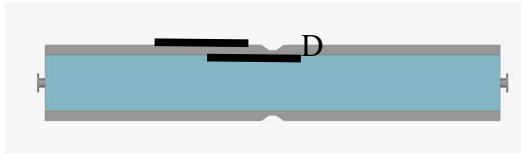
Figure 3.21 - Variable of distance D
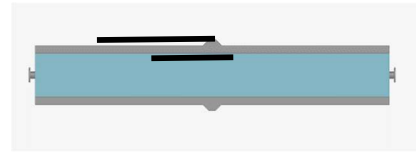
Figure 3.22 - Change in variable D

The second geometric variable is the total thickness of the top and bottom plates that will hold the phase change material as we can see in figure 3.23, allowing more phase change material in the design if it increases of less if it decreases.
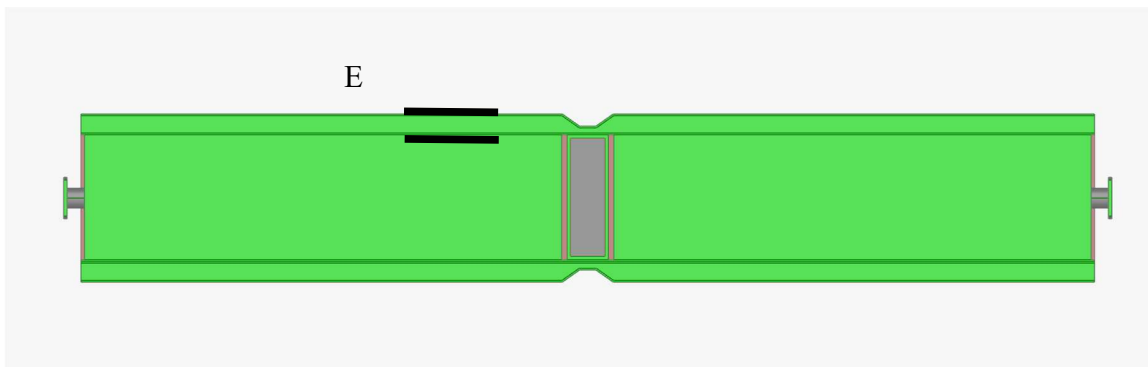
Figure 3.23 - Cross section of battery housing enhancing the distance in between the holding volume of the phase change material

❖ Thicknesses

The variable of the thickness in the model of the thermal analysis will only vary in the case of the enclosure of the phase change material, with the intention on the transmission of heat through the metal, figure 3.24.
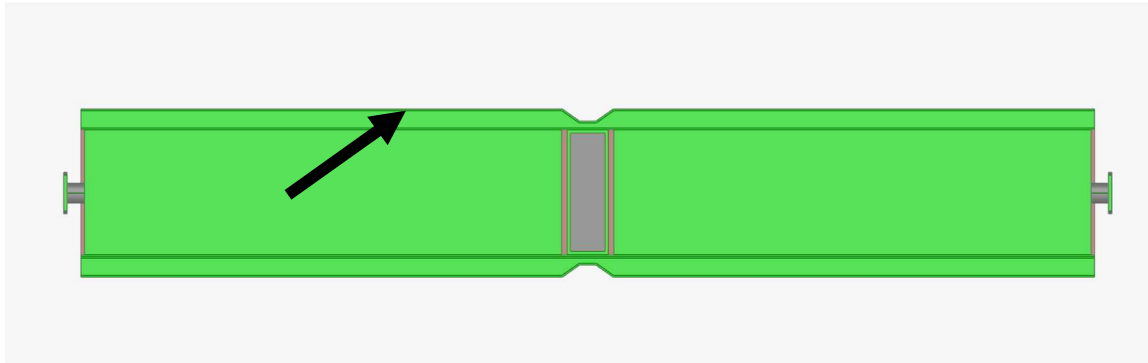
Figure 3.24 - Thickness of the top and bottom cover of the battery housing

3.4.4 Outputs in Thermal analysis

The output response of every minor case in the thermal analysis consists of the average and minimum temperature in the battery module in case in which the temperatures are below operable indicated on the manufacturer, this case consisted of low temperatures, figure 3.25. In the contrary case, the maximum temperature and the average temperature on the battery module, the reason is that in high temperatures it will require to have a cooler temperature due to the manufacturer specifications.
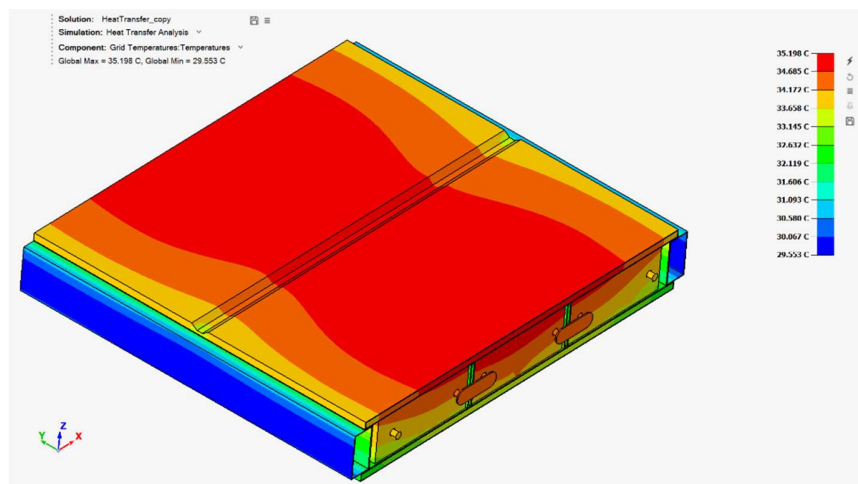
Figure 3.25 - Outputs represented on the first iteration on the design of the battery housing.

The processing phase in crash and thermal simulations represents the core computational step where the mathematical models defined during pre-processing are solved to predict the system's response under specific conditions. This stage transforms the geometrical, material, and boundary condition inputs into actionable insights by performing complex numerical calculations. Each simulation type presents unique challenges, from capturing high-speed impact dynamics in crash scenarios to accurately modeling heat transfer phenomena in thermal analyses. This chapter delves into the processing methodologies, the key computational techniques employed, and the critical considerations necessary to ensure accurate, reliable, and efficient simulation outcomes. By understanding the intricacies of this phase, the robustness of the overall simulation workflow can be evaluated and optimized for real-world applications.

3.5 FEA

The processing phase in computational simulations is a crucial step where numerical models are solved to predict system behavior under specific conditions. For crash and thermal simulations, this phase requires robust solvers capable of handling the unique demands of each scenario. The solvers employed in this research are RADIOSS and OptiStruct, each offering specialized capabilities tailored to the simulation type.

RADIOSS is particularly suited for crash simulations due to its explicit finite element capabilities. It excels in modelling rapid, high-energy impacts where nonlinearities such as large deformations, complex contact interactions, and material failure play significant roles. Its ability to handle transient dynamics and simulate the intricate behaviors of materials under extreme conditions makes it an essential tool for crash analysis.

For thermal simulations, OptiStruct is the solver of choice. It employs implicit methods that are well-suited for steady-state and transient thermal analyses. OptiStruct accurately captures heat transfer mechanisms, including conduction, convection, and radiation, ensuring precise calculation of temperature distributions and thermal gradients within the system.

The selection of the appropriate solver and careful configuration of parameters, such as time steps and convergence criteria, are crucial for ensuring the accuracy and reliability of the simulation results. This sub-chapter details the methodologies and solver configurations employed during the processing phase, providing a comprehensive understanding of how dynamic and thermal behaviors were analyzed effectively.

During the processing phase, continuous monitoring of the simulation is essential to detect any unexpected errors or failures that may arise. These issues could result from numerical instabilities, such as excessive element distortions in crash simulations or divergence in thermal calculations. Monitoring involves tracking solver convergence metrics, reviewing error messages, and validating intermediate results against expected physical behaviors. In case of unforeseen errors, adjustments such as refining the mesh, modifying boundary conditions, or altering solver parameters are implemented to restore stability and ensure the simulation progresses as intended. This proactive approach minimizes disruptions and maintains the reliability of the analysis.

3.6 DOE

The processing of the Design of Experiments (DOE) involves systematically evaluating how variations in design parameters influence the performance of a system. In this study, the focus is on investigating the effects of material thicknesses, ranging from 1 mm to 5 mm, and geometric values varying between -1 and 1. By altering these parameters, a set of design alternatives is generated, which enables exploration of the design space and the identification of optimal configurations. The DOE approach is employed to assess how different combinations of input variables affect key performance criteria, such as structural integrity, thermal behavior, and overall efficiency. This analysis helps uncover potential trade-offs between design choices and provides valuable insights for optimizing the system's performance.

The MELS (Matrix of Experiments for Local Sensitivity) methodology was employed to systematically explore the effects of varying design parameters, such as material thickness and geometric changes, on the system's performance. The MELS methodology involves creating structured matrices that allow for the efficient evaluation of multiple variables, one pair at a time, by fixing one parameter and varying others in a controlled manner. This enables the identification of how individual and combined changes influence the overall behavior of the system.

In this study, the DOE process was implemented using MELS to analyze two variables at a time—specifically, material thicknesses ranging from 1 mm to 5 mm and geometric variations between -1 and 1. These two parameters were chosen for their significant impact on the system's structural and thermal performance. By isolating the influence of each

parameter, the methodology provided a clear understanding of the local sensitivity of the system's performance to these specific changes.

To facilitate the analysis, tables were generated that displayed the combinations of thickness and geometric changes for each experiment. These were organized by the experimental runs, with each row corresponding to a unique combination of the two variables. For example, the first table may show the effect of different thickness values on the system's performance, while another table explores the effects of varying geometric values on the same performance metrics.

These tables 3.10 and 3.11 serve as a concise representation of the design space, allowing for a direct comparison of how different parameter combinations influence key performance indicators.

Table 3-10 - Table of DOE of thicknesses

Experiment	Thickness 1	Thickness 2
1	1.8	2.6
2	2.6	4.2
3	3.4	1.8
4	4.2	3.4
5	1.16	4.52
6	1.96	2.12
7	2.76	3.72

Table 3-11 - Table of DOE of shapes

Experiment	Shape 1	Shape 2
1	-0.6	-0.2
2	-0.2	0.6
3	0.2	-0.6
4	0.6	0.2
5	-0.92	0.76
6	-0.52	-0.44
7	-0.12	0.36

The results derived from the MELS methodology provided valuable insights into the relative importance of thickness and geometry in optimizing the design. This approach enabled a more focused exploration of the parameter space, making it easier to identify critical factors that contribute to the system's performance and inform subsequent optimization steps.

3.7 MDAO

The processing of Multidisciplinary Design Analysis and Optimization (MDAO) involves the integration of various engineering disciplines to evaluate and optimize a system's performance across multiple objectives. This process combines simulations from different domains, such as structural and thermal analysis, into a cohesive framework that allows for the simultaneous analysis of competing design variables. By considering the interdependencies between these disciplines, MDAO facilitates a comprehensive assessment

of design trade-offs and provides optimized solutions that meet specific performance criteria. The processing phase of MDAO typically includes the generation of design alternatives, the application of optimization algorithms, and the evaluation of the results to identify the most effective configuration. This approach enables the design process to move beyond traditional single-discipline analysis, ensuring a more holistic and efficient solution to complex engineering challenges.

In the context of Multidisciplinary Design Analysis and Optimization (MDAO), the selection of solvers is critical to ensuring the accuracy, reliability, and computational efficiency of the simulations. For the present study, two primary solvers were employed: OptiStruct and RADIOSS, each chosen for its specific strengths in addressing the particular types of analyses required.

OptiStruct is an implicit solver primarily utilized for structural and thermal simulations. Its capabilities in performing steady-state and transient analyses make it ideal for linear and nonlinear structural problems. In this study, OptiStruct was used to analyze the system's structural integrity, focusing on material behaviors, stress analysis, and thermal performance. The solver's advanced optimization algorithms were employed to refine the design and improve its overall performance while adhering to the defined constraints. By leveraging OptiStruct, the study was able to explore various design alternatives, optimizing the geometry, material properties, and boundary conditions to achieve an efficient solution that balanced both structural and thermal objectives.

Conversely, RADIOSS is an explicit solver, particularly well-suited for dynamic simulations involving high-energy, short-duration events such as impact and crash scenarios. The solver's explicit formulation makes it ideal for modeling transient loading conditions that involve large deformations, complex material failure, and intricate contact interactions. RADIOSS was utilized in this study to simulate the behavior of the system under crash conditions, capturing the dynamic response of the components under extreme stress. Its ability to accurately model the intricate interactions between components during high-energy events made it essential for performing reliable crash simulations, ensuring that the system's safety and durability were thoroughly assessed.

While selecting the appropriate solvers is essential, ensuring an efficient and reliable workflow throughout the simulation process is equally important. Monitoring the simulations

is necessary to track progress, identify potential issues, and ensure that the results are accurate and meaningful. This involves overseeing various aspects of the simulation, including convergence, error detection, and computational efficiency.

One of the primary aspects of monitoring is the convergence of the solution. During optimization and analysis, convergence ensures that the results, such as force, displacement, and temperature, reach stable values, indicating that the solver has produced a reliable solution. If convergence issues occur, further adjustments may be required, such as modifying solver settings or refining the model to enhance accuracy and stability. For both OptiStruct and RADIOSS, solver-specific diagnostics and error logs were routinely examined to detect potential issues like instability in the model, misapplied boundary conditions, or poor mesh quality, which could lead to erroneous results.

Another key component of monitoring involves computational efficiency, especially for large-scale simulations. Both OptiStruct and RADIOSS can be computationally intensive, particularly when dealing with complex geometries or transient analyses. To maintain an efficient workflow, monitoring tools were used to track CPU usage, memory consumption, and simulation time. This allowed adjustments to be made to the mesh or solver parameters, balancing the trade-off between accuracy and computational cost. For instance, mesh refinement in critical regions was carefully managed to ensure that the simulation captured the necessary details without exceeding the computational resources.

In conclusion, the use of OptiStruct and RADIOSS solvers, combined with diligent monitoring of the simulation process, ensured a smooth and efficient MDAO workflow. By leveraging the unique strengths of each solver and maintaining rigorous oversight of the computational process, the study was able to effectively evaluate and optimize design alternatives. This approach enabled the development of solutions that met the required performance criteria, balancing both structural integrity and thermal efficiency.

Post-processing

The post-processing phase is a critical step in the simulation process, where raw data generated during the analysis is transformed into meaningful insights for decision-making and design optimization. In the context of this study, post-processing was applied to several analyses, including thermal and crash simulations, Finite Element Analysis (FEA), Design of Experiments (DOE), and Multidisciplinary Design Analysis and Optimization (MDAO). For each of these analyses, post-processing played a key role in interpreting the results, verifying the accuracy of the simulations, and guiding the refinement of design parameters. In thermal and crash simulations, post-processing involved extracting temperature distributions, stress concentrations, and deformation patterns to assess component performance under operational conditions. For FEA, the results were analyzed to evaluate the structural integrity of the components and to identify potential areas for improvement. The post-processing of DOE and MDAO simulations enabled the extraction of key design parameters and optimization trends, allowing for the selection of the most efficient design solutions based on multiple performance criteria. This chapter discusses the techniques and methodologies employed in post-processing, providing a comprehensive understanding of how the results from these various analyses were interpreted and used to inform the final design decisions.

3.8 Benchmark

Post-processing benchmark analysis plays a crucial role in extracting valuable insights from the simulation results, enabling a deeper understanding of how the system performs under various conditions. In this context, benchmark analysis refers to the process of evaluating and validating the results of simulations—such as thermal and crash analyses—against established standards or reference models. The post-processing phase involves analyzing key metrics, such as stress distributions, temperature gradients, material behavior, and deformation patterns, to assess the accuracy and reliability of the simulation. This step is essential for verifying that the model behaves as expected under real-world conditions and ensuring that the design meets the necessary performance and safety criteria. The results from benchmark analysis are used to identify any discrepancies, refine the model, and guide design

optimizations. This chapter outlines the methods and techniques employed in post-processing benchmark analysis, focusing on how data is interpreted and applied to inform subsequent design iterations.

3.8.1 Thermal

Post-processing of benchmark analysis in thermal simulations plays a crucial role in assessing the thermal performance of a system and verifying its design against real-world operating conditions. After completing the thermal analysis, the post-processing phase involves interpreting key results such as temperature distribution, heat flux, and thermal gradients across the components. These results are essential for evaluating the efficiency of heat dissipation, identifying potential hotspots, and ensuring that the system operates within the desired thermal limits. In thermal simulations, it is important to compare the simulated temperature profiles to benchmark data or experimental results to confirm the accuracy and validity of the model. The post-processing phase also includes identifying areas where thermal stresses may cause material deformation or failure, and it provides insights into potential design improvements for better heat management. This chapter outlines the methods used in post-processing thermal benchmark analysis, focusing on how thermal data is analyzed to optimize designs for thermal efficiency, safety, and performance.

Temperature distribution

In the post-processing phase of an MDAO framework applied to the thermal analysis of battery housing, evaluating the temperature distribution is critical to understanding the thermal behavior of the system. This analysis provides insights into how heat is dissipated across the housing and identifies regions with high-temperature gradients or potential hotspots, which could compromise the material integrity or the safety of the battery cells. The simulation results are analyzed to visualize the surface and internal temperature profiles, revealing the effectiveness of heat transfer mechanisms such as conduction, convection, and radiation. Particular attention is given to transient and steady-state conditions, ensuring that the design performs reliably under varying operational scenarios.

To validate the simulation, the temperature profiles are compared against experimental benchmark data, enhancing confidence in the accuracy of the model. The findings from the temperature distribution analysis inform design decisions, such as optimizing the housing

material for improved thermal conductivity, enhancing cooling channel configurations, and mitigating thermal gradients to reduce stresses. These insights enable the iterative improvement of the battery housing design, ensuring compliance with thermal performance objectives, safety standards, and material constraints. Visualization tools, including contour plots and vector fields, further aid in interpreting the thermal behavior and support the development of more efficient, durable, and cost-effective designs can be visualized in the next figure 3.26.
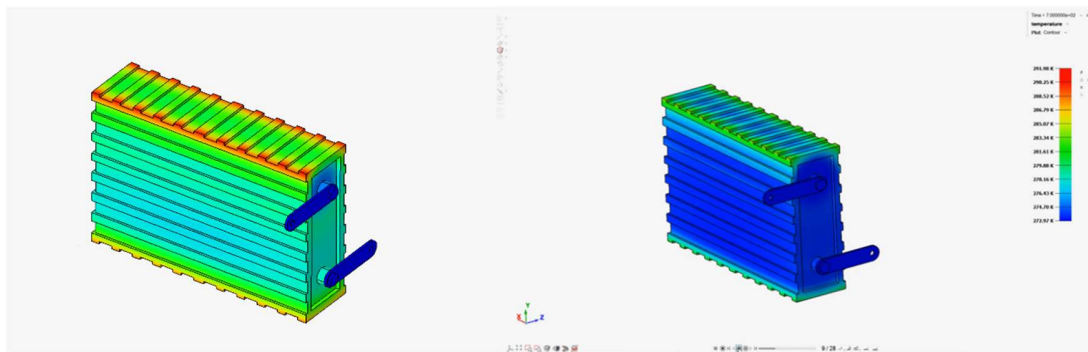
Figure 3.26 - Post-processing on the thermal analysis

Hotspots

Evaluating hotspots during the post-processing phase of the MDAO framework is key to making sure the battery housing design performs well thermally and remains reliable. Hotspots—areas where heat builds up—can weaken materials and put battery cells at risk of failure or thermal runaway. By reviewing thermal simulation results, these critical zones are identified and analyzed to understand why they occur and how they affect the overall design. This involves checking for poor heat dissipation, uneven material behavior, or flaws in the cooling layout. Beyond just locating the hotspots, the analysis also looks at how heat moves around them to find the root causes. Comparing these findings with real-world data or reference models helps confirm that the design is both safe and effective.

Addressing hotspots through targeted design changes is a key outcome of this evaluation. Strategies may include modifying cooling channel designs, selecting higher-conductivity materials, or altering the geometry of the housing to improve heat dispersion. The use of post-processing visualization techniques, such as thermal maps and cross-sectional temperature profiles, aids in clearly presenting the findings and identifying actionable

solutions. Through this iterative process, hotspot analysis drives enhancements in the thermal efficiency, safety, and durability of the battery housing design. All of this can be observed in the figure 3.27, emphasizing in the hotspots in the placement on 3 a just 1 battery.
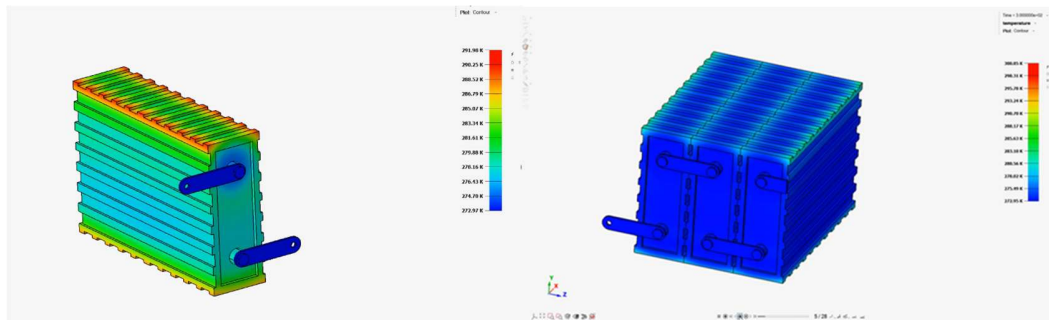
Figure 3.27 - Partial results on batteries stacked

3.8.2 Crash

Post-processing crash simulation benchmarking plays a key role in understanding how components perform under impact. After running the simulation, engineers extract results like deformation shapes, stress levels, and energy absorption to see how the system reacts during a crash. This helps verify if the model meets safety standards and reflects real-world behavior. By studying the data, weak points can be identified, and the performance of protective structures can be assessed. The results are also compared with physical tests or reference benchmarks to confirm the model's accuracy. This chapter focuses on the tools and methods used to interpret crash data and how those insights support safer, more effective design improvements.

Deformation patterns

Lateral crash tests are a critical aspect of vehicle safety evaluation, focusing on the structural integrity and energy absorption capabilities of a system when subjected to side-impact forces. The deformation patterns observed in these tests provide invaluable insights into how components respond to high-energy impacts, including the distribution of stresses and strains across critical areas. By analyzing these patterns, the research identifies regions of structural weakness, potential failure points, and areas where energy absorption can be optimized.

In a typical lateral crash scenario, the deformation begins at the point of contact, where the energy of impact is initially absorbed. This leads to localized compression and bending, often

resulting in plastic deformation in key structural members such as side rails, doors, and impact beams. The patterns spread radially from the impact site, with deformation magnitudes varying based on material properties, geometry, and connection points between components. These patterns are essential for understanding the load paths and how effectively the structure mitigates forces to protect occupants.

Special attention is given to regions where significant deformation could lead to intrusion into the occupant space. For example, excessive displacement of the side doors or pillars could compromise passenger safety. The analysis identifies whether these regions meet safety criteria, such as those outlined by international crash safety standards. Additionally, the behavior of welded joints, fasteners, and connections between dissimilar materials is closely monitored, as these areas are often prone to failure under extreme stress.

The research also investigates the role of design variables in influencing deformation patterns. By comparing deformation results across multiple design configurations, the study identifies how adjustments in material thickness, reinforcements, or component geometries can enhance the system's performance during lateral impacts. This knowledge guides the development of more robust designs that improve energy absorption and reduce intrusion risks.

The analysis of deformation patterns in lateral crash tests provides a comprehensive understanding of structural behavior under side-impact scenarios. These insights are instrumental in refining designs to enhance vehicle safety and ensure compliance with regulatory standards. Through detailed examination of these patterns, the study highlights areas for potential improvement and contributes to the advancement of safer, more resilient vehicle structures.

Figure 3.28 and 3.29 illustrates a representative deformation pattern observed in a lateral crash scenario. The figure highlights the localized compression at the initial impact zone, the progressive deformation along the side structure, and the resulting displacement of critical components such as the side doors and B-pillar. Color-coded stress contours indicate areas of high strain, particularly around joint connections and reinforcements, emphasizing the critical regions that require optimization. This visual representation supports the textual analysis by providing a clear depiction of how forces propagate and affect the structural integrity of the vehicle during a lateral crash.
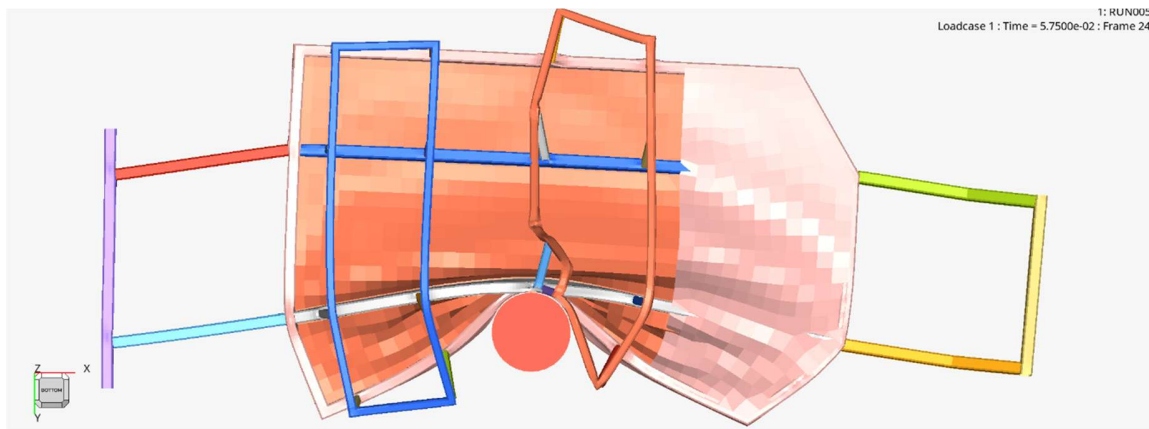
Figure 3.28 - Upper view on side impact
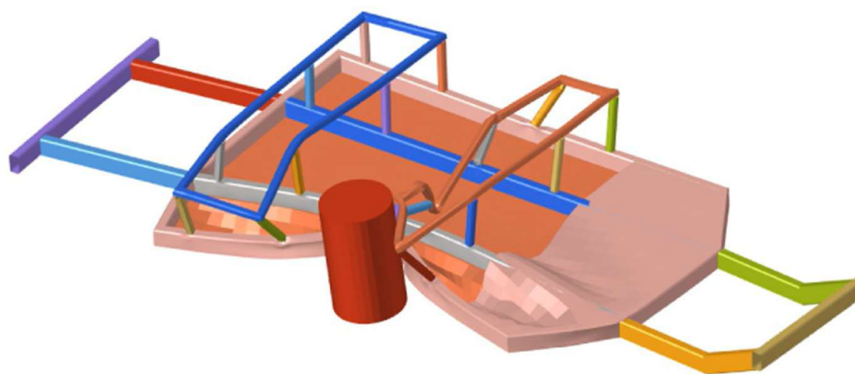
Figure 3.29 – Isometric view on side impact

Stress strain distribution.

Understanding stress and strain distribution in lateral crash tests is essential for evaluating how effectively a vehicle structure absorbs and manages impact energy. These tests simulate real-world side collisions, where components like the side doors, B-pillar, and floorpan are subjected to sudden and uneven loading. The highest stress typically occurs at the point of impact, gradually reducing as the energy is redirected and absorbed by reinforcements and crumple zones. Stress analysis helps pinpoint which structural paths carry the most load, identifying areas where reinforcement may be needed. Meanwhile, strain analysis reveals how different sections deform under crash loads, especially around critical points like welds, joints, or geometric transitions that tend to show complex deformation behavior. For

111

instance, in a side impact, the B-pillar may experience bending, while surrounding sheet metal panels stretch or compress to help reduce intrusion into the cabin. Studying these behaviors provides actionable insights for improving material selection, joint design, and structural geometry, ultimately enhancing occupant protection and vehicle crashworthiness. Figure 3.30 shows the Von Mises stress distribution resulting from a lateral crash simulation. The contour plot uses a color gradient to illustrate stress levels, with red indicating areas of maximum stress and blue representing regions with minimal loading. Significant deformation is observed near the side impact area, particularly around structural joints and interface zones. These high-stress and strain regions reveal how the structure absorbs and redirects impact energy. The visualization underscores the need for targeted reinforcements and optimized material selection in these critical zones to improve crashworthiness and minimize structural failure during side impacts.
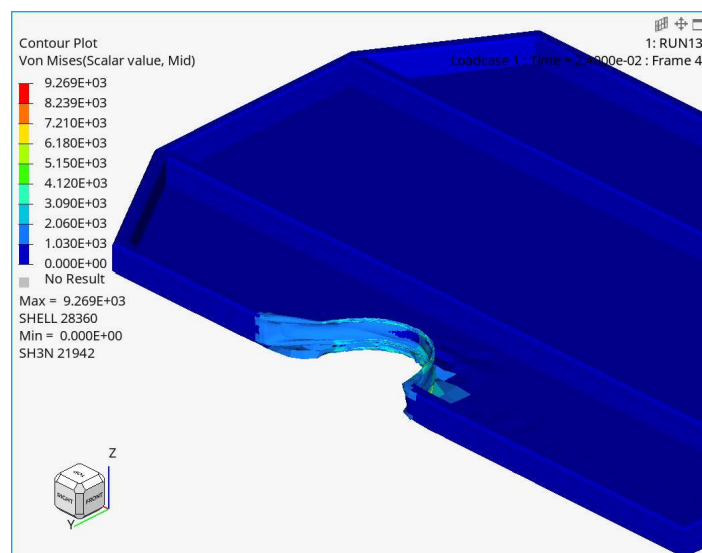
Figure 3.30 Isolated view on side impact of internal structure

The analysis of stress-strain distribution underscores the importance of balancing material strength and ductility in vehicle design. High-strength materials are required in areas subjected to extreme stress to prevent failure, while ductile materials in other regions ensure controlled energy absorption and deformation. This balance is a key consideration in designing safe and reliable vehicle structures capable of withstanding side impacts effectively.

Energy absorption

Energy absorption plays a critical role in lateral crash tests, as it determines how effectively a vehicle can mitigate the forces resulting from a side impact to protect occupants. The ability of a structure to absorb and dissipate energy during a crash minimizes the transfer of forces to the passenger compartment, reducing the likelihood of injury. The analysis of energy absorption focuses on the behavior of critical components, such as the side impact beams, crumple zones, and reinforcements, which are designed to deform in a controlled manner.

During a lateral crash, kinetic energy generated by the vehicle's motion is converted into internal energy within the structure through plastic deformation and localized material failure. Crumple zones are engineered to absorb a significant portion of this energy, ensuring a progressive collapse that mitigates peak forces. Reinforcements, such as the B-pillar and door beams, work to contain the deformation within specific zones, preventing excessive intrusion into the passenger cabin.

The distribution of absorbed energy varies across the structure, with higher concentrations observed near the point of impact and along the load transfer paths. For example, the side impact beam absorbs the initial kinetic energy, while adjacent panels and reinforcements contribute to dissipating the residual forces. This distribution ensures that energy is managed effectively, safeguarding the structural integrity of the vehicle's safety cell.

Figure 3.31 illustrates the energy absorption characteristics during a lateral crash simulation. The graph displays the variation of internal energy and kinetic energy over time. The internal energy curve represents the energy absorbed by the structure through deformation, showing a steady increase as the impact progresses. The kinetic energy curve, on the other hand, depicts a rapid decline, indicating the conversion of motion energy into structural deformation. The intersection of these curves marks the point where the vehicle has absorbed most of the impact energy, leaving minimal residual kinetic energy to affect the passenger compartment.
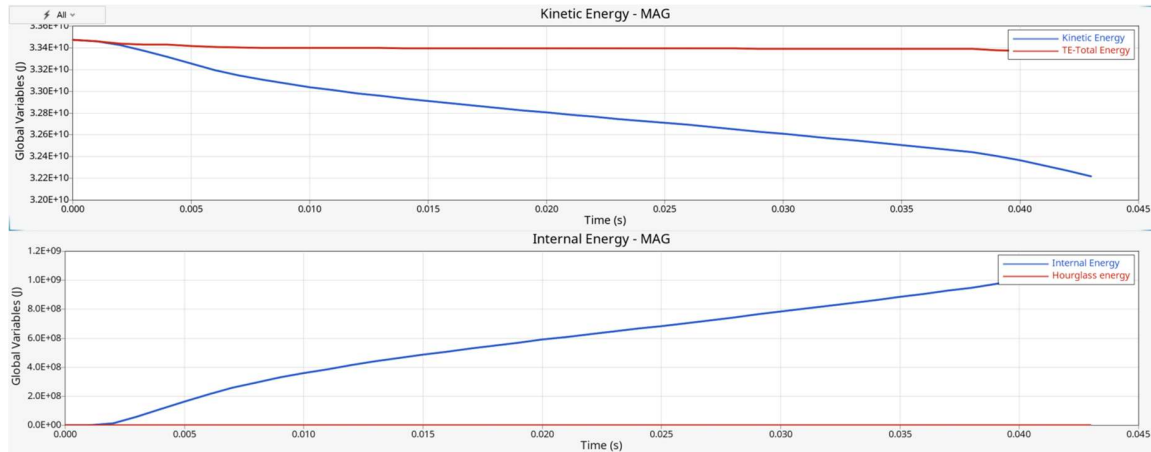
Figure 3.31 – Internal and kinetic energy on the postprocessing of the original design

The graphical representation emphasizes the importance of designing components with optimal energy absorption capabilities. Reinforcing materials and strategic placement of crumple zones enhance the vehicle's ability to manage energy effectively. By correlating the internal and kinetic energy curves, engineers can evaluate the efficiency of the energy absorption process and identify areas for further improvement in crashworthiness.

3.9 FEA

The Finite Element Analysis (FEA) and base analysis conducted in this thesis serve as fundamental tools for evaluating the mechanical behavior and thermal performance of the system under various conditions. FEA is employed to discretize complex geometries into smaller, manageable elements, enabling the simulation of real-world physical phenomena such as stress, strain, and temperature distribution within a component or assembly. The base analysis includes static and dynamic evaluations, considering factors like material properties, boundary conditions, and load applications, to assess the system's structural integrity and thermal response. By using FEA, the research explores how different design configurations, material choices, and environmental factors influence the system's performance, providing crucial insights for optimization and decision-making in the design process. This approach allows for the identification of critical areas that require further refinement and offers a comprehensive understanding of the system's behavior in both normal and extreme conditions.

3.9.1 Base analysis

The concept of the base analysis implemented in the Multidisciplinary Design Analysis and Optimization (MDAO) framework plays a crucial role in evaluating the performance of a system under various design configurations and operational conditions. In this context, the base analysis serves as the foundational assessment for each design iteration, providing essential data on the system's mechanical, thermal, or fluidic behavior before any optimization or refinement is performed. This initial analysis is used to establish the baseline performance of the system by considering key parameters such as material properties, loading conditions, and geometric configurations. The results from the base analysis are then integrated into the MDAO process, where they are iteratively used to assess how different design variables impact the system's overall performance. By incorporating base analyses into the MDAO, this research ensures that design decisions are informed by accurate and reliable simulations, allowing for the optimization of key parameters to meet specific performance goals, such as minimizing weight, improving strength, or enhancing thermal efficiency. The base analysis thus acts as a critical starting point that guides the subsequent steps of the optimization process.

Crash

The post-processing phase of crash analysis within an MDAO framework is crucial for evaluating the structural performance of a design under impact conditions. This stage involves the interpretation of simulation outputs to assess key metrics such as energy absorption, deformation patterns, stress distribution, and failure points. These outputs provide valuable insights into the ability of the structure to withstand crash scenarios and maintain occupant safety. The analysis also identifies areas requiring reinforcement or redesign to improve crashworthiness and optimize material usage.

Visualizing results through detailed graphics plays a central role in the post-processing phase. Outputs such as deformation contour plots, energy absorption curves, and stress maps highlight critical regions where the structure experiences the highest impact forces. Time-based animations of the crash sequence further aid in understanding the dynamic behavior of the system during impact. By integrating these visual tools with quantitative data, engineers

can effectively evaluate the performance of the base design and explore iterative improvements within the MDAO framework. This approach ensures the development of safer and more efficient designs that meet stringent safety standards and performance objectives.

Output

The outputs generated during the post-processing phase of crash analysis in an MDAO framework provide a comprehensive understanding of the structural behavior under impact conditions can be seen in table 3.12. Key outputs include deformation profiles, which illustrate the extent and location of structural displacement, and stress-strain distributions that identify areas of material failure or yielding. Additional metrics, such as total energy absorption, kinetic energy dissipation, and contact forces, are critical for evaluating the effectiveness of the design in mitigating crash impacts. These outputs also quantify the structural integrity and occupant safety by assessing factors like intrusion into protected zones and load transfer pathways. By analyzing these results, engineers can pinpoint weaknesses in the base design and make data-driven decisions to enhance crashworthiness, ensuring compliance with safety standards and optimization objectives.

Table 3-12 – Table of inputs and variables on the battery housing side panel (BHSP)

Variables	BHSP-1	1.8
	BHSP-2	2.6
Outputs	Internal Energy - MAG	3.53E+08
	Kinetic Energy - MAG	3.26E+10
	Contact energy - MAG	1.37E+07
	Mass - MAG	851.72711
	2 accelerometer2 - ACC-Resultant Acceleration	0.4783807
	477716 - AX-X Acceleration	0.005295
	2 accelerometer2 - AX-X Acceleration	0.4144818
	2 accelerometer2 - AX-X Acceleration	-0.005295
	1 group1 - FX-X Total Force	8.33E+07

Graphic

Graphics in image 3.32 play a pivotal role in visualizing and interpreting the results of crash analysis within the MDAO framework. By transforming raw simulation data into detailed

visual representations, engineers can better understand the structural response to impact scenarios. Commonly used graphics include deformation contour plots, which highlight areas of displacement and potential structural failure, and stress distribution maps that reveal critical stress concentrations across the design. Energy absorption graphs and time-sequenced animations further illustrate how impact energy is distributed and dissipated throughout the structure during the crash event. These graphical tools not only facilitate the identification of weaknesses and improvement opportunities but also enhance communication of findings to stakeholders. By providing a clear and intuitive understanding of the crash performance, graphics support iterative design optimization and ensure that safety and performance goals are achieved.
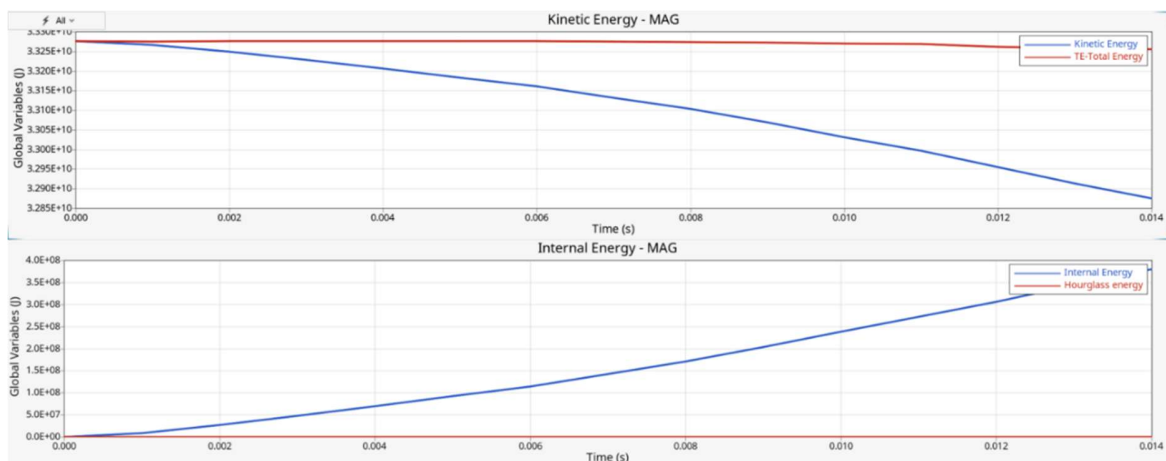
Figure 3.32 - Graphic on the kinetic energy and internal energy on the proposed design

Thermal

Post-processing in the thermal analysis stage of an MDAO framework is crucial for evaluating the system's heat management performance and informing design optimizations. This phase involves interpreting key results such as temperature distributions, thermal gradients, and heat flux patterns to assess heat dissipation efficiency and pinpoint critical areas like hotspots or zones with elevated thermal stress. These findings are essential to ensure that the design complies with performance and safety requirements under real-world operating conditions.

Visual representations significantly enhance the interpretation of simulation data. Tools such as temperature contour plots, heat flux vectors, and gradient overlays offer an intuitive understanding of how thermal energy flows and accumulates throughout the structure. These

graphics make it easier to detect thermal bottlenecks and communicate results effectively to design teams and stakeholders. By combining quantitative data with clear visual insights, the post-processing phase plays a key role in guiding iterative improvements and reinforcing thermal reliability across the MDAO process.

Outputs

The outputs on table 3.13 generated during the thermal analysis post-processing phase provide essential data for evaluating the system's thermal performance. Key outputs include detailed temperature distributions across the components, which reveal areas experiencing excessive heat or insufficient heat dissipation. Heat flux data is also crucial, as it indicates the rate at which heat is transferred within the system, helping to identify potential thermal bottlenecks or inefficiencies. Additionally, thermal gradient outputs allow for the assessment of how heat varies spatially within the system, highlighting regions where rapid temperature changes could lead to material stresses or failure. These outputs are critical for assessing whether the design remains within safe operational limits and supports informed decisions regarding material selection, cooling strategies, and overall thermal management.

Table 3-13 – Table of variables and outputs on thermal analysis in upper and lower cover

Variables	L1	20
	L2	6
Outputs	Heat Transfer : Mass	189.409
	Heat Transfer : UP-MAX	1234.15
	Heat Transfer : UP-AVG	192.775
	Heat Transfer : SUN-AVG	190.402
	Heat Transfer : SUN-MAX	1234.15
	Heat Transfer : BOTTOM-MAX	1091.21
	Heat Transfer : BOTTOM-AVG	207.171
	Mass	178.56315
	UP-MAX	1.59E+07

3.10 DOE

The design process for the external crash structure of the battery housing involved a comprehensive approach to optimizing the geometric and thickness variables of sheet metal components. The objective was to create a structure that not only meets the desired safety requirements but also adheres to design constraints related to material properties and manufacturing capabilities. The process, incorporated various design iterations with different sheet metal thicknesses and shapes. These variables were strategically paired and evaluated through a series of experiments using the MELS (Multidisciplinary Experimentation and Simulation) method. An algorithm was used to analyze and select the best combinations, with regression models helping to refine the design and identify optimal solutions. Despite challenges in achieving the desired R-values, the analysis provided valuable insights into the behavior of key parameters, laying the groundwork for further refinement of the design.

3.10.1 BH-1

The process in which the first design of the external crash structure had the next procedure along with the variables, both geometric and from thicknesses, according to each one. The design of this external crash structure, figure 3.33, consists of sheet metal components with their desired thicknesses.
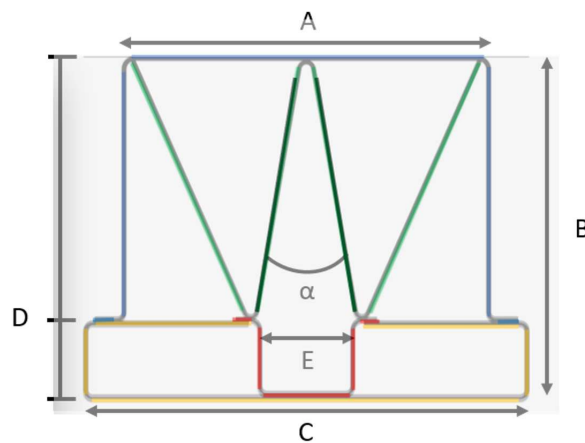
Figure 3.33 - BH-1 Battery housing side crash structure number 1

In this design the variables were split into thicknesses and shapes, according to each one and their pairing, it was selected the best option on the selection on each one. With this the algorithm was runner and found the best option of regression possible

The best regressions chosen were LSR and MLSM depending on the output, however the value R did not reach the expected value between 0.75 and one. This propose a challenge just choosing the values that need to be optimized.

In table 3.14 the results of "R" are presented, giving us the regression outputs on all the variables further explained.

Table 3-14 - BH-1 Provisional Results of regression on outputs of value R

BH-1 design		Blue - Green	Red - Yellow	SHAPE-1/2	SHAPE-3/4	SHAPE-5
Internal Energy	RBF	0.999585	0.953004	0.786859	0.758462	0.288319
Kinetic Energy	MLSM	0.999890	0.999637	0.998942	0.872012	-0.777778
Total energy	MLSM	0.999946	0.999914	0.999960	0.961219	0.896837
Mass	LSR	1.000000	1.000000	0.999892	0.992880	0.999725
X-Momentum	MLSM	0.999968	0.999982	0.999725	0.818755	0.935864
Central acceleration M	LSR	0.263052	0.945366	0.778888	0.685619	-0.052471
Central acceleration I	MLSM	0.735693	0.855274	-0.286882	0.816292	0.650090
Central acceleration R	LSR	0.338427	0.912656	-0.288096	-0.361111	-0.089118
Central acceleration Mi	MLSM	0.690905	0.974927	-0.005099	-0.361111	-0.741294
Total energy	MLSM	0.999946	0.999914	0.999960	0.961219	0.896837
Acceleration node 58623	RBF	-0.082570	0.504094	0.943079	0.069914	0.103086
Acceleration node 58623 R	MLSM	0.598370	-0.361111	0.584242	-0.136986	-0.777778

Thicknesses

The study explored variations in sheet metal thickness across 14 experiments in table 3.15, conducted in two runs of seven each. Thickness values ranged from 1 to 5 mm, with two pairs examined: BHSP-1 and BHSP-2 in the first iteration, and BHSP-3 and BHSP-4 in the second. Using MELS, experiments were analyzed through a fitting algorithm alternating regression type, employing the FAST parameter for optimal fit.

In both iterations, the best regressions—LSR and MLSM—were selected. However, R-values failed to meet the target range of 0.75 to 1, presenting challenges in optimizing values. Despite this, key parameters such as kinetic energy, internal energy, total energy, model

mass, X-momentum, and central node acceleration consistently exceeded an R-value of 0.65. These parameters were deemed reliable for further analysis.

For BHSP-1 and BHSP-2, optimization produced scatter plots correlating model weight (X-axis) with output behavior as shell thickness increased. Similarly, BHSP-3 and BHSP-4 demonstrated analogous trends, providing insights into how outputs responded to varying thicknesses.

Node 58623's acceleration was included as an additional output but had no significant impact on optimization decisions. The study highlighted limitations in achieving regression criteria for certain outputs, emphasizing challenges in parameter optimization within the given constraints.

Table 3-15 - BH-1 Provisional Results of analysis of thicknesses

#	1	2	3	4	5	6	7	#	1	2	3	4	5	6	7
Blue	1.8	2.6	3.4	4.2	1.16	1.96	2.76	Red	1.8	2.6	3.4	4.2	1.16	1.96	2.76
Green	2.6	4.2	1.8	3.4	4.52	2.12	3.72	Yellow	2.6	4.2	1.8	3.4	4.52	2.12	3.72
Internal energy	3.74E+08	4.80E+08	3.91E+08	4.89E+08	4.45E+08	3.55E+08	4.64E+08	Internal energy	4.06E+08	4.46E+08	4.18E+08	4.60E+08	4.18E+08	3.94E+08	4.39E+08
Mass	855.48	870.63	858.31	873.46	865.33	853.01	868.16	Mass	858.54083	868.42719	860.50757	870.39398	864.87653	856.95691	866.84326
Momentum in X	-7189137.0	-7299628.0	-7209660.5	-7320135.5	-7260235.0	-7171496.5	-7282102.5	Momentum in X	-7209982.5	-7285474	-7224282.5	-7298832.5	-7260108	-7197803.5	-7272877.5
Accel. Central	0.0153	0.0052	0.0163	0.0198	0.0063	0.0245	0.0064	Accel. Central	0.0039083	0.060114	0.0041181	0.0375128	0.0532478	0.0033792	0.043992
Accel Central Integral	1.85E-05	7.73E-06	2.21E-05	8.17E-06	1.08E-06	2.56E-05	1.63E-05	Accel Central Integral	9.83E-07	2.23E-05	7.11E-07	1.35E-05	1.95E-05	5.44E-07	1.18E-05
Resultant central acceleration	0.107	0.096	0.142	0.138	0.094	0.088	0.096	Accel. Central Resultant	0.018231	0.251996	0.066015	0.193609	0.191918	0.052711	0.164805
Kinetic energy	3.28E+10	3.32E+10	3.28E+10	3.33E+10	3.31E+10	3.27E+10	3.32E+10	Kinetic Energy	3.28E+10	3.32E+10	3.29E+10	3.32E+10	3.31E+10	3.28E+10	3.31E+10
Accel. Cent. Min	-2.940E-08	-2.815E-02	-4.709E-02	-1.224E-01	-5.475E-02	-2.300E-08	-1.521E-02	Accel. Cent. Min	-0.01520	-0.24797	-0.03254	-0.17426	-0.18437	-0.03347	-0.16260
Total Energy	3.31E+10	3.37E+10	3.32E+10	3.38E+10	3.35E+10	3.30E+10	3.36E+10	Total Energy	3.32E+10	3.36E+10	3.33E+10	3.37E+10	3.35E+10	3.32E+10	3.36E+10
Node AX-X	109393.2	74592.6	31733.7	82388.5	86569.2	62287.2	124892.3	Node AX-X	87942.5	38311.7	77749.7	58949.84	84482.1	75770.68	50718.53
Node-ACC	742091.8	666796.9	321932.5	333736.5	840223.3	420380.8	613154.3	Node-ACC	398946.6	269177.3	235159.1	476271.6	325490.5	309100.6	510121.2

Geometry variables

Similarly to the variable of the thickness, two designs were paired for them to observe the behavior and consist of seven experiments with two runs and the fifth design was experimented on in a separate environment.

In the geometric variables there are five variations on the design as we can see below on figures 3.34.
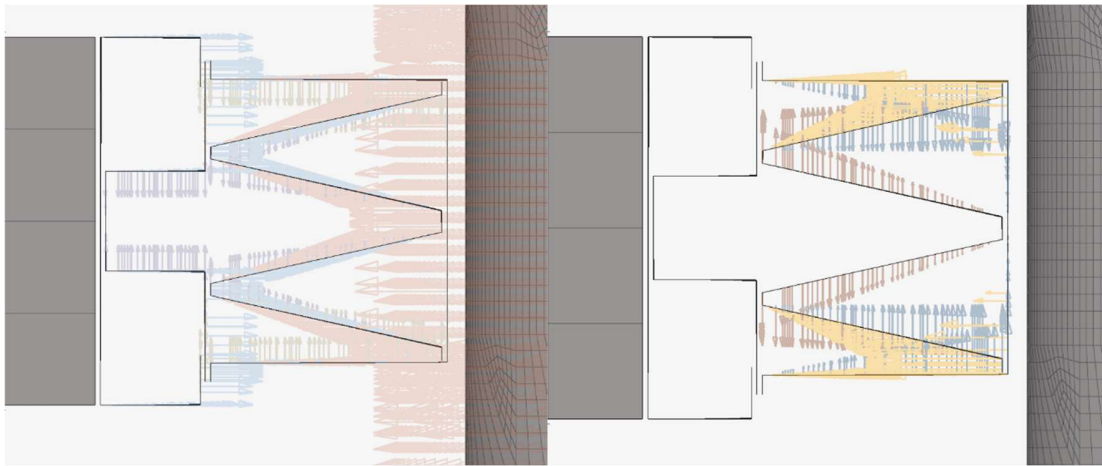
Figure 3.34 - Geometric variables proposed on the BHSP 1st design

In the first iteration, shapes 1 and 2 ranged between one and -1, with experiments designed using MELS based on proposed outputs. The results were analyzed using a fitting algorithm that alternates between regression types for viable outputs, employing the FAST parameter for optimal mathematical fit. Despite selecting LSR and MLSM as the best regressions, the R-value did not reach the target range of 0.65 to 1, complicating the optimization process.

Some outputs, however, were considered reliable. Parameters such as kinetic energy, internal energy, mass, X-momentum, central node acceleration, and total energy consistently achieved R-values above 0.65. While the acceleration at node 58623 was included as an additional output, its lower R-value did not significantly affect optimization decisions.

In the second iteration, shape 3 values ranged from 1 to 0, while shape 4 values ranged between -0.4 and 1. Using MELS, the outputs were again evaluated with the fitting algorithm. Although LSR and MLSM were the preferred regressions, the R-values remained below the desired range, presenting further challenges in selecting optimization values.

The reliable parameters from the first iteration—kinetic energy, internal energy, mass, X-momentum, central node acceleration, and total energy—remained consistent. Acceleration at node 58623 continued to be an additional output, but its lower R-value did not hinder decision-making.

It is important to note that only shapes 1 and 2 changed, maintaining a static shell element thickness of 3 mm. This ensured consistency across iterations.

In the fifth iteration, sheet metal values ranged between 1 and -1, and MELS experiments were conducted accordingly. Unfortunately, the chosen regressions failed to meet the R-value criterion, making the results unsuitable for reliable predictions.

These challenges highlight the difficulties in achieving accurate regressions within the specified constraints. Improvements in modeling approaches or regression techniques may be necessary to optimize outputs and enhance prediction reliability.

Table 3-16 - BH-1 Provisional Results of analysis of the variation on shape five

#	1	2	3	4
Shape five	0.475	0.0875	0.8625	-0.10625
Internal energy	4.23E+08	4.35E+08	4.26E+08	4.34E+08
Masa	864.26935	864.43042	864.11243	864.51257
Momentum in X	-7254074.5	-7254661	-7253094	-7255069
Accel. Central	0.0058244	0.0090331	0.0064982	0.0179852
Accel Central Integral	1.15E-06	1.92E-05	1.39E-06	2.76E-05
Accel. Central Resultant	0.0618855	0.1069494	0.0757193	0.2247467
Kinetic Energy	3.30E+10	3.30E+10	3.30E+10	3.30E+10
Accel. Centre. Min	-0.0561633	-0.0045446	-0.06717	-0.05068
Total Energy	3.35E+10	3.35E+10	3.35E+10	3.35E+10

Table 3-17 - BH-1 Provisional Results of analysis of shapes

#	1	2	3	4	5	6	7	#	1	2	3	4	5	6	7
Shape 1	-0.6	-0.2	0.2	0.6	-0.92	-0.52	-0.12	Shape 3	-0.12	0.16	0.44	0.72	-0.344	-0.064	0.216
Shape 2	-0.2	0.6	-0.6	0.2	0.76	-0.44	0.36	Shape 4	0.4	0.8	0.2	0.6	0.88	0.28	0.68
Internal energy	4.20E+08	4.26E+08	4.35E+08	4.36E+08	4.08E+08	4.29E+08	4.29E+08	Internal energy	4.36E+08	4.42E+08	4.36E+08	4.40E+08	4.39E+08	4.36E+08	4.40E+08
Masa	860.97333	862.65656	866.29327	867.9765	858.16382	861.69513	863.37836	Masa	864.76624	865.05463	864.62982	864.9397	865.16534	864.67352	864.96411
Momentum in X	-7225731.5	-7239893	-7269118.5	-7284733.5	-7203877	-7230929	-7246382.5	Momentum in X	-7256620.5	-7258605	-7256454	-7257416	-7259256	-7255676	-7257970.5
Accel. Central	0.0286836	0.007917	0.0158031	0.0289002	0.0875817	0.0341061	0.0080318	Accel. Central	0.006185	0.0344697	0.0046677	3.49E-04	0.0428224	0.0065507	0.0245682
Accel Central Integral	1.01E-05	1.25E-05	3.53E-05	1.68E-05	9.52E-05	1.07E-05	1.38E-05	Accel Central Integral	1.41E-05	9.47E-07	6.62E-06	1.55E-06	3.99E-07	1.48E-05	1.38E-06
Accel. Central Resultant	0.1287265	0.0424241	0.1988062	0.0376191	1.0580393	0.1754587	0.0760618	Accel. Central Resultant	0.0721306	0.0423113	0.0087056	0.1177262	0.045249	0.0919003	0.0490594
Kinetic Energy	3.29E+10	3.30E+10	3.31E+10	3.32E+10	3.28E+10	3.29E+10	3.30E+10	Kinetic Energy	3.31E+10	3.31E+10	3.30E+10	3.31E+10	3.31E+10	3.31E+10	3.31E+10
Accel. Centre. Min	-0.1188752	-0.0038564	-0.0193404	-7.76E-09	-0.8486527	-0.1633951	-0.0201494	Accel. Centre. Min	-3.10E-08	-0.0054282	-0.0039171	-0.0035737	-0.0088218	-0.0058323	-0.0035045
Total Energy	3.33E+10	3.34E+10	3.35E+10	3.36E+10	3.32E+10	3.34E+10	3.34E+10	Total Energy	3.35E+10	3.35E+10	3.35E+10	3.35E+10	3.35E+10	3.35E+10	3.35E+10
Node AX-X	57250.145	42478.484	100957.09	79063	18381.092	68237.016	61338.637	Node AX-X	87942.578	38311.758	77749.758	58949.84	84482.133	75770.68	50718.531
Node-ACC	384530.44	326611.5	354595.63	285649.72	439765.66	364311.38	256617.13	Node-ACC	398946.63	269177.38	235159.17	476271.66	325490.59	309100.63	510121.25

3.10.2 BH-2

The process in which the first design of the external crash structure had the next procedure along with the variables, both geometric and from thicknesses, according to each one. The design of this external crash structure, figure 3.35, consists of sheet metal components with their desired thickness.
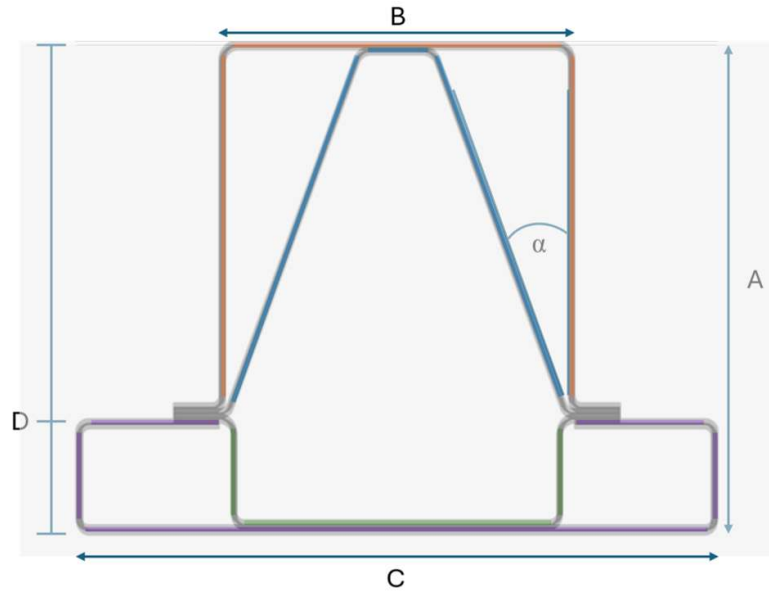
Figure 3.35 - BH-2 Battery housing side crash structure number 2

In this design the variables were split into thicknesses and shapes, according to each one and their pairing, it was selected the best option on the selection on each one. With this the algorithm was runner and found the best option of regression possible

The best regressions chosen were LSR and MLSM depending on the output, however the value R did not reach the expected value between .75 and one. This proposes a challenge just choosing the values that need to be optimized.

In table 3.18 the results of "R" are presented, giving us the regression outputs on all the variables further explained.

Table 3-18 - BH-2 Provisional Results of regression on outputs of value R

BH-2		Orange - Blue	Green - Purple	SHAPE- 1/2	SHAPE- 3/4	SHAPE- 5/6
Internal Energy	RBF	0.98673	0.94505	0.749087	0.846936	0.692115
Kinetic Energy	LSR	0.99989	0.99912	0.998318	0.906672	0.958869
Contact energy	MLSM	0.52567	0.83575	0.844202	-0.201777	0.293001
Mass	LSR	1	1.00000	0.999814	0.997832	0.998621

Resultant Acceleration 477716	MLSM	0.55694	0.96739	0.749811	0.277412	0.766386
Acceleration AX-X	RBF	0.42644	0.92022	-0.361111	0.380789	0.937249
Acceleration accelerometer2	MLSM	0.97002	0.81384	0.538198	-0.357676	-0.361111
- AX-X	RBF	0.42644	0.92022	-0.361111	0.380789	0.937249

Thicknesses

The variables in thickness were paired in external and internal, this constitutes the thicknesses that were explored in fourteen different experiments with two runs of seven each. The first pair explored was the thickness in the BHSP-1 and 2 and the second pair is in the BHSP-3 and 4.

In the first pair and second pair of the iteration, the value of the sheet metal was between 1 and 5 mm, and the values chosen for the design of experiments using MELS with the results of the proposed outputs were as follows.

In these results the values of the mathematical model that will be taken almost 100% granted are total energy, kinetic energy, internal energy, acceleration on central node, momentum on X. Every single output in this has a value above 0.65.

The optimization on the thicknesses from the BHSP-3 and BHSP-4 gave scatter points where it was calculated via the mathematical model to have a result on each point, giving a reference on how the outputs of the model behave after increasing the thickness of the shell elements.

Table 3-19 - BH-2 Provisional Results of analysis of thicknesses

#	1	2	3	4	5	6	7	#	1	2	3	4	5	6	7
Orange	1.8	2.6	3.4	4.2	1.16	1.96	2.76	Green	1.8	2.6	3.4	4.2	1.16	1.96	2.76
Blue	2.6	4.2	1.8	3.4	4.52	2.12	3.72	Pourple	2.6	4.2	1.8	3.4	4.52	2.12	3.72
Internal Energy	3.38E+08	3.90E+08	3.57E+08	4.21E+08	3.67E+08	3.37E+08	3.87E+08	Internal Energy	3.5E+08	3.9E+08	3.7E+08	4.0E+08	3.7E+08	3.5E+08	3.8E+08
Kinetic Energy	3.26E+10	3.30E+10	3.27E+10	3.31E+10	3.29E+10	3.26E+10	3.30E+10	Kinetic Energy	3.3E+10	3.3E+10	3.3E+10	3.3E+10	3.3E+10	3.3E+10	3.3E+10
Contact energy	1.47E+07	1.57E+07	1.30E+07	1.61E+07	1.56E+07	1.45E+07	1.60E+07	Contact energy	1.4E+07	1.3E+07	1.6E+07	1.4E+07	1.3E+07	1.4E+07	1.3E+07
Mass	851.49231	862.70099	854.20856	865.41724	858.28625	849.79382	861.0025	Mass	851.7	860.8	856.1	865.2	855.5	850.8	859.9
Resultant Acceleration	0.3156748	0.8235576	0.4275574	0.245122	1.1954052	0.4015076	0.4775527	Resultant Acceleration	0.478	0.207	0.243	0.420	0.619	0.443	0.218
477716 - Acceleration	0.2620867	0.7876765	0.0047683	0.0019928	1.1573762	0.1520182	0.464097	477716 - Acceleration	0.00530	0.11961	0.00996	0.38120	0.00528	0.00515	0.09719
accelerometer2 Acceleration	0.0176985	0.0059006	0.1187966	0.0991568	0.0089216	0.0375086	0.0022186	accelerometer2 Acceleration	0.414	0.028	0.039	0.002	0.593	0.361	0.031
accelerometer2 Acceleration	-0.2620867	-0.7876765	-0.0047683	-0.0019928	-1.1573762	-0.1520182	-0.464097	accelerometer2 Acceleration	-0.0053	-0.1196	-0.0100	-0.3812	-0.0053	-0.0051	-0.0972
Total Force	7.90E+07	9.41E+07	8.36E+07	9.94E+07	8.73E+07	7.83E+07	9.30E+07	Total Force	8.3E+07	9.1E+07	9.1E+07	9.3E+07	8.6E+07	8.4E+07	9.0E+07

Geometry variables

Similarly to the variable of the thickness, two designs were paired for them to observe the behavior and consist of seven experiments with two runs and the fifth design was experimented on in a separate environment.

In the geometric variables there are five variations on the design as we can see below on the figure 3.36.
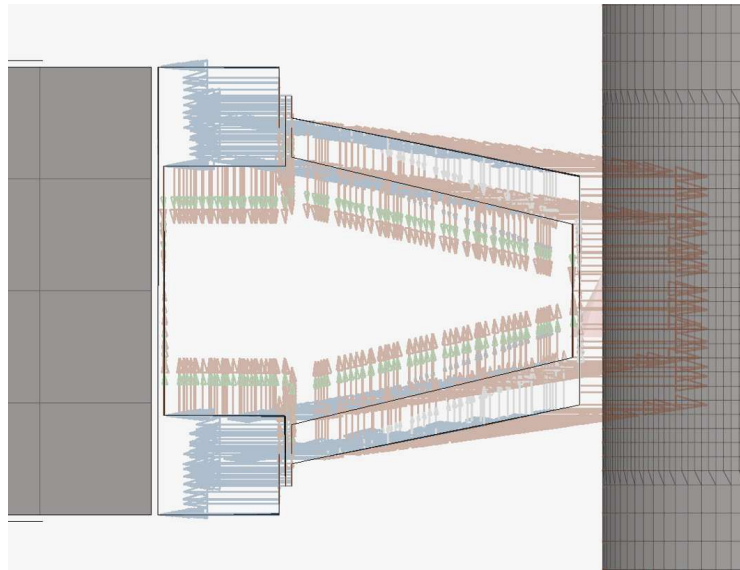

Figure 3.36 - Geometric variables proposed on 2nd design of side panel

In the first iteration, shapes 1 and 2 ranged between one and -1, with experiments designed using MELS based on proposed outputs. The results were analyzed using a fitting algorithm that alternates between regression types for viable outputs, employing the FAST parameter for optimal mathematical fit. Despite selecting LSR and MLSM as the best regressions, the R-value did not reach the target range of 0.65 to 1, complicating the optimization process.

Some outputs, however, were considered reliable. Parameters such as kinetic energy, internal energy, mass, X-momentum, central node acceleration, and total energy consistently achieved R-values above 0.65. While the acceleration at node 58623 was included as an additional output, its lower R-value did not significantly affect optimization decisions.

In the second iteration, shape 3 values ranged from 1 to 0, while shape 4 values ranged between -0.4 and 1. Using MELS, the outputs were again evaluated with the fitting algorithm.

Although LSR and MLSM were the preferred regressions, the R-values remained below the desired range, presenting further challenges in selecting optimization values.

The reliable parameters from the first iteration—kinetic energy, internal energy, mass, X-momentum, central node acceleration, and total energy—remained consistent. Acceleration at node 58623 continued to be an additional output, but its lower R-value did not hinder decision-making.

It is important to note that only shapes 1 and 2 changed, maintaining a static shell element thickness of 3 mm. This ensured consistency across iterations.

In the fifth iteration, sheet metal values ranged between one and -1, and MELS experiments were conducted accordingly. Unfortunately, the chosen regressions failed to meet the R-value criterion, making the results unsuitable for reliable predictions.

These challenges highlight the difficulties in achieving accurate regressions within the specified constraints. Improvements in modelling approaches or regression techniques may be necessary to optimize outputs and enhance prediction reliability.

Table 3-20 - BH-2 Provisional Results of analysis of thicknesses of Shape 5 and Shape 6

#	1	2	3	4	5	6	7
Shape three	0.2	0.4	0.6	0.8	0.04	0.24	0.44
Shape 4	-0.2	0.6	-0.6	0.2	0.76	-0.44	0.36
Internal energy	3.81E+08	3.75E+08	3.80E+08	3.79E+08	3.68E+08	3.79E+08	3.75E+08
Kinetic energy	3.29E+10	3.29E+10	3.29E+10	3.29E+10	3.29E+10	3.29E+10	3.29E+10
Contact energy	1.38E+07	1.52E+07	1.53E+07	1.42E+07	1.46E+07	1.32E+07	1.52E+07
Mass	858.4502	857.72961	858.46271	857.68597	857.91046	858.61023	857.85632
ACC-Resultant	0.5184357	0.5523592	0.3670097	0.1976293	0.4031779	0.4649512	0.5118744
Node 477716 AX-X	0.005041	0.0037417	0.0023743	0.0013294	0.0048365	0.0049751	0.0032756
2 Acceleration	0.4606845	0.5461051	0.3634924	0.1929363	0.2324719	0.3830934	0.5070047
Accelerometer	-0.005041	-0.0037417	-0.0023743	-0.0013294	-0.0048365	-0.0049751	-0.0032756
Total Force	8.95E+07	9.05E+07	8.64E+07	8.80E+07	8.73E+07	8.87E+07	8.87E+07

Table 3-21 - BH-2 Provisional Results of analysis of shapes

#	1	2	3	4	5	6	7	#	1	2	3	4	5	6	7
Shape one	-0.6	-0.2	0.2	0.6	-0.92	-0.52	-0.12	Shape three	-0.6	-0.2	0.2	0.6	-0.92	-0.52	-0.12
Shape 2	-0.2	0.6	-0.6	0.2	0.76	-0.44	0.36	Shape 4	-0.2	0.6	-0.6	0.2	0.76	-0.44	0.36
Internal energy	3.84E+08	3.80E+08	3.76E+08	3.69E+08	4.05E+08	3.83E+08	3.81E+08	Internal energy	3.75E+08	3.78E+08	3.60E+08	3.80E+08	3.83E+08	3.67E+08	3.79E+08
Kinetic energy	3.28E+10	3.28E+10	3.29E+10	3.30E+10	3.27E+10	3.28E+10	3.29E+10	Kinetic energy	3.29E+10	3.29E+10	3.29E+10	3.29E+10	3.29E+10	3.29E+10	3.29E+10
Contact energy	1.64E+07	1.24E+07	1.69E+07	1.28E+07	1.11E+07	1.55E+07	1.31E+07	Contact energy	1.63E+07	1.38E+07	1.02E+07	1.54E+07	1.63E+07	1.26E+07	1.37E+07
Mass	856.08063	857.57745	859.33838	860.88251	854.64417	856.44623	857.92773	Mass	858.83136	858.40186	858.51135	858.11121	858.76685	858.84906	858.42261
ACC-Resultant	0.5186546	0.6418501	0.3054782	0.2354846	1.5819578	0.1957259	0.4994216	ACC-Resultant	0.2272734	0.1905455	0.3043583	0.2843435	0.1100165	0.3321712	0.3168321
Node 477716 AX-X	0.2043232	0.0048082	0.066714	0.0543793	1.94E-04	3.32E-05	0.0046344	Node 477716 AX-X	0.1235073	0.0025393	0.2377802	0.262963	0.0014709	0.15722	0.0033809
2 Acceleration	0.0091199	0.5970501	0.0505218	0.0484863	1.5730174	0.0433491	0.4025118	2 Acceleration	0.0211978	0.0858016	0.0127607	0.0161744	0.0248183	0.02476	0.1922209
Accelerometer	-0.2043232	-0.0048082	-0.066714	-0.0543793	-1.94E-04	-3.32E-05	-0.0046344	Accelerometer	-0.1235073	-0.0025393	-0.2377802	-0.262963	-0.0014709	-0.15722	-0.0033809
Total Force	8.89E+07	9.02E+07	8.93E+07	8.06E+07	8.80E+07	8.89E+07	9.11E+07	Total Force	8.95E+07	9.15E+07	8.94E+07	9.08E+07	9.06E+07	8.97E+07	9.00E+07

3.10.3 BH-3

The process in which the third design of the external crash structure had the next procedure along with the variables, both geometric and from thicknesses, according to each one. The design of this external crash structure, figure 3.37, consists of sheet metal components with their desired thicknesses.
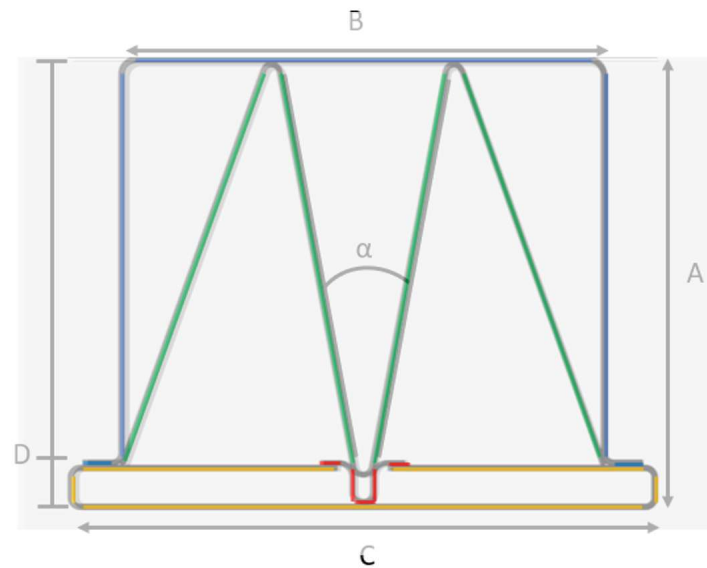

Figure 3.37 - BH-3 Battery housing side crash structure number 3

In this design the variables were split into thicknesses and shapes, according to each one and their pairing, it was selected the best option on the selection on each one. With this the algorithm was runner and found the best option of regression possible

The best regressions chosen were LSR and MLSM depending on the output, however the value R did not reach the expected value between .75 and one. This proposes a challenge just choosing the values that need to be optimized.

In table 3.22 the results of "R" are presented, giving us the regression outputs on all the variables further explained.

Table 3-22 - BH-2 Provisional Results of regression on outputs of value R

BH-2		Blue - Green	Red - Yellow	SHAPE-1	SHAPE-2/3	SHAPE-4/5	SHAPE-6/7
Internal Energy	RBF	0.92135	0.96435	-0.586518	0.901708	0.954483	0.893461
Kinetic Energy	LSR	0.99592	0.99932	0.996634	0.943085	-0.133565	0.988728
X-Momentum	MLSM	0.99042	0.99959	0.998209	0.940538	-0.149519	0.989700
Mass	LSR	1.00000	1.00000	0.999984	0.999712	0.998746	0.998750

Accelerometer 3	MLSM	0.95389	0.99897	0.840649	0.971660	0.902433	-0.361111
Resultant Acceleration	RBF	0.99866	0.98946	-0.777107	-0.043405	0.912312	-0.143342

Thicknesses

The variables in thickness were paired in external and internal, this constitutes the thicknesses that were explored in fourteen different experiments with two runs of seven each. The first pair explored was the thickness in the BHSP-1 and 2 and the second pair is in the BHSP-3 and 4.

In the first pair of the iteration the value of the sheet metal was between 1 and 5 mm, and the values chosen for the design of experiments using MELS with the results of the proposed outputs were as follows:

These results were imported to a fitting algorithm that alters between different types of regressions for a result to be viable with the parameter FAST for the best fit in the mathematical model.

After running the algorithm, the best regressions chosen were LSR and MLSM depending on the output, however the value R did not reach the expected value between .75 and one. This proposes a challenge just choosing the values that need to be optimized.

In these results the values of the mathematical model that will be taken almost 100% granted are the kinetic energy, the internal energy, the mass of the model, the momentum on X, the acceleration of the central node, and the total energy. Every single output in this has a value above .65, however the value given in the node 477716 in the acceleration will be considered as an additional output, but the decision will not carry any concern on the parameter.

It is crucial to indicate that the only values on the model that changes are the BHSP-1 and BHSP-2, creating the base thickness of the model on the rest of shell elements static at 3 mm. These results were imported to a fitting algorithm that alters between different types of regressions for a result to be viable with the parameter FAST for the best fit in the mathematical model.

After running the algorithm, the best regressions chosen were LSR and MLSM depending on the output, however the value R did not reach the expected value between .75 and one. This proposes a challenge just choosing the values that need to be optimized.

In these results the values of the mathematical model that will be taken almost 100% granted are total energy, kinetic energy, internal energy, acceleration on central node, momentum on x. Every single output in this has a value above .65.

Table 3-23 - BH-3 Provisional Results of analysis of thicknesses

#	1	2	3	4	5	6	7	#	1	2	3	4	5	6	7
Blue	1.8	2.6	3.4	4.2	1.16	1.96	2.76	Red	1.8	2.6	3.4	4.2	1.16	1.96	2.76
Green	2.6	4.2	1.8	3.4	4.52	2.12	3.72	Yellow	2.6	4.2	1.8	3.4	4.52	2.12	3.72
Internal energy	4.23E+08	5.31E+08	4.39E+08	5.58E+08	4.73E+08	4.03E+08	5.20E+08	Internal energy	4.48E+08	5.04E+08	4.66E+08	5.18E+08	4.64E+08	4.45E+08	4.94E+08
Kinetic energy	3.09E+10	3.14E+10	3.10E+10	3.15E+10	3.12E+10	3.09E+10	3.13E+10	Kinetic energy	3.10E+10	3.13E+10	3.11E+10	3.14E+10	3.11E+10	3.10E+10	3.13E+10
Momentum on X	-6791857.5	-6897548.5	-6813946.5	-6919240	-6860711	-6774977	-6881205	Momentum on X	-6804670.5	-6873433.5	-6838986	-6907422	-6834456	-6798141.5	-6866419.5
Mass	810.0976	824.99835	813.05127	827.95203	819.65527	807.70819	822.60895	Mass	812.29926	821.39545	816.65417	825.75037	816.09229	811.35101	820.4472
Central accelerometer	-8.5102129	-11.025245	-13.109803	-17.805754	-7.2403584	-9.0975475	-11.534315	Central accelerometer	-8.1220093	-12.334987	-12.297167	-14.865142	-5.7221413	-8.5854635	-12.491762
Accelerometer	77974.537	60535.483	110525.53	96670.11	48158.255	91575.238	70920.449	Accelerometer	84798.141	90965.963	88062.528	93044.114	85785.64	84369.317	90858.06

Geometry variables

Similarly to the variable of thickness, designs were paired for them to observe the behavior and consist of seven experiments with three runs and the seventh design was experimented on in a separate environment.

In the geometric variables there are six variations on the design as we can see below on figure 3.38.
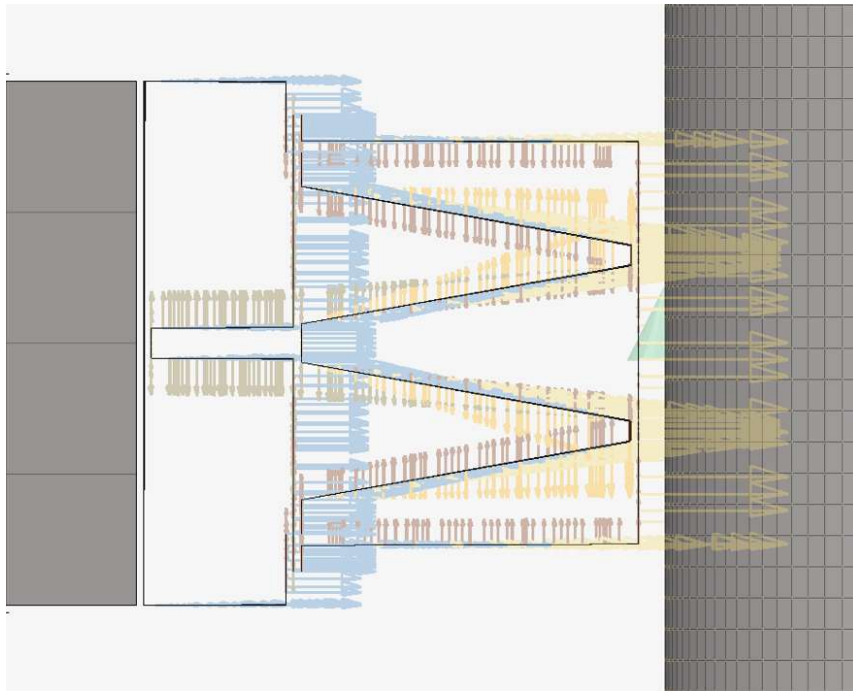
Figure 3.38 - Geometric variables of proposed 3rd design

The iterative optimization process aimed to evaluate the value of sheet metal within the range of -1 to 1, using design of experiments (DOE) with MELS. Despite thorough testing, the fitting algorithms—primarily LSR and MLSM—struggled to achieve the desired regression values (≥ 0.65) necessary for building a reliable predictive mathematical model. This posed significant challenges in optimizing the parameters and outputs.

In the first iteration, the selected variables and proposed outputs were analyzed. However, after importing the results into the fitting algorithm and testing various regression types, the best regressions failed to meet the criteria, with -values falling short of the required range. The parameters deemed viable for the model included kinetic energy, internal energy, total energy, mass, momentum on the X-axis, and acceleration at the central node. Notably, the

acceleration at node 477716 was also considered as an additional output, but its inclusion carried no significant influence on the decision-making process. The model's shapes 2 and 3 were the only variables altered in this iteration, while the base thickness of the shell elements remained static at 3 mm.

The second iteration followed a similar procedure. The sheet metal value again ranged between -1 and 1, and the DOE results were tested with MELS for proposed outputs. After running the fitting algorithm, LSR and MLSM regression methods produced outputs, but - values still failed to reach the desired range of 0.75 to 1. This iteration retained key outputs such as total energy, kinetic energy, internal energy, momentum on the X-axis, and acceleration at the central node, all of which exceeded -values of 0.65. Adjustments were made to shapes 3 and 4, maintaining the 3 mm base thickness of shell elements.

The third iteration involved testing the same range for sheet metal values with a new set of DOE parameters. Results were again imported into the fitting algorithm, which attempted to identify optimal regressions. While LSR and MLSM were employed, the outputs still did not meet the expected -value range of 0.75 to 1. Key metrics—total energy, kinetic energy, internal energy, acceleration at the central node, and momentum on the X-axis—remained the most reliable predictors with -values exceeding 0.65. In this iteration, modifications were limited to shapes 6 and 7, while the base thickness of 3 mm for shell elements was retained.

Across all iterations, the consistent challenge lay in achieving regression values within the optimal range. While key metrics provided a foundation for the model, the inability of certain outputs to meet criteria highlighted the difficulty of parameter optimization. The results underline the importance of refining regression approaches and exploring additional design variables to enhance model predictability. The fixed base thickness of 3 mm and the focus on specific shape variables reflect the systematic yet constrained approach used in this iterative design process.

Table 3-24 - BH-3 Provisional Results of analysis of shapes

#	1	2	3	4	5	6	7	#	1	2	3	4	5	6	7
Shape two	-0.6	-0.2	0.2	0.6	-0.92	-0.52	-0.12	Shape four	-0.6	-0.2	0.2	0.6	-0.92	-0.52	-0.12
Shape 3	-0.2	0.6	-0.6	0.2	0.76	-0.44	0.36	Shape 5	-0.2	0.6	-0.6	0.2	0.76	-0.44	0.36
Internal energy	4.92E+08	4.86E+08	4.84E+08	4.78E+08	4.86E+08	4.93E+08	4.85E+08	Internal energy	4.95E+08	4.76E+08	4.87E+08	4.80E+08	225301	6.29E+08	4.86E+08
Kinetic energy	3.12E+10	3.12E+10	3.12E+10	3.12E+10	3.12E+10	3.12E+10	3.12E+10	Kinetic energy	3.12E+10	3.12E+10	3.12E+10	3.12E+10	3.18E+10	3.12E+10	3.12E+10
Contact energy	-6859655.5	-6857680.5	-6855464	-6852682.5	-6863583.5	-6859419	-6857224.5	Contact energy	-6857379.5	-6857721	-6856008	-6854058.5	-6961975	-6858829	-6856983
Mass	819.6073	819.23444	818.85559	818.45483	819.94061	819.53809	819.14606	Mass	819.42584	819.18506	818.93585	818.6731	819.63739	819.40082	819.11249
ACC-Resultant	-12.057939	-15.52045	8.8963766	-13.498379	-17.010481	-10.628202	-14.512509	ACC-Resultant	-33.333122	-14.220862	-11.220742	7.0634665	7.5679984	-32.352737	-13.36393
Node 477716 AX-X	86324.51	95137.492	85232.175	82570.266	84770.19	88633.877	92649.141	Node 477716 AX-X	72416.481	86666.231	87000.086	94988.962	76083.455	70963.858	88239.105
2 Acceleration	-0.6	-0.2	0.2	0.6	-0.92	-0.52	-0.12	Shape four	-0.6	-0.2	0.2	0.6	-0.92	-0.52	-0.12
Accelerometer	-0.2	0.6	-0.6	0.2	0.76	-0.44	0.36	Shape 5	-0.2	0.6	-0.6	0.2	0.76	-0.44	0.36
Total Force	4.92E+08	4.86E+08	4.84E+08	4.78E+08	4.86E+08	4.93E+08	4.85E+08	Internal energy	4.95E+08	4.76E+08	4.87E+08	4.80E+08	225301	6.29E+08	4.86E+08

Table 3-25 - BH-3 Provisional Results of analysis of shapes

#	1	2	3	4	5	6	7
Shape six	-0.6	-0.2	0.2	0.6	-0.92	-0.52	-0.12
Shape 7	-0.2	0.6	-0.6	0.2	0.76	-0.44	0.36
Internal energy	5.04E+08	4.35E+08	6.76E+08	4.57E+08	4.36E+08	5.64E+08	4.48E+08
Kinetic energy	3.13E+10	3.12E+10	3.13E+10	3.12E+10	3.12E+10	3.13E+10	3.12E+10
Contact energy	-6866023.5	-6844504	-6873174	-6848116	-6848623	-6873608	-6849043
Mass	820.92023	816.78119	822.47296	817.41425	817.41992	822.23834	817.55609
ACC-Resultant	-11.25936	-7.0999961	-7.0449681	-8.2475471	-7.0787659	-7.2915988	-7.0393643
Node 477716 AX-X	203688.5	129413.56	36306.565	25624.946	2615720.4	115917.57	129098.52
Shape six	-0.6	-0.2	0.2	0.6	-0.92	-0.52	-0.12

#	1	2	3	4
Shape one	0	-0.5	0.5	-0.75
Internal energy	4.86E+08	4.85E+08	4.79E+08	4.87E+08
Kinetic energy	3.12E+10	3.13E+10	3.11E+10	3.14E+10
Momentum on X	-6856044	-6880674.5	-6833689	-6891659
Mass	819.02484	821.7135	816.35358	823.06189
Central accelerometer	-12.496834	-10.013577	-17.11908	-9.196691
Accelerometer	90063.694	82999.535	81397.287	71081.844

3.10.4 External sheet

The process in which the first design of the external sheet had the next procedure along with the variables, both geometric and from thickness, according to each one. The design of this external crash structure, figure 3.39, consists of sheet metal components with their desired thickness.
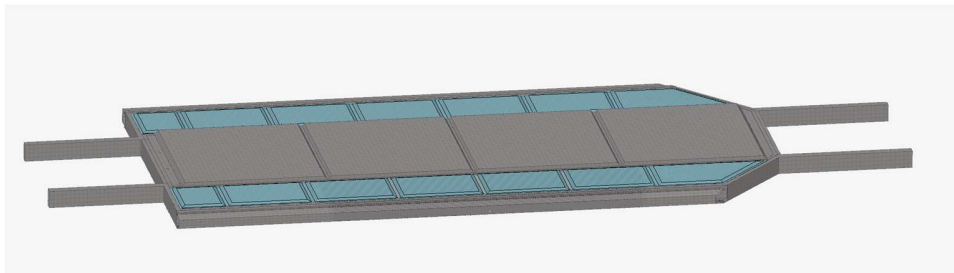
Figure 3.39 - EX-SH Design of the sheet metal external design.

In this design the variables were split into thicknesses and shapes, according to each one and their pairing, it was selected the best option on the selection on each one. With this the algorithm was runner and found the best option of regression possible

The best regressions chosen were LSR and MLSM depending on the output, however the value R did not reach the expected value between .75 and one. This proposes a challenge just choosing the values that need to be optimized.

In table 3.26 the results of "R" are presented, giving us the regression outputs on all the variables further explained.

Table 3-26 - BH-2 Provisional Results of regression on outputs of value R

BH-EXT-SH		EXT-SH	SHAPE 1/2
Internal Energy - MAG	RBF	0.9997901	0.3484053
Kinetic Energy - MAG	MLSM	0.9999967	0.9568411
Mass - MAG	MLSM	1.0000000	0.9383089
Contact energy - MAG	RBF	0.9117555	0.9343266
TE-Total Energy - MAG	LSR	0.9999985	0.9302562

Accelerometer - AX-X Acceleration	RBF	0.9742007	0.7684083

Thickness

The variables in thickness were paired in external and internal, this constitutes the thicknesses that were explored in one experiment with one run.

Table 3-27 - EX-SH Provisional Results of analysis of thicknesses

#	1	2	3	4	5	6	7
EXT-SH	1.8	2.6	3.4	4.2	1.16	1.96	2.76
Internal energy	8.56E+08	9.29E+08	9.56E+08	1.03E+09	8.32E+08	8.61E+08	9.37E+08
Kinetic energy	3.16E+10	3.22E+10	3.26E+10	3.32E+10	3.12E+10	3.17E+10	3.22E+10
Mass	837.87012	854.40723	866.38373	882.92078	828.28894	840.26544	856.80249
Contact energy	3.30E+07	3.70E+07	3.75E+07	4.54E+07	3.14E+07	3.28E+07	3.83E+07
Total energy	9.74E+11	9.93E+11	1.01E+12	1.03E+12	9.63E+11	9.77E+11	9.96E+11
Accelerometer - AX-X Acceleration	-1879.3063	-3558.0693	-4423.2378	-5320.5835	-1736.4183	-2048.7712	-3740.0862
accelerometer - ACC-Resultant Acceleration	1887.2841	3595.4392	4440.0444	5350.6392	1739.0082	2054.4468	3773.522

These results were imported to a fitting algorithm that alters between different types of regressions for a result to be viable with the parameter FAST for the best fit in the mathematical model.

After running the algorithm, the best regressions chosen were LSR and MLSM depending on the output, however the value R did not reach the expected value between .75 and one. This proposes a challenge just choosing the values that need to be optimized.

In these results the values of the mathematical model that will be taken almost 100% granted are the kinetic energy, the internal energy, the mass of the model, the momentum on X, the acceleration of the central node, and the total energy. Every single output in this has a value above .65.

It is crucial to indicate that the only value on the model that changes is the EXT-SH, creating the base thickness of the model on the rest of shell elements static at 3 mm.

Geometry variables

Similarly to the variable of the thickness, two designs were paired for them to observe the behavior and consist of seven experiments with two runs and the fifth design was experimented on in a separate environment.

In the geometric variables there are five variations on the design as we can see below on the figures 3.40 and 3.41.
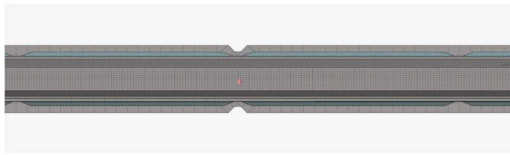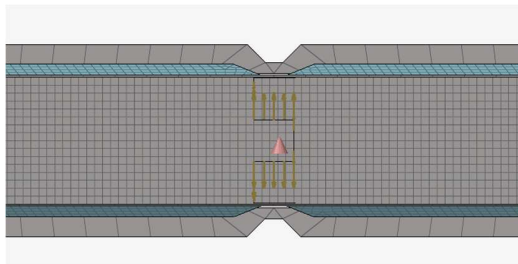

Figure 3.40 - EX-SH Geometric variable "shape 1"
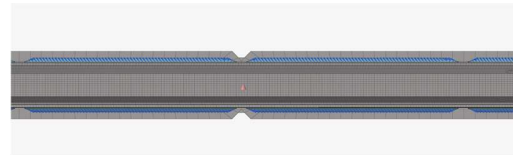
Figure 3.41 - EX-SH Geometric variable "shape 2"

In the first pair of the iteration the value of the shapes 1 and 2 were between one and -1, and the values chosen for the design of experiments using MELS with the results of the proposed outputs were as follows:

Table 3-28 - EX-SH Provisional Results of analysis of the variation on shape one and shape two

#	1	2	3	4	5	6	7
Shape 1	-0.6	-0.2	0.2	0.6	-0.92	-0.52	-0.12
Shape 2	-0.2	0.6	-0.6	0.2	0.76	-0.44	0.36
Internal energy	9.38E+08	9.30E+08	9.33E+08	9.40E+08	9.38E+08	9.24E+08	9.27E+08
Kinetic energy	3.25E+10	3.24E+10	3.23E+10	3.23E+10	3.25E+10	3.24E+10	3.24E+10
Mass	862.03589	859.91846	858.91742	858.59613	862.03589	860.0791	859.5824
Contact energy	3.79E+07	3.75E+07	3.61E+07	3.74E+07	3.79E+07	3.63E+07	3.75E+07
Total energy	1.00E+12	1.00E+12	9.98E+11	9.98E+11	1.00E+12	1.00E+12	9.99E+11
Accelerometer - AX-X Acceleration	-2494.3074	-2818.386	-4841.9238	-5544.2539	-2494.3074	-3232.658	-3206.3394
accelerometer - ACC-Resultant Acceleration	2510.0896	2820.7625	4872.2622	5571.5859	2510.0896	3255.967	3215.8843

These results were imported to a fitting algorithm that alters between different types of regressions for a result to be viable with the parameter FAST for the best fit in the mathematical model.

After running the algorithm, the best regressions chosen were LSR and MLSM depending on the output, however the value R did not reach the expected value between .65 and one. This proposes a challenge just choosing the values that need to be optimized.

In these results the values of the mathematical model that will be taken almost 100% granted are kinetic energy, internal energy, the mass of the model, the momentum on X, the acceleration of the central node, and the total energy. Every single output in this has a value above .65.

It is crucial to indicate that the only values on the model that changes are the shape one and chape two, creating the base thickness of the model of shell elements static at 3 mm.

3.10.5 Pillar - 1

The process in which the second design of the pillar structure had the next procedure along with the variables, both geometric and from thicknesses, according to each one. The design of this pillar, figure 3.42, consists of sheet metal components with their desired thickness.
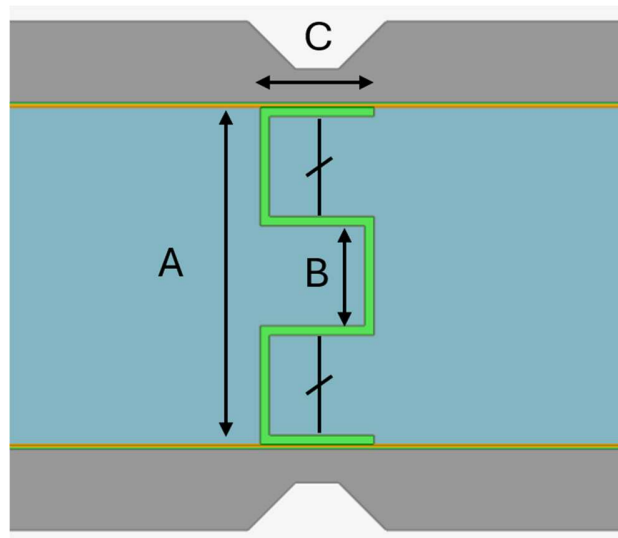
Figure 3.42 - P-1 Pillar geometry on the design number 1

In this design the variables were split into thicknesses and shapes, according to each one and their pairing, it was selected the best option on the selection on each one. With this the algorithm was runner and found the best option of regression possible

The best regressions chosen were LSR and MLSM depending on the output, however the value R did not reach the expected value between .75 and one. This proposes a challenge just choosing the values that need to be optimized.

In table 3.29 the results of "R" are presented, giving us the regression outputs on all the variables further explained.

Table 3-29 – PILLAR Provisional Results of regression on outputs of value R

BH-P-1		PILLAR	SHAPE 1/2
TE-Total Energy - MAG	LSR	0.9999985	0.9993743
Internal Energy - MAG	RBF	0.9997901	0.5284544
Kinetic Energy - MAG	MLSM	0.9999967	0.9810710
Mass - MAG	MLSM	1.0000000	1.0000000
Contact energy - MAG	RBF	0.9117555	0.2527607
Two accelerometer2 - AX-X Acceleration	RBF	0.9742007	0.4331803
Two accelerometer2 - ACC-Resultant Acceleration	RBF	0.9732692	0.2576966

Thickness

The variables in thickness were paired in external and internal, this constitutes the thicknesses that were explored in one experiment with one run.

Table 3-30 - P-1 Provisional Results of analysis of thicknesses

#	1	2	3	4	5	6	7
Pillar	2.6	4.2	1.8	3.4	4.52	2.12	3.72
Internal Energy - MAG	8.56E+08	9.29E+08	9.56E+08	1.03E+09	8.32E+08	8.61E+08	9.37E+08
Kinetic Energy - MAG	3.16E+10	3.22E+10	3.26E+10	3.32E+10	3.12E+10	3.17E+10	3.22E+10
Mass - MAG	837.87012	854.40723	866.38373	882.92078	828.28894	840.26544	856.80249
Contact energy - MAG	3.30E+07	3.70E+07	3.75E+07	4.54E+07	3.14E+07	3.28E+07	3.83E+07
TE-Total Energy - MAG	9.74E+11	9.93E+11	1.01E+12	1.03E+12	9.63E+11	9.77E+11	9.96E+11
AX-X Acceleration	-1879.3063	-3558.0693	-4423.2378	-5320.5835	-1736.4183	-2048.7712	-3740.0862
ACC-Resultant Acceleration	1887.2841	3595.4392	4440.0444	5350.6392	1739.0082	2054.4468	3773.522

These results were imported to a fitting algorithm that alters between different types of regressions for a result to be viable with the parameter FAST for the best fit in the mathematical model.

After running the algorithm, the best regressions chosen were LSR and MLSM depending on the output, however the value R did not reach the expected value between .75 and one. This proposes a challenge just choosing the values that need to be optimized.

In these results the values of the mathematical model that will be taken almost 100% granted are kinetic energy, internal energy, the mass of the model, the momentum on X, the acceleration of the central node, and the total energy. Every single output in this has a value above .65.

It is crucial to indicate that the only value on the model that changes is the EXT-SH, creating the base thickness of the model on the rest of the shell elements static at 3 mm.

Geometry variables

Similarly to the variable of the thickness, two designs were paired for them to observe the behavior and consist of seven experiments with two runs, in the geometric variables there are five variations on the design as we can see below on the figures 3.43 and 3.44.
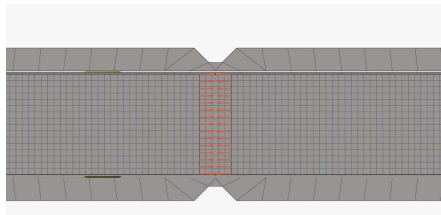

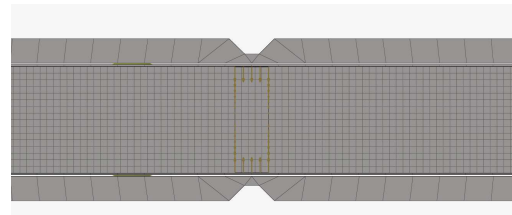Figure 3.43 - P-1 Geometric variable "shape 1"
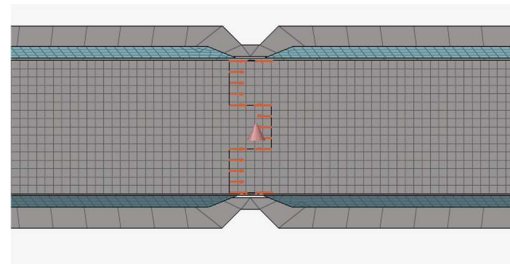
Figure 3.44 - P-1 Geometric variable "shape 2"

In the first pair of the iteration the value of the shapes 1 and 2 were between one and -1, and the values chosen for the design of experiments using MELS with the results of the proposed outputs were as follows:

Table 3-31 - P-1 Provisional Results of analysis of the variation on shape one and shape two

#	1	2	3	4	5	6	7
Shape 1	-0.6	-0.2	0.2	0.6	-0.92	-0.52	-0.12
Shape 2	-0.2	0.6	-0.6	0.2	0.76	-0.44	0.36
Internal Energy - MAG	9.34E+08	9.36E+08	9.31E+08	9.32E+08	9.36E+08	9.32E+08	9.33E+08
Kinetic Energy - MAG	3.24E+10	3.24E+10	3.23E+10	3.24E+10	3.24E+10	3.24E+10	3.23E+10
Mass - MAG	859.77161	859.42743	859.08325	859.70276	860.04694	859.70276	859.35858
Contact energy - MAG	3.84E+07	3.74E+07	3.73E+07	3.80E+07	3.81E+07	3.80E+07	3.71E+07
TE-Total Energy - MAG	9.99E+11	9.99E+11	9.99E+11	9.99E+11	1.00E+12	9.99E+11	9.99E+11
AX-X Acceleration	-3662.9868	-3798.7781	-3859.8513	-3766.2397	-3688.4631	-3766.2397	-3896.0088
ACC-Resultant Acceleration	3687.6162	3827.8367	3873.2922	3787.6802	3733.3772	3787.6802	3919.9812

These results were imported to a fitting algorithm that alters between different types of regressions for a result to be viable with the parameter FAST for the best fit in the mathematical model.

After running the algorithm, the best regressions chosen were LSR and MLSM depending on the output, however the value R did not reach the expected value between .65 and one. This proposes a challenge just choosing the values that need to be optimized.

In these results the values of the mathematical model that will be taken almost 100% granted are kinetic energy, internal energy, the mass of the model, the momentum on X, the acceleration of the central node, and the total energy. Every single output in this has a value above .65.

It is crucial to indicate that the only values on the model that changes are the shape one and chape two, creating the base thickness of the model of shell elements static at 3 mm.

3.10.6 Pillar - 2

The process in which the second design of the pillar structure had the next procedure along with the variables, both geometric and from thicknesses, according to each one. The design of this pillar, figure 3.44, consists of sheet metal components with their desired thickness.
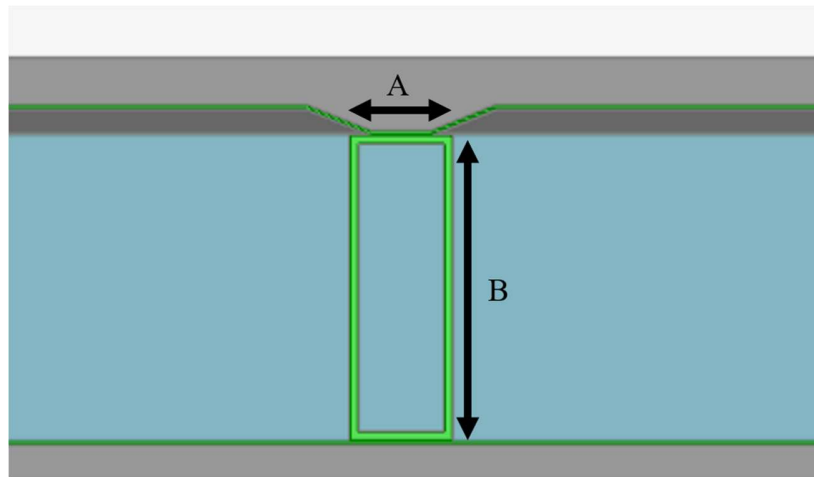
Figure 3.45 - P-2 Pillar geometry on the design number 2

In this design the variables were split into thicknesses and shapes, according to each one and their pairing, it was selected the best option on the selection on each one. With this the algorithm was runner and found the best option of regression possible

The best regressions chosen were LSR and MLSM depending on the output, however the value R did not reach the expected value between .75 and one. This proposes a challenge just choosing the values that need to be optimized.

In table 3.22 the results of "R" are presented, giving us the regression outputs on all the variables further explained.

Table 3-32 – PILLAR Provisional Results of regression on outputs of value R

BH-P-1		PILLAR	SHAPE 1/2
Internal Energy - MAG	MLSM	0.9893767	0.7610363
Kinetic Energy - MAG	MLSM	0.9999178	0.1070112
Mass - MAG	MLSM	1	1.0000000
Contact energy - MAG	MLSM	0.8370406	-0.4400000
TE-Total Energy - MAG	MLSM	0.9999985	0.9627464
Two accelerometer2 - AX-X Acceleration	MLSM	0.9274095	0.8617949

Two accelerometer2 - ACC-Resultant Acceleration	MLSM	0.9378168	0.8188015
One group1 - total resultant force	MLSM	0.9766135	-0.4229062
Internal Energy - MAG	MLSM	0.9893767	0.7610363

Thickness

The variables in thickness were paired in external and internal, this constitutes the thicknesses that were explored in one experiment with one run.

Table 3-33 - P-2 Provisional Results of analysis of thicknesses

#	1	2	3	4	5	6	7
Pillar	1.8	2.6	3.4	4.2	1.16	1.96	2.76
Internal energy	9.22E+08	1.03E+09	8.76E+08	9.97E+08	1.03E+09	8.86E+08	1.00E+09
Kinetic energy	3.21E+10	3.31E+10	3.16E+10	3.27E+10	3.33E+10	3.18E+10	3.28E+10
Mass	851.54761	881.59033	839.13635	869.17908	885.5108	843.05676	873.09955
Contact energy	3.56E+07	4.26E+07	3.25E+07	3.97E+07	4.02E+07	3.18E+07	3.86E+07
Total energy	9.90E+11	1.02E+12	9.75E+11	1.01E+12	1.03E+12	9.80E+11	1.01E+12
Accelerometer on AX-X	-4654.917	-6084.5786	-3933.2773	-5951.0527	-6584.3213	-4083.9922	-6152.7881
Resultant acceleration on accelerometer	4689.771	6193.8169	3938.999	6032.1025	6666.4336	4109.9497	6241.5073
Total resultant force	2.01E+08	2.21E+08	1.93E+08	2.13E+08	2.20E+08	1.96E+08	2.13E+08

These results were imported to a fitting algorithm that alters between different types of regressions for a result to be viable with the parameter FAST for the best fit in the mathematical model.

After running the algorithm, the best regressions chosen were LSR and MLSM depending on the output, however the value R did not reach the expected value between .75 and one. This proposes a challenge just choosing the values that need to be optimized.

In these results the values of the mathematical model that will be taken almost 100% granted are kinetic energy, internal energy, the mass of the model, the momentum on X, the acceleration of the central node, and the total energy. Every single output in this has a value above .65.

It is crucial to indicate that the only value on the model that changes is the EXT-SH, creating the base thickness of the model on the rest of the shell elements static at 3 mm.

Geometry variables

Similarly to the variable of the thickness, two designs were paired for them to observe the behavior and consist of seven experiments with two runs, in the geometric variables there are five variations on the design as we can see below on the figures 3.46 and 3.47.
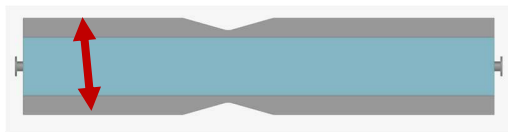

Figure 3.46 - P-2 Geometric variable "shape 1"
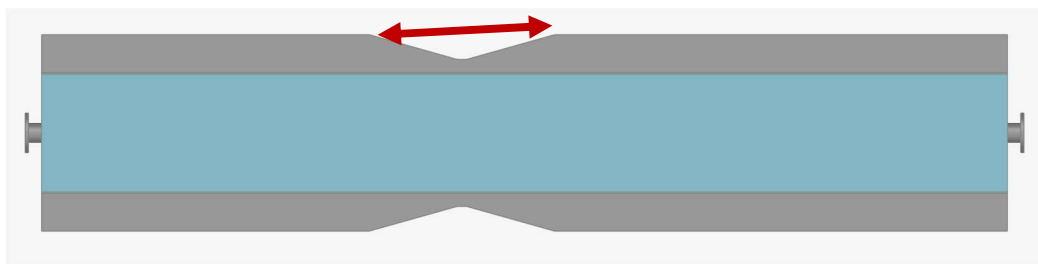

Figure 3.47 - P-2 Geometric variable "shape 2"

In the first pair of the iteration the value of the shapes 1 and 2 were between one and -1, and the values chosen for the design of experiments using MELS with the results of the proposed outputs were as follows:

Table 3-34 - P-2 Provisional Results of analysis of the variation on shape one and shape two

#	1	2	3	4	5	6	7
Shape 1	-0.6	-0.2	0.2	0.6	-0.92	-0.52	-0.12
Shape 2	-0.2	0.6	-0.6	0.2	0.76	-0.44	0.36
Internal energy	9.49E+08	9.39E+08	9.56E+08	9.42E+08	9.43E+08	9.57E+08	9.42E+08
Kinetic energy	3.23E+10	3.23E+10	3.23E+10	3.23E+10	3.23E+10	3.23E+10	3.23E+10
Mass	859.51721	858.8288	859.28772	858.92059	859.15009	859.60901	858.92059
Contact energy	2.54E+08	3.56E+07	3.87E+07	3.55E+07	3.58E+07	3.97E+07	3.55E+07
Total energy	9.99E+11	9.98E+11	9.99E+11	9.98E+11	9.99E+11	9.99E+11	9.98E+11
Accelerometer on AX-X	-6429.2026	-8280.4668	-5786.7876	-8251.8066	-8251.0811	-5095.6357	-8251.8066
Resultant acceleration on accelerometer	6601.3462	8287.8975	5828.0298	8270.9189	8256.4336	5138.0737	8270.9189
Total resultant force	2.04E+08	2.05E+08	2.07E+08	2.05E+08	2.05E+08	2.08E+08	2.05E+08

These results were imported to a fitting algorithm that alters between different types of regressions for a result to be viable with the parameter FAST for the best fit in the mathematical model.

After running the algorithm, the best regressions chosen were LSR and MLSM depending on the output, however the value R did not reach the expected value between .65 and one. This proposes a challenge just choosing the values that need to be optimized.

In these results the values of the mathematical model that will be taken almost 100% granted are the kinetic energy, the internal energy, the mass of the model, the momentum on X, the acceleration of the central node, and the total energy. Every single output in this has a value above .65.

It is crucial to indicate that the only values on the model that changes are the shape one and chape two, creating the base thickness of the model of shell elements static at 3 mm.

3.10.7 Thermal analysis

The process in which thermal analysis had the next procedure along with the variables, both geometric and from thicknesses, according to each one. The design of the upper and lower cover for thermal isolation, figure 3.48 consists of sheet metal components with their desired thicknesses.
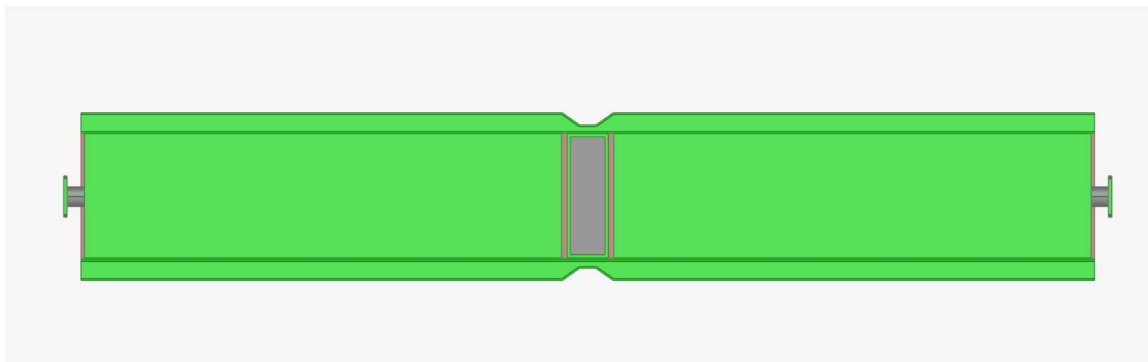
Figure 3.48 - TH-A Cross section of thermal model for thermal isolation and thermal absorption

Thickness

The variables in thickness were paired in external and internal, this constitutes the thicknesses that were explored in one experiment with one run.

Table 3-35 - TH-A Provisional Results of analysis of thicknesses

THK	C°	MASS	UP-MAX	UP-AVG	SUN-MAX	SUN-AVG	BOT-MAX	BOT-AVG
1.50	10	189.85	28.67	19.27	26.68	21.45	21.53	16.79
1.50	25	189.85	43.67	34.27	41.68	36.45	36.53	31.79
1.50	45	189.85	63.67	54.27	61.68	56.45	56.53	51.79
1.25	10	189.85	28.68	19.26	26.70	21.48	21.52	19.26
1.25	25	189.85	43.68	34.26	41.70	36.48	36.52	34.26
1.25	45	189.85	63.68	54.26	61.70	56.48	56.52	54.26
2.00	10	188.41	29.63	19.29	26.93	21.51	21.61	16.76
2.00	25	188.41	44.63	34.29	41.93	36.51	36.60	31.76
2.00	45	188.41	64.63	54.29	61.93	56.50	56.60	51.76
1.20	10	188.41	29.63	19.29	26.93	21.51	21.61	16.76
1.20	25	188.41	44.63	34.29	41.93	36.51	36.60	31.76
1.20	45	188.41	64.63	54.29	61.93	56.50	56.60	51.76
3.50	10	191.24	29.23	18.10	29.22	22.68	18.09	15.10
3.50	25	191.24	44.23	33.10	44.22	37.67	33.09	30.10
3.50	45	191.24	64.23	53.10	64.22	57.68	53.09	50.10

These results were imported to a fitting algorithm that alters between different types of regressions for a result to be viable with the parameter FAST for the best fit in the mathematical model.

After running the algorithm, the best regressions chosen were LSR and MLSM depending on the output, however the value "R" did not reach the expected value between .75 and one. This proposes a challenge just choosing the values that need to be optimized.

Table 3-36 - TH-A Provisional Results of regression on outputs of value R

Heat Transfer: Mass	MLSM	0.1070112
Heat Transfer: UP-MAX	LSR	0.1070112
Heat Transfer: UP-AVG	RBF	0.9062877
Heat Transfer: SUN-AVG	RBF	0.8871675
Heat Transfer: SUN-MAX	MLSM	0.9993501
Heat Transfer: BOTTOM-MAX	RBF	0.9157113
Heat Transfer: BOTTOM-AVG	MLSM	0.0400476

In these results the values of the mathematical model that will be taken almost 100% granted are kinetic energy, internal energy, the mass of the model, the momentum on X, the acceleration of the central node, and the total energy. Every single output in this has a value above .65.

It is crucial to indicate that the only value on the model changes, creating the base thickness of the model on the rest of the shell elements static at 3 mm.

Geometry variables

Similarly to the variable of the thickness, two designs were paired for them to observe the behavior and consist of seven experiments with two runs and the fifth design was experimented on in a separate environment.

In the geometric variables there are five variations in the design as we can see below on the figures 3.49, 3.50 and 3.51.

Figure 3.49 - TH-A Geometric variable "L1"
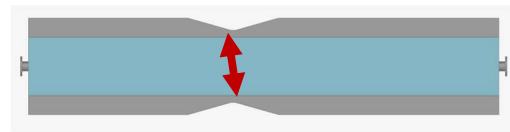
Figure 3.50 - TH-A Geometric variable "L2"

Figure 3.51 - TH-A Geometric variable "P1"

Table 3-37 - TH-A Provisional Results of regression on outputs of value R

Heat Transfer: Mass	MLSM	0.9999979
Heat Transfer: UP-MAX	LSR	-0.5965831
Heat Transfer: UP-AVG	RBF	-0.6427431
Heat Transfer: SUN-AVG	RBF	-0.6525432
Heat Transfer: SUN-MAX	MLSM	-0.7331735
Heat Transfer: BOTTOM-MAX	RBF	-0.7777778
Heat Transfer: BOTTOM-AVG	MLSM	0.0833309

In the first iteration the value of the shape L1 was between 30 and 15, and the values chosen for the design of experiments using MELS with the results of the proposed outputs were as follows:

Table 3-38 - TH-A Provisional Results of analysis of the variation on shape L1

L1	C°	MASS	UP-MAX	UP-AVG	SUN-MAX	SUN-AVG	BOT-MAX	BOT-AVG
30.00	10	202.07	31.53	19.51	27.05	21.20	21.71	16.48
30.00	25	202.07	46.53	34.51	42.05	36.20	36.71	31.48
30.00	45	202.07	66.53	54.51	62.05	56.20	56.71	51.48
25.00	10	196.70	31.44	19.48	26.77	21.12	21.58	16.60
25.00	25	196.70	46.44	34.48	41.77	36.12	36.58	31.60
25.00	45	196.70	66.44	54.48	61.77	56.12	56.58	51.60
20.00	10	191.31	31.65	19.46	26.66	20.89	21.39	16.74
20.00	25	191.31	46.65	34.45	41.66	35.89	36.39	31.74
20.00	45	191.31	66.65	54.45	61.66	55.89	56.39	51.74
15.00	10	185.93	45.75	21.70	37.16	23.74	22.63	17.72
15.00	25	185.93	64.75	36.70	52.16	38.74	37.63	32.72
15.00	45	185.93	84.75	56.70	72.16	58.74	57.63	52.72

These results were imported to a fitting algorithm that alters between different types of regressions for a result to be viable with the parameter FAST for the best fit in the mathematical model.

After running the algorithm, the best regressions chosen were LSR and MLSM depending on the output, however the value R did not reach the expected value between .65 and one. This proposes a challenge just choosing the values that need to be optimized.

Table 3-39 - TH-A Provisional Results of regression on outputs of value R

Heat Transfer: Mass	MLSM	0.9999979	0.9390122	0.9929494
Heat Transfer: UP-MAX	LSR	-0.5965831	0.7621622	-0.5574684
Heat Transfer: UP-AVG	RBF	-0.6427431	-0.7777778	-0.5625000
Heat Transfer: SUN-AVG	RBF	-0.6525432	-0.7777778	-0.1102235
Heat Transfer: SUN-MAX	MLSM	-0.7331735	-0.7777778	0.8883439
Heat Transfer: BOTTOM-MAX	RBF	-0.7777778	-0.7777778	-0.5625000
Heat Transfer: BOTTOM-AVG	MLSM	0.0833309	-0.7777778	-0.4948537

In these results the values of the mathematical model that will be taken almost 100% granted are the kinetic energy, the internal energy, the mass of the model, the momentum on X, the

acceleration of the central node, and the total energy. Every single output in this has a value above .65. It is crucial to indicate that in this variable it is not possible to indicate a correlation between the values of L1. In the second iteration the value of the shapes L2 were between 3.5 and 17.5, and the values chosen for the design of experiments using MELS with the results of the proposed outputs were as follows:

Table 3-40 - TH-A Provisional Results of analysis of the variation on shape L2

L2	C°	MASS	UP-MAX	UP-AVG	SUN-MAX	SUN-AVG	BOT-MAX	BOT-AVG
3.50	10	191.24	23.82	19.37	23.82	21.79	21.38	16.89
3.50	25	191.24	38.82	34.37	38.82	36.79	36.38	31.89
3.50	45	191.24	58.82	54.37	28.82	56.79	56.38	51.89
7.50	10	191.35	29.23	18.10	29.22	22.68	18.09	15.10
7.50	25	191.35	44.23	33.10	44.22	37.67	33.09	30.10
7.50	45	191.35	64.23	53.10	64.22	57.68	53.09	50.10
12.50	10	191.54	36.62	13.02	36.61	29.22	13.08	10.14
12.50	25	191.54	51.62	28.02	51.61	44.22	28.08	25.14
12.50	45	191.54	71.62	48.02	71.61	64.22	48.08	45.14
17.50	10	191.64	38.79	20.96	27.67	21.98	28.32	17.80
17.50	25	191.64	53.79	35.96	42.67	36.98	43.32	32.80
17.50	45	191.64	73.79	55.96	62.67	56.98	63.32	52.80

These results were imported to a fitting algorithm that alters between different types of regressions for a result to be viable with the parameter FAST for the best fit in the mathematical model.

After running the algorithm, the best regressions chosen were LSR and MLSM depending on the output, however the value R did not reach the expected value between .65 and one. This proposes a challenge just choosing the values that need to be optimized.

In these results the values of the mathematical model that will be taken almost 100% granted are the kinetic energy, the internal energy, the mass of the model, the momentum on X, the acceleration of the central node, and the total energy. Every single output in this has a value above .65.

In the third iteration the value of the shape P1 were between 7.5 and 25, and the values chosen for the design of experiments using MELS with the results of the proposed outputs were as follows:

Table 3-41 - TH-A Provisional Results of analysis of the variation on shape P1

P1	C°	MASS	UP-MAX	UP-AVG	SUN-MAX	SUN-AVG	BOT-MAX	BOT-AVG
7.50	10	191.35	38.79	20.96	27.67	21.98	28.32	17.8
7.50	25	191.35	53.79	35.96	42.67	36.98	43.32	32.8
7.50	45	191.35	73.79	55.96	62.67	63.98	63.32	52.8
12.00	10	191.30	23.8	19.33	23.79	21.74	21.35	16.91
12.00	25	191.30	38.80	34.33	38.79	36.74	36.35	31.91
12.00	45	191.30	58.80	54.30	58.79	56.74	56.35	51.91
15.00	10	191.20	23.80	19.33	23.79	21.73	21.35	16.94
15.00	25	191.20	38.80	34.33	38.79	36.73	36.35	31.94
15.00	45	191.20	58.80	54.33	58.79	56.73	56.35	51.94
25.00	10	190.80	23.79	19.33	23.79	21.71	21.35	16.95
25.00	25	190.80	38.79	34.33	38.79	36.71	36.35	31.95
25.00	45	190.80	58.79	54.33	58.79	56.71	56.35	51.95

These results were imported to a fitting algorithm that alters between different types of regressions for a result to be viable with the parameter FAST for the best fit in the mathematical model.

After running the algorithm, the best regressions chosen were LSR and MLSM depending on the output, however the value R did not reach the expected value between .65 and one. This proposes a challenge just choosing the values that need to be optimized.

In these results the values of the mathematical model that will be taken almost 100% for granted are kinetic energy, internal energy, the mass of the model, the momentum on X, the acceleration of the central node, and the total energy. Every single output in this has a value above .65.

Both variables were plotted on the same goal, to minimize weight, maximize the internal energy approved on the model, reduce the kinetic energy on the model and reduce the acceleration on the central node. With these experiments the optimization method applied were the GRSM (Global Response Search Method)

3.11 MDAO

The post-processing phase of a Multidisciplinary Design Analysis and Optimization (MDAO) focused on crash and thermal analysis involves the detailed evaluation and interpretation of simulation results to optimize the design of a system or component. This stage is critical for assessing how different design variables—such as material properties, geometry, and structural configurations—impact the performance of a product under crash and thermal loading conditions. Using advanced post-processing techniques, the results from various simulations, including energy absorption, deformation behavior, heat distribution, and thermal cycling, are analyzed to identify potential areas for improvement. By visualizing key parameters like stress, strain, temperature gradients, and acceleration, engineers can make informed decisions about design modifications, material selection, and overall system robustness. The goal of post-processing in this context is to ensure that the final design not only meets safety and performance standards but also balances the trade-offs between crashworthiness, thermal management, and overall efficiency.

3.11.1 BH-1

The process in which the first design of the external crash structure had the next procedure along with the variables, both geometric and from thicknesses, according to each one. The design of this external crash structure

Thicknesses

The variables in thickness were paired in external and internal, this constitutes the thicknesses that were explored in fourteen different experiments with two runs of seven each. The first pair explored was the thickness in the BHSP-1 and 2 and the second pair is in the BHSP-3 and 4.

It is crucial to indicate that the only values on the model that changes are the BHSP-1 and BHSP-2, creating the base thickness of the model on the rest of shell elements static at 3 mm. The resulting graphics of BHSP1 are:
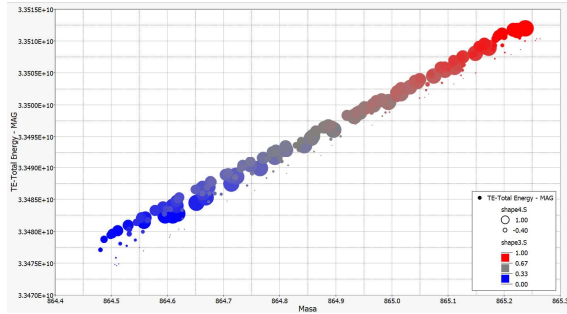
Figure 3.52 - Graphic of scatter points with X axis as the weight and Y axis as the internal energy.
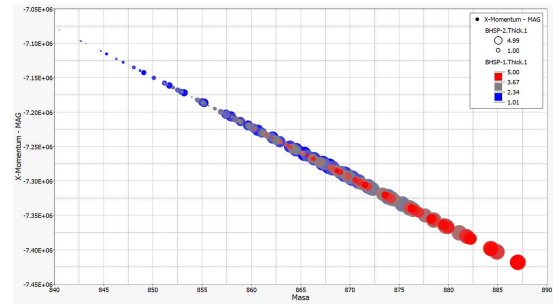
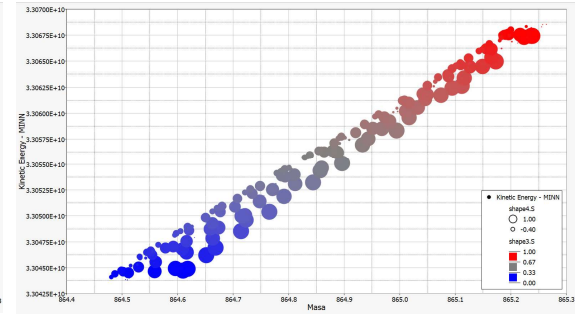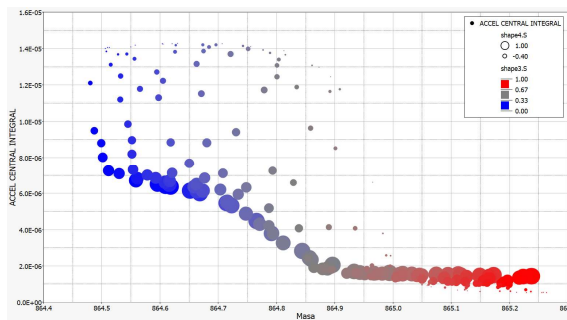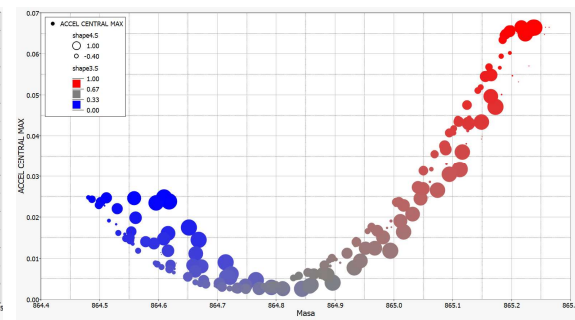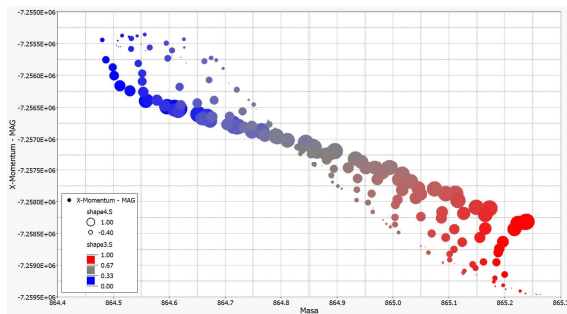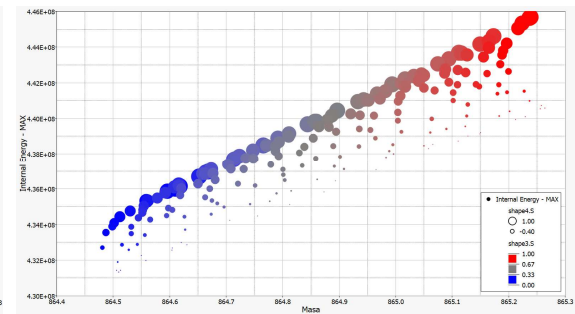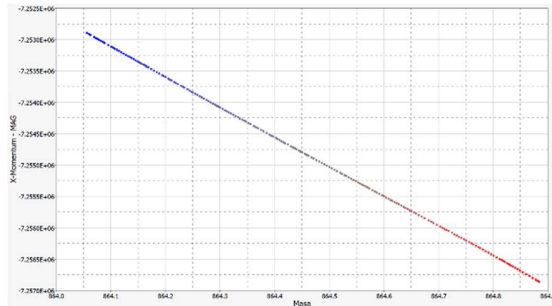Figure 3.53 - Graphic of scatter points with X axis as the weight and Y axis as the momentum in X
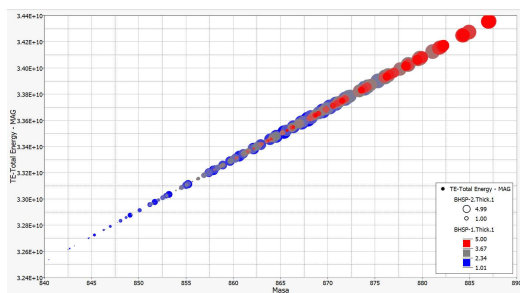
Figure 3.54 - Graphic of scatter points with X axis as the weight and Y axis as the total energy
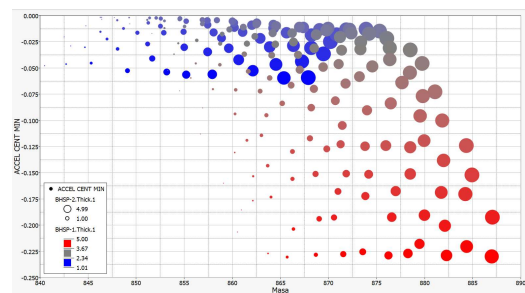
Figure 3.55 - Graphic of scatter points with X axis as the weight and Y axis as the acceleration on X of the node
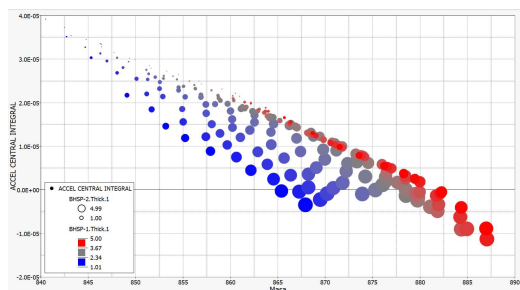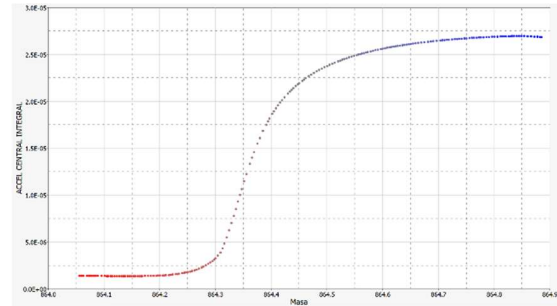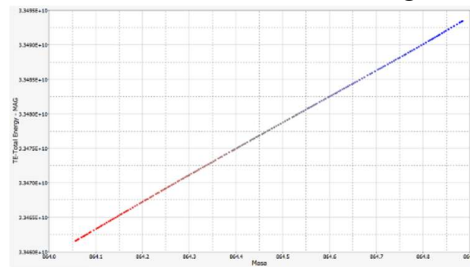

Figure 3.56 - Graphic of scatter points with X axis as the weight and Y axis as the integral acceleration of the node
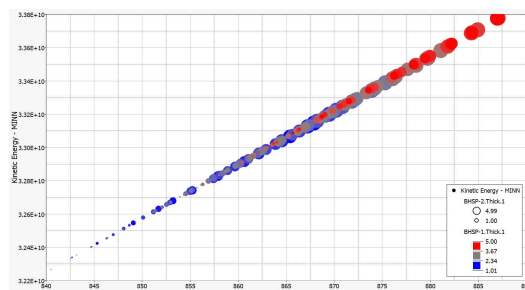
Figure 3.57 - Graphic of scatter points with X axis as the weight and Y axis as the kinetic energy

Both variables were plotted on the same goal, to minimize weight, maximize the internal energy approved on the model, reduce the kinetic energy on the model and reduce the acceleration on the central node. With these experiments the optimization method applied was the GRSM (Global Response Search Method).

In the second pair of the iteration the value of the sheet metal was between 1 and 5 mm, and the values chosen for the design of experiments using MELS.

It is crucial to indicate that the only values on the model that changes are the BHSP-3 and BHSP-4, creating the base thickness of the model on the rest of shell elements static at 3 mm. The resulting graphics of the BHSP3 are:
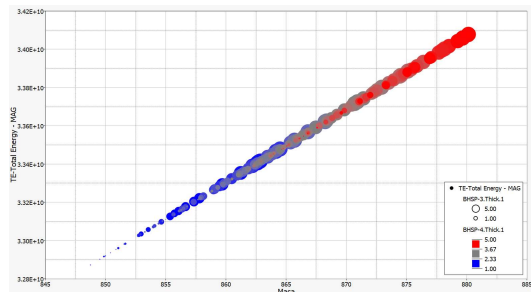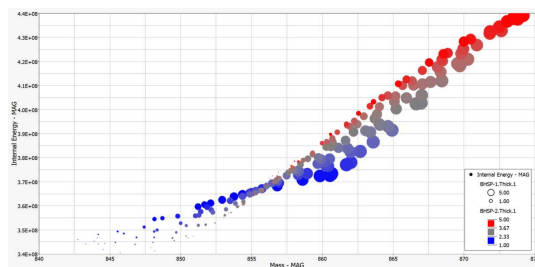

Figure 3.58 - Graphic of scatter points with X axis as the weight and Y axis as the total energy.
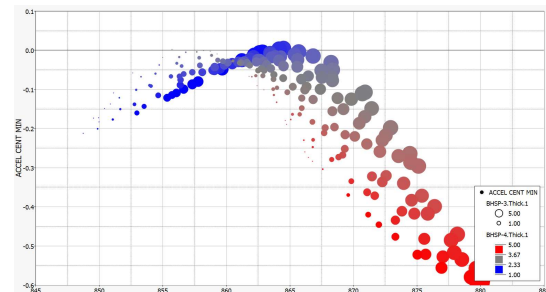
Figure 3.59 - Graphic of scatter points with X axis as the weight and Y axis as the minimum acceleration on the central node
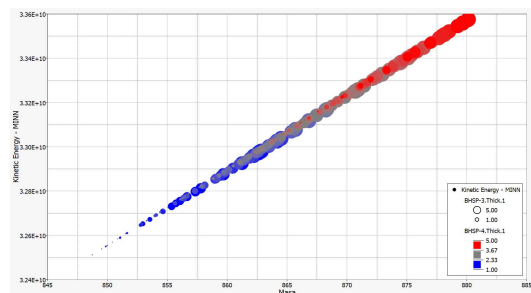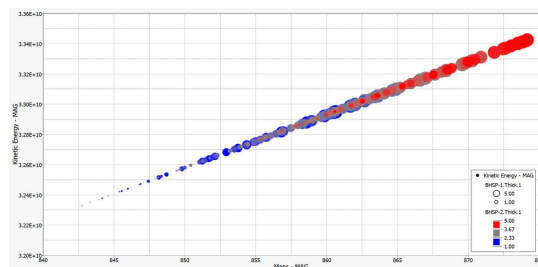

Figure 3.60 - Graphic of scatter points with X axis as the weight and Y axis as the kinetic energy.
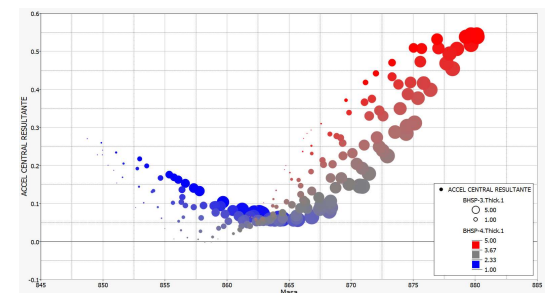
Figure 3.61 - Graphic of scatter points with X axis as the weight and Y axis as the resultant acceleration on the central node.
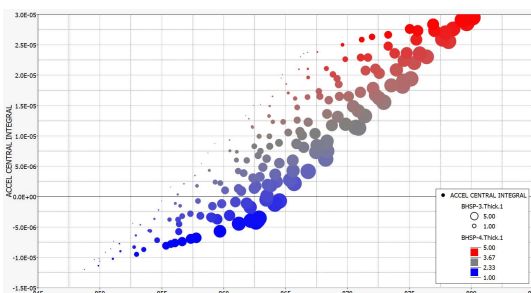
Figure 3.62 - Graphic of scatter points with X axis as the weight and Y axis as the integral acceleration on the central node.
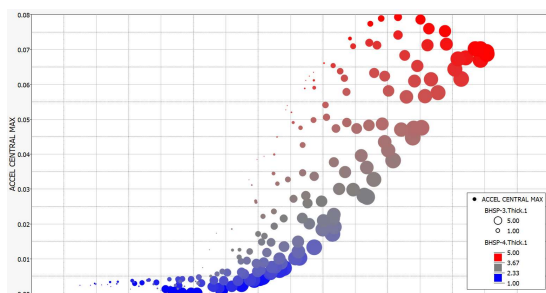
Figure 3.63 - Graphic of scatter points with X axis as the weight and Y axis as the maximum acceleration on the central node.
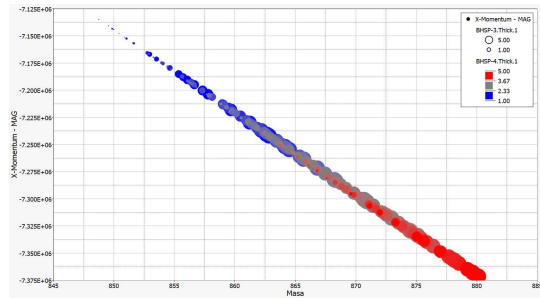
Figure 3.64 - Graphic of scatter points with X axis as the weight and Y axis as the momentum on x.
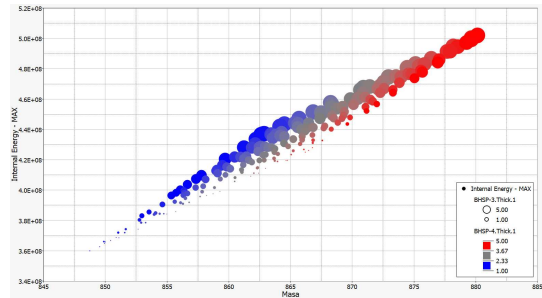
Figure 3.65 - Graphic of scatter points with X axis as the weight and Y axis as the internal energy.

Geometry variables

Similarly to the variable of the thickness, two designs were paired for them to observe the behavior and consist of seven experiments with two runs and the fifth design was experimented on in a separate environment.

It is crucial to indicate that the only values on the model that changes are the shape one and chape two, creating the base thickness of the model of shell elements static at 3 mm.

The resulting graphics of the shape one is:
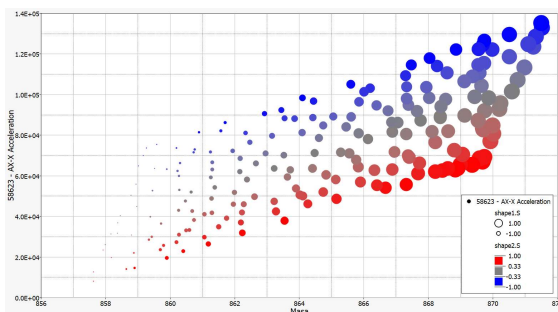
Figure 3.66 - Graphic of scatter points with X axis as the weight and Y axis as the acceleration on X node 58623.
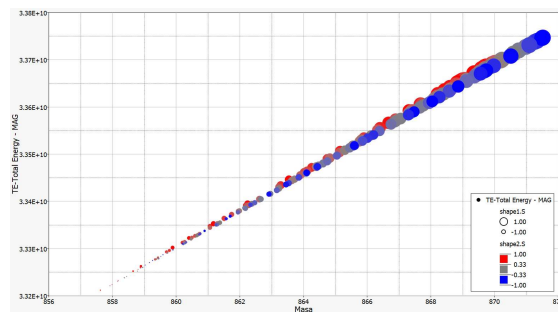
Figure 3.67 - Graphic of scatter points with X axis as the weight and Y axis as the total energy.
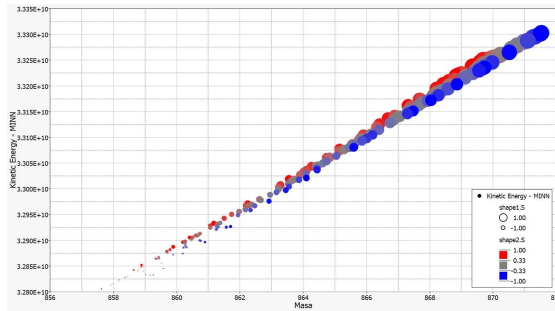
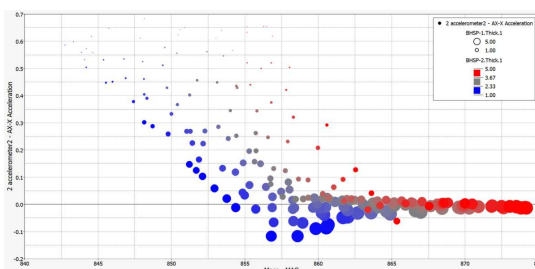Figure 3.68 - Graphic of scatter points with X axis as the weight and Y axis as the kinetic energy.
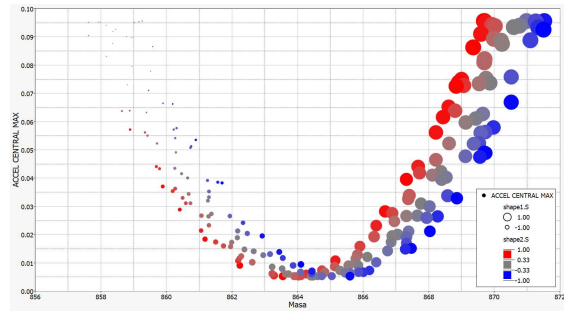
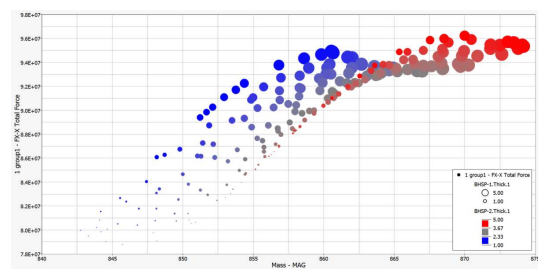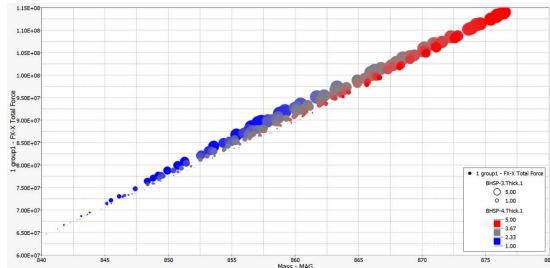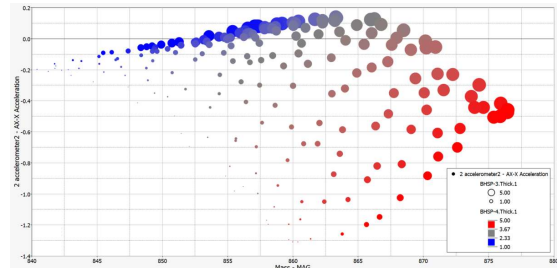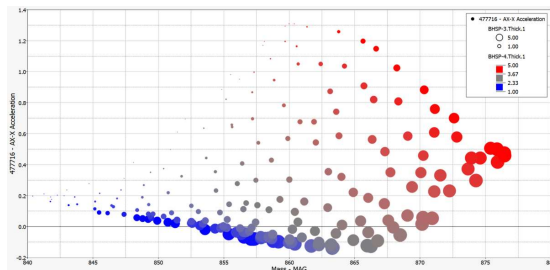Figure 3.69 - Graphic of scatter points with X axis as the weight and Y axis as the acceleration on X the central node.
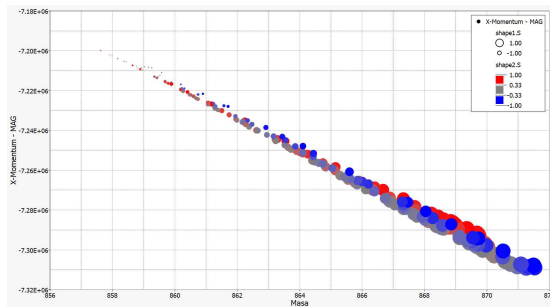
Figure 3.70 - Graphic of scatter points with X axis as the weight and Y axis as the momentum on X.
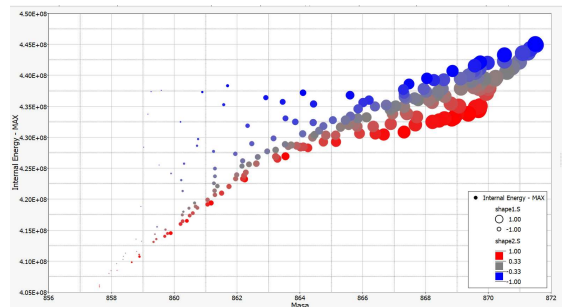
Figure 3.71 - Graphic of scatter points with X axis as the weight and Y axis as the internal energy.

Both variables were plotted on the same goal, to minimize weight, maximize the internal energy approved on the model, reduce the kinetic energy on the model and reduce the acceleration on the central node. With these experiments the optimization method applied was the GRSM.

In the second pair of the iteration the value of shape three was between 1 and 0, the value of shape four was between -.4 and one and the values chosen for the design of experiments using MELS.

It is crucial to indicate that the only values on the model that changes are shape one and shape two, creating the base thickness of the model of shell elements static at 3 mm.

The resulting graphics of the shape three are:
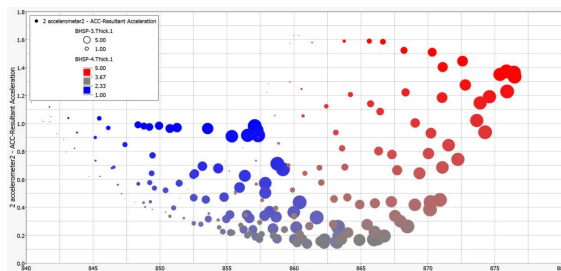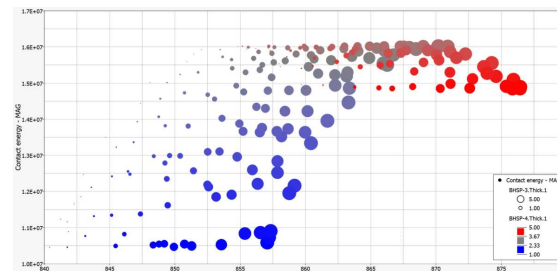
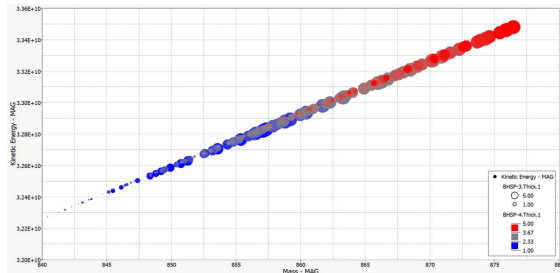Figure 3.72 - Graphic of scatter points with X axis as the weight and Y axis as the total energy.

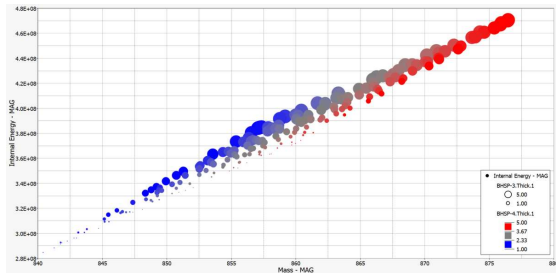Figure 3.73 - Graphic of scatter points with X axis as the weight and Y axis as the kinetic energy.

Figure 3.74 - Graphic scatter points with X axis as the weight and Y axis as the integral central acceleration.

Figure 3.75 - Graphic of scatter points with X axis as the weight and Y axis as the maximum central acceleration.

Figure 3.76 - Graphic of scatter points with X axis as the weight and Y axis as the momentum on X.

Figure 3.77 - Graphic of scatter points with X axis as the weight and Y axis as the internal energy.

Both variables were plotted on the same goal, to minimize weight, maximize the internal energy approved on the model, reduce the kinetic energy on the model and reduce the acceleration on the central node. With these experiments the optimization method applied was GRSM.

In the fifth variable of the iteration the value of the sheet metal was between one and -1, and the values chosen for the design of experiments using MELS.
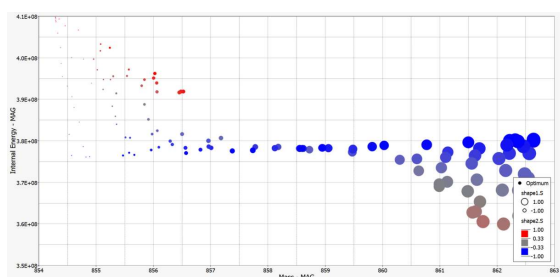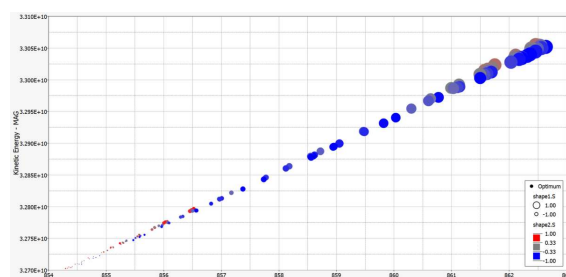
The resulting graphics of the shape five are:

Figure 3.78 - Graphic of scatter points with X axis as the weight and Y axis as the momentum on X.

Figure 3.79 - Graphic of scatter points with X axis as the weight and Y axis as the integral central acceleration.

Figure 3.80 - Graphic of scatter points with X axis as the weight and Y axis as the total energy.

For the first design of the external crash structure, the best output analysis was:

Table 3-42 - Results of optimal shapes on the first design of the external crash structure

Shape one	0
Shape two	-1
Shape three	0
Shape four	1
Shape five	.2

Table 3-43 – Results of optimal thickness on the first design of the external crash structure

Blue	1.23 mm
Green	3 mm
Red	3 mm
Yellow	1 mm

3.11.2 BH-2

The process in which the first design of the external crash structure had the next procedure along with the variables, both geometric and from thicknesses, according to each one. The design of this external crash structure.

Thicknesses

The variables in thickness were paired in external and internal, this constitutes the thicknesses that were explored in fourteen different experiments with two runs of seven each. The first pair explored was the thickness in the BHSP-1 and 2 and the second pair is in the BHSP-3 and 4.

It is crucial to indicate that the only values on the model that changes are the BHSP-1 and BHSP-2, creating the base thickness of the model on the rest of shell elements static at 3 mm. The resulting graphics of BHSP1 are:

Figure 3.81 – Graphic of scatter points with X axis as the weight and Y axis as the internal energy.

Figure 3.82 - Graphic of scatter points with X axis as the weight and Y axis as the kinetic energy.
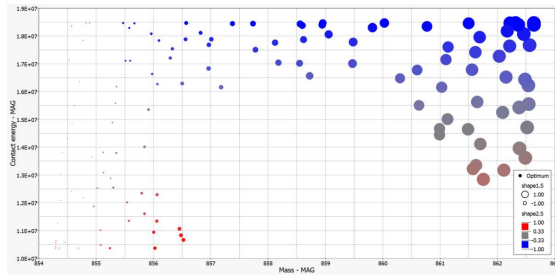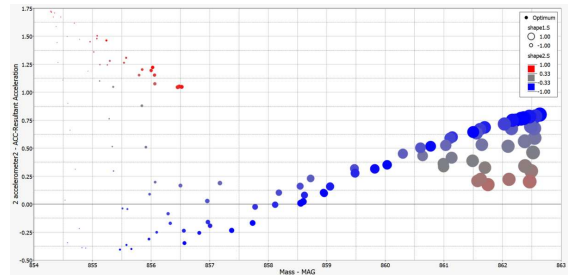

Figure 3.83 Graphic of scatter points with X axis as the weight and Y axis as the acceleration AX-X.

Figure 3.84 - Graphic of scatter points with X axis as the weight and Y axis as the total force.

In the second pair of the iteration the value of the sheet metal was between 1 and 5 mm, and the values chosen for the design of experiments using MELS.

It is crucial to indicate that the only values on the model that changes are the BHSP-3 and BHSP-4, creating the base thickness of the model on the rest of shell elements static at 3 mm. The resulting graphics of the BHSP3 are:

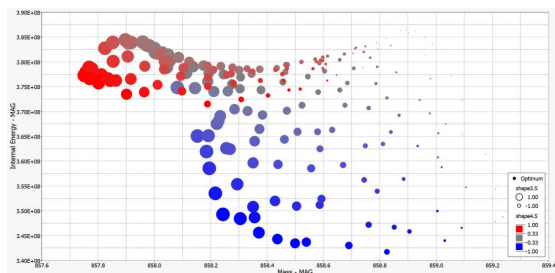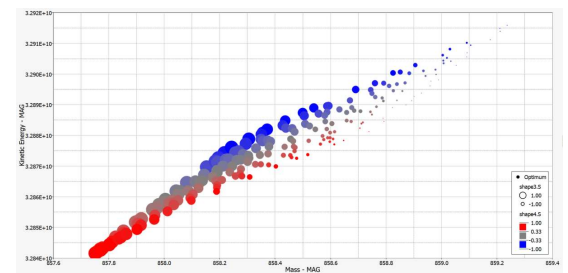Figure 3.85 - Graphic of scatter points with X axis as the weight and Y axis as the total force.

Figure 3.86 - Graphic of scatter points with X axis as the weight and Y axis as the maximum accelerometer value on AX-X.

Figure 3.87 - Graphic of scatter points with X axis as the weight and Y axis as the acceleration on node 477716.
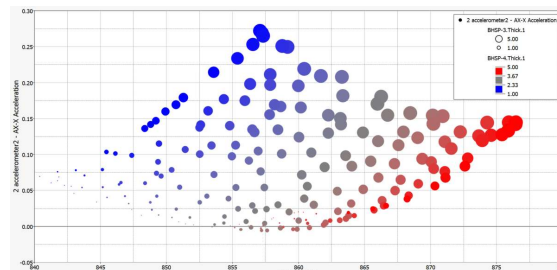
Figure 3.88 - Graphic of scatter points with X axis as the weight and Y axis as the minimum accelerometer value on AX-X.

Figure 3.89 - Graphic of scatter points with X axis as the weight and Y axis as the resultant accelerometer value.
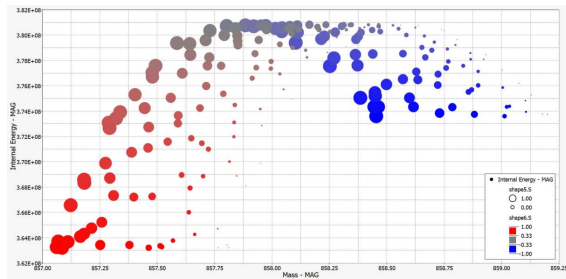

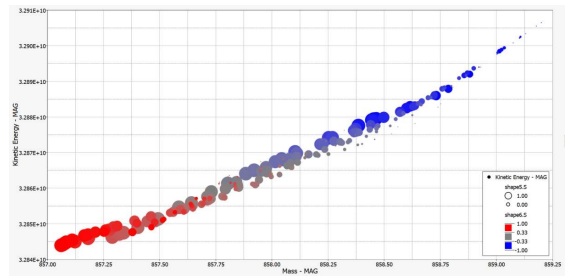Figure 3.90 - Graphic of scatter points with X axis as the weight and Y axis as the contact energy.

Figure 3.91 - Graphic of scatter points with X axis as the weight and Y axis as the kinetic energy.

Figure 3.92 - Graphic of scatter points with X axis as the weight and Y axis as the internal energy.

Geometry variables

Similarly to the variable of the thickness, designs were paired for them to observe the behavior and consist of seven experiments with three runs. In the first pair of the iteration the value of the sheet metal was between one and -1, and the values chosen for the design of experiments using MELS.

The optimization on the thicknesses from the shape one and shape two gave scatter points where it was calculated via the mathematical model to have a result on each point, giving a reference on how the outputs of the model behave after increasing the thickness of the shell elements. In each graphic the X axis has the weight of the model.

It is crucial to indicate that the only values on the model that changes are shape one and shape two, creating the base thickness of the model of shell elements static at 3 mm.

The resulting graphics of the shape one is:

Figure 3.93 - Graphic of scatter points with X axis as the weight and Y axis as the internal energy.

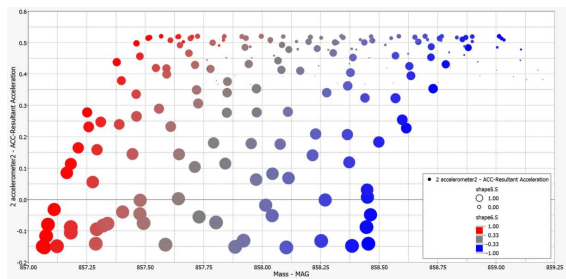Figure 3.94 - Graphic of scatter points with X axis as the weight and Y axis as the kinetic energy.

Figure 3.95 - Graphic of scatter points with X axis as the weight and Y axis as the contact energy.

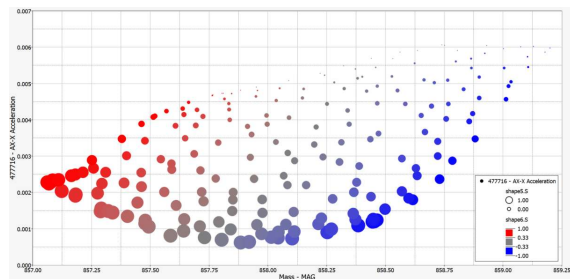Figure 3.96 - Graphic of scatter points with X axis as the weight and Y axis as the resultant value on the accelerometer.

Both variables were plotted on the same goal, to minimize weight, maximize the internal energy approved on the model, reduce the kinetic energy on the model and reduce the acceleration on the central node. With these experiments the optimization method applied was GRSM. In the second pair of the iteration the value of the sheet metal was between one and -1, and the values chosen for the design of experiments using MELS.

The optimization on the thicknesses from shape three and shape four gave scatter points where it was calculated via the mathematical model to have a result on each point, giving a reference on how the outputs of the model behave after increasing the thickness of the shell elements. In each graphic the X axis has the weight of the model.

It is crucial to indicate that the only values on the model that changes are shape three and shape four, creating the base thickness of the model of shell elements static at 3 mm.

The resulting graphics of Shape 3 are:
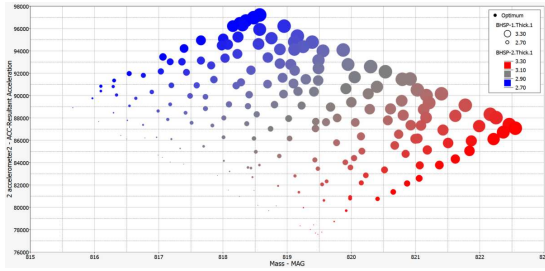

Figure 3.97 - Graphic of scatter points with X axis as the weight and Y axis as the internal energy.

Figure 3.98 - Graphic of scatter points with X axis as the weight and Y axis as the kinetic energy.

In the third pair of the iteration the value of the sheet metal was between one and -1, and the values chosen for the design of experiments using MELS.

The optimization on the thicknesses from shape five and shape six gave scatter points where it was calculated via the mathematical model to have a result on each point, giving a reference

on how the outputs of the model behave after increasing the thickness of the shell elements. In each graphic the X axis has the weight of the model.

It is crucial to indicate that the only values on the model that changes are shape five and shape six, creating the base thickness of the model of shell elements static at 3 mm.

The resulting graphics of Shape 5 are:

Figure 3.99 - Graphic of scatter points with X axis as the weight and Y axis as the internal energy.
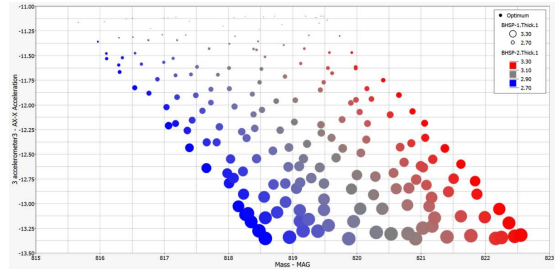

Figure 3.100 - Graphic of scatter points with X axis as the weight and Y axis as the kinetic energy.

Figure 3.101 - Graphic of scatter points with X axis as the weight and Y axis as the resultant central acceleration.

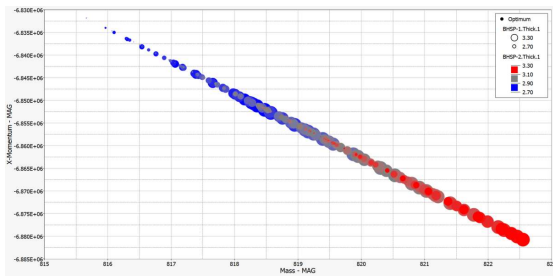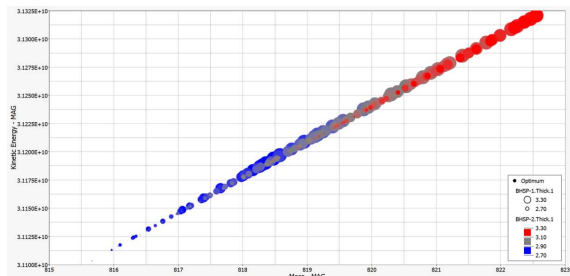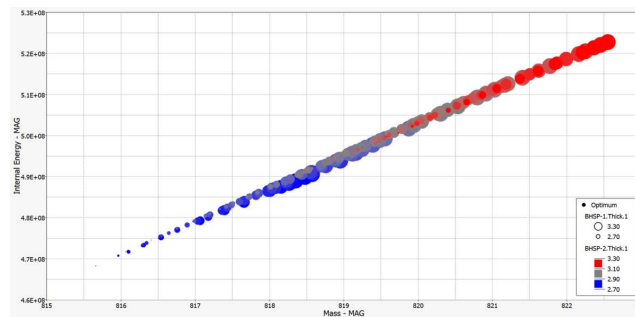Figure 3.102 - Graphic of scatter points with X axis as the weight and Y axis as the acceleration on X of node 477716.
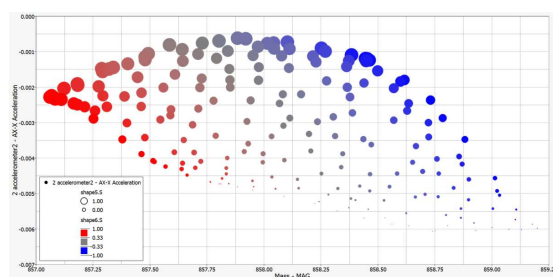
Figure 3.103 - Graphic of scatter points with X axis as the weight and Y axis as acceleration

For the second design of the external crash structure, the best output analysis was:

Table 3-44 – Results of optimal shapes on the second design of the external crash structure

Shape one	-1
Shape two	+1
Shape three	-1
Shape four	-1
Shape five	-1
Shape six	0

Table 3-45 – Results of optimal thickness on the second design of the external crash structure

Orange	1 mm
Blue	3 mm
Green	3 mm
Purple	1 mm

3.11.3 BH-3

The process in which the first design of the external crash structure had the next procedure along with the variables, both geometric and from thicknesses, according to each one. The design of this external crash structure.

Thicknesses

The variables in thickness were paired in external and internal, this constitutes the thicknesses that were explored in fourteen different experiments with two runs of seven each. The first pair explored was the thickness in BHSP-1 and 2 and the second pair is in BHSP-3 and 4. In the first pair of the iteration the value of the sheet metal was between 1 and 5 mm, and the values chosen for the design of experiments using MELS.

The optimization on the thicknesses from the BHSP-1 and BHSP-2 gave scatter points where it was calculated via the mathematical model to have a result on each point, giving a reference on how the outputs of the model behave after increasing the thickness of the shell elements. In each graphic the X axis has the weight of the model.

It is crucial to indicate that the only values on the model that changes are the BHSP-1 and BHSP-2, creating the base thickness of the model on the rest of shell elements static at 3 mm. The resulting graphics of BHSP1 are:
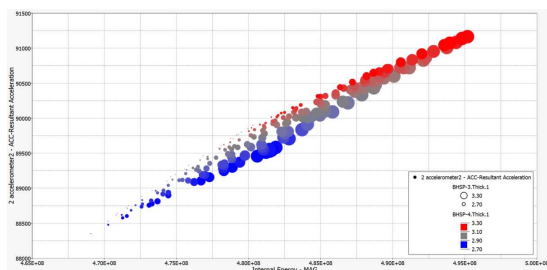
Figure 3.104 - Graphic of scatter points with X axis as the weight and Y axis as the resultant central acceleration.
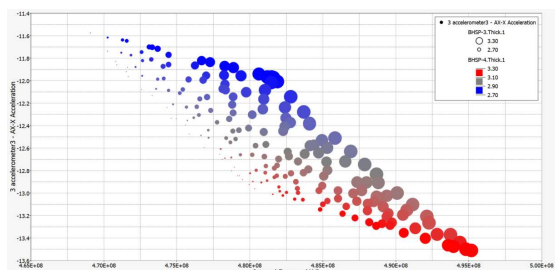

Figure 3.105 - Graphic of scatter points with X axis as the weight and Y axis as the acceleration con AX-X.
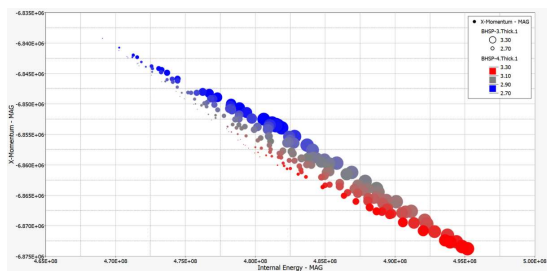

Figure 3.106 - Graphic of scatter points with X axis as the weight and Y axis as the momentum on X.
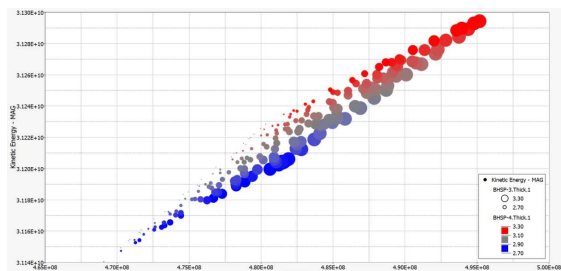

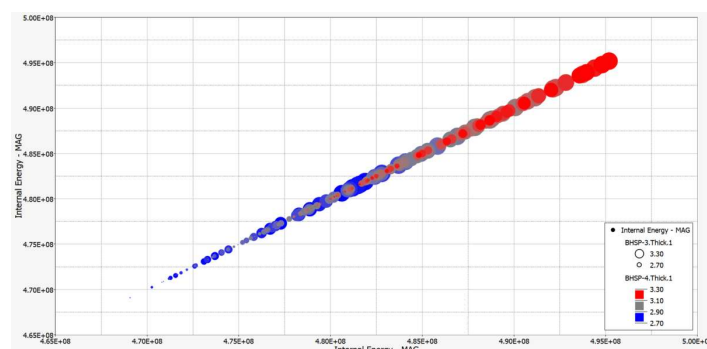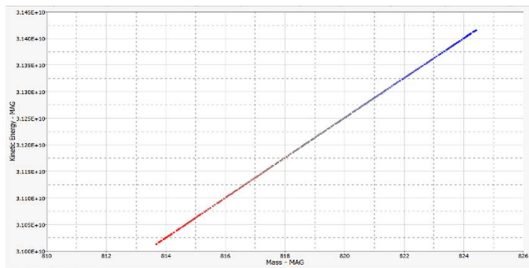Figure 3.107 - Graphic of scatter points with X axis as the weight and Y axis as the kinetic energy.

Figure 3.108 - Graphic of scatter points with X axis as the weight and Y axis as the internal energy.

Both variables were plotted on the same goal, to minimize weight, maximize the internal energy approved on the model, reduce the kinetic energy on the model and reduce the acceleration on the central node. With these experiments the optimization method applied was GRSM.

In the second pair of the iteration the value of the sheet metal was between 1 and 5 mm, and the values chosen for the design of experiments using MELS.

The optimization on the thicknesses from the BHSP-3 and BHSP-4 gave scatter points where it was calculated via the mathematical model to have a result on each point, giving a reference on how the outputs of the model behave after increasing the thickness of the shell elements. In each graphic the X axis has the weight of the model.

It is crucial to indicate that the only values on the model that changes are the BHSP-3 and BHSP-4, creating the base thickness of the model on the rest of shell elements static at 3 mm. The resulting graphics of the BHSP3 are:

Figure 3.109 - Graphic of scatter points with X axis as the weight and Y axis as the resultant central acceleration.

Figure 3.110 - Graphic of scatter points with X axis as the weight and Y axis as the acceleration con AX-X.
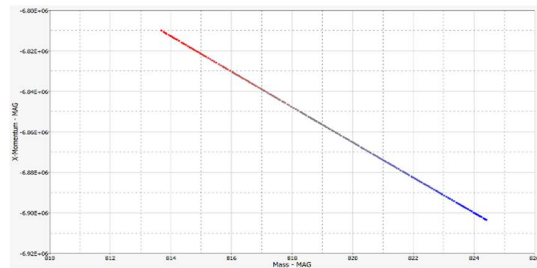

Figure 3.111 - Graphic of scatter points with X axis as the weight and Y axis as the momentum on X.

Figure 3.112 - Graphic of scatter points with X axis as the weight and Y axis as the kinetic energy.

Figure 3.113 - Graphic of scatter points with X axis as the weight and Y axis as the internal energy.

Geometry variables

Similarly to the variable of thickness, designs were paired for them to observe the behavior and consist of seven experiments with three runs and the seventh design was experimented on in a separate environment.

In the first variable of the iteration the value of the sheet metal was between one and -1, and the values chosen for the design of experiments using MELS.

The resulting graphics of the shape one is:

Figure 3.114 - Graphic of scatter points with X axis as the weight and Y axis as the kinetic energy.

Figure 3.115 - Graphic of scatter points with X axis as the weight and Y axis as the momentum on X.
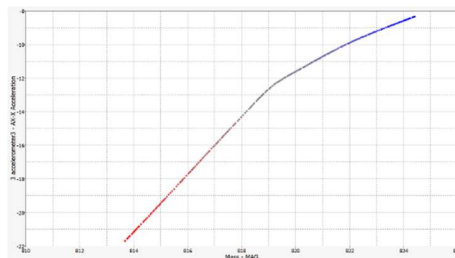
Figure 3.116 - Graphic of scatter points with X axis as the weight and Y axis as the acceleration of accelerometer AX-X.

In the first pair of the iteration the value of the sheet metal was between one and -1, and the values chosen for the design of experiments using MELS.

The optimization on the thicknesses from the shape two and shape three gave scatter points where it was calculated via the mathematical model to have a result on each point, giving a reference on how the outputs of the model behave after increasing the thickness of the shell elements. In each graphic the X axis has the weight of the model.

It is crucial to indicate that the only values on the model that changes are shape two and shape three, creating the base thickness of the model of shell elements static at 3 mm.

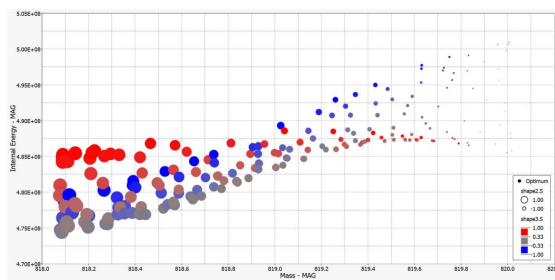The resulting graphics of the shape two are:

Figure 3.117 - Graphic of scatter points with X axis as the weight and Y axis as the internal energy.
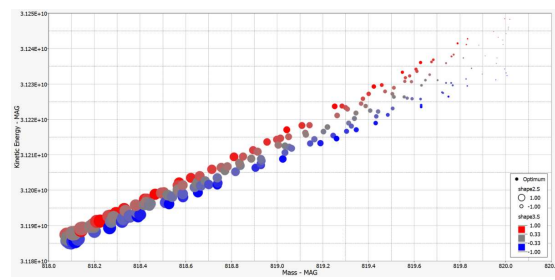

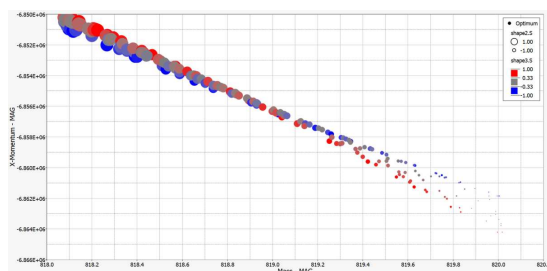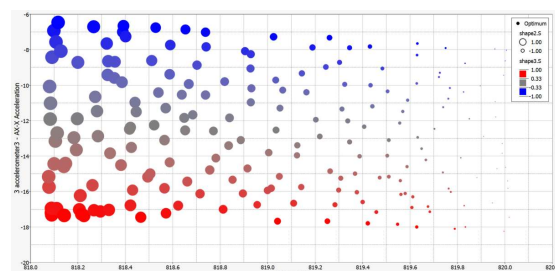Figure 3.118 - Graphic of scatter points with X axis as the weight and Y axis as the kinetic energy.

Figure 3.119 - Graphic of scatter points with X axis as the weight and Y axis as the momentum on X.

Figure 3.120 - Graphic of scatter points with X axis as the weight and Y axis as the acceleration on AX-X on accelerometer.

Both variables were plotted on the same goal, to minimize weight, maximize the internal energy approved on the model, reduce the kinetic energy on the model and reduce the acceleration on the central node. With these experiments the optimization method applied were the GRSM.

In the second pair of the iteration the value of the sheet metal was between one and -1, and the values chosen for the design of experiments using MELS.

The optimization on the thicknesses from the shape four and shape five gave scatter points where it was calculated via the mathematical model to have a result on each point, giving a reference on how the outputs of the model behave after increasing the thickness of the shell elements. In each graphic the X axis has the weight of the model.

It is crucial to indicate that the only values on the model that changes are shape three and shape four, creating the base thickness of the model of shell elements static at 3 mm.
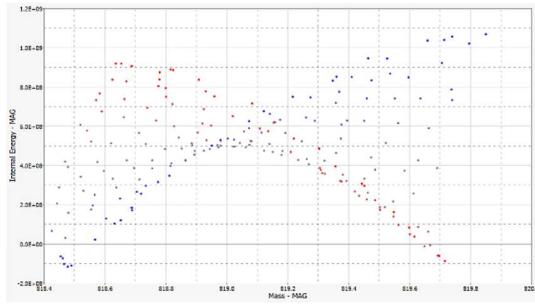
The resulting graphics of Shape 5 are:

Figure 3.121 - Graphic of scatter points with X axis as the weight and Y axis as the internal energy.
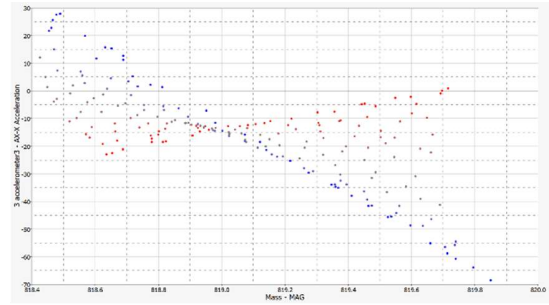

Figure 3.122 - Graphic of scatter points with X axis as the weight and Y axis as the acceleration on AX-X on accelerometer.
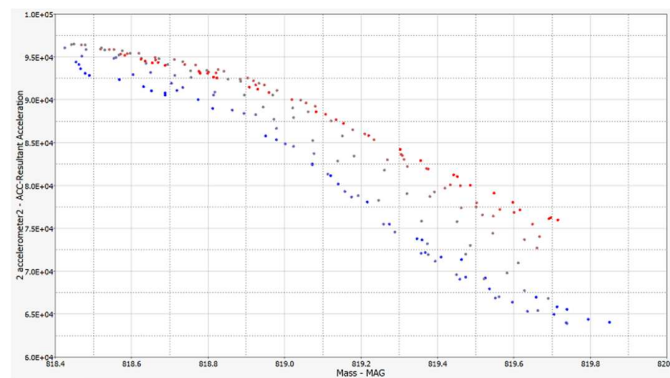

Figure 3.123 - Graphic of scatter points with X axis as the weight and Y axis as the acceleration on accelerometer.

In the third pair of the iteration the value of the sheet metal was between one and -1, and the values chosen for the design of experiments using MELS.

The optimization on the thicknesses from the shape six and shape seven gave scatter points where it was calculated via the mathematical model to have a result on each point, giving a reference on how the outputs of the model behave after increasing the thickness of the shell elements. In each graphic the X axis has the weight of the model.

It is crucial to indicate that the only values on the model that changes are shape six and shape seven, creating the base thickness of the model of shell elements static at 3 mm.

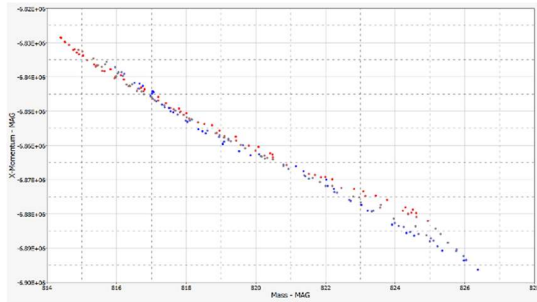The resulting graphics of Shape 6 are:

Figure 3.124 - Graphic of scatter points with X axis as the weight and Y axis as the momentum on X.
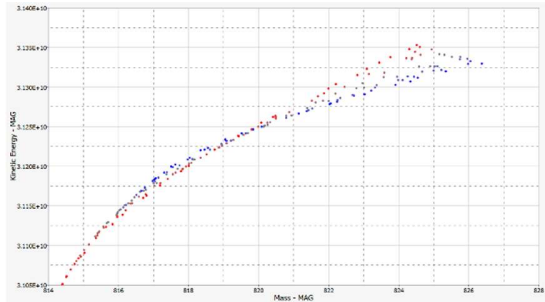

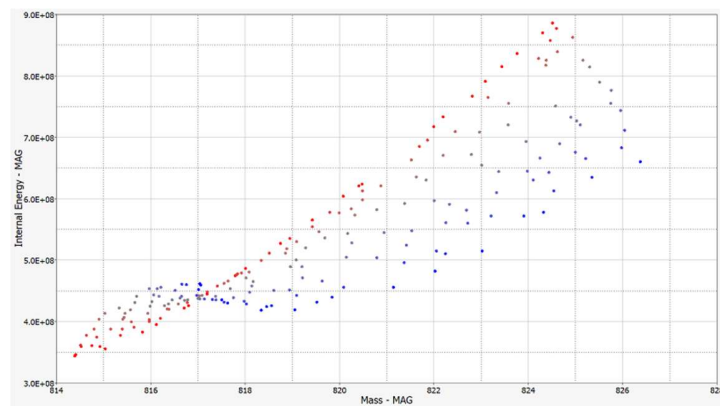Figure 3.125 - Graphic of scatter points with X axis as the weight and Y axis as the kinetic energy.

Figure 3.126 - Graphic of scatter points with X axis as the weight and Y axis as the internal energy.

For the third design of the external crash structure, the best output analysis was:

Table 3-46 – Results of optimal shapes on the third design of the external crash

Shape one	.2
Shape two	0
Shape three	-1
Shape four	-1
Shape five	-1
Shape six	0
Shape seven	-1

Table 3-47 – Results of optimal thickness on the third design of the external crash structure.

Blue	1 mm
Green	3 mm
Red	3 mm
Yellow	1 mm

3.11.4 External sheet - 1

The process in which the first design of the external sheet had the next procedure along with the variables, both geometric and from thickness, according to each one. The design of this external crash structure.

Thickness

The variables in thickness were paired in external and internal, this constitutes the thicknesses that were explored in one experiment with one run.

The optimization on the thickness from the EXT-SH gave scatter points where it was calculated via the mathematical model to have a result on each point, giving a reference on how the outputs of the model behave after increasing the thickness of the shell elements. In each graphic the X axis has the weight of the model.

It is crucial to indicate that the only value on the model that changes is the EXT-SH, creating the base thickness of the model on the rest of the shell elements static at 3 mm.

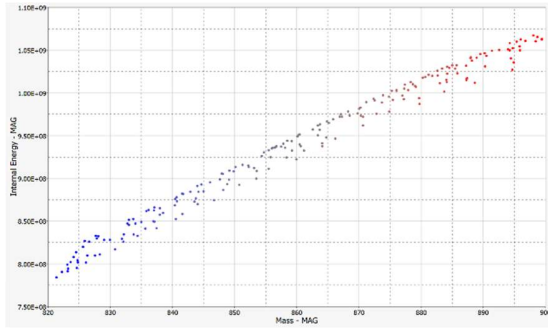The resulting graphics of the EXT-SH are:

Figure 3.127 - Graphic of scatter points with X axis as the weight and Y axis as the internal energy.
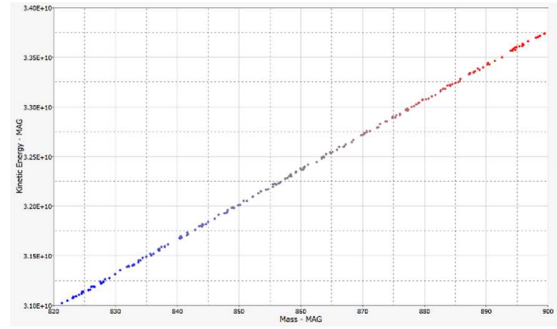

Figure 3.128 - Graphic of scatter points with X axis as the weight and Y axis as the kinetic energy.
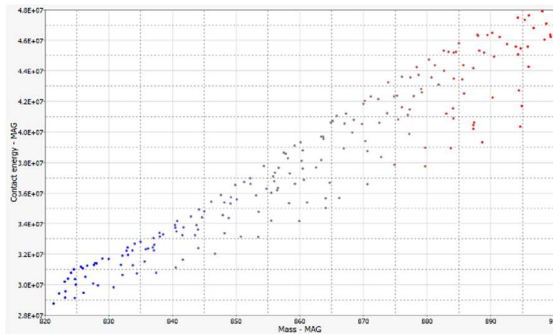

Figure 3.129 - Graphic of scatter points with X axis as the weight and Y axis as the contact energy
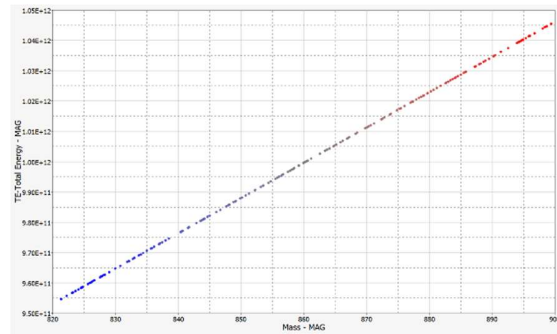

Figure 3.130 - Graphic of scatter points with X axis as the weight and Y axis as the total energy
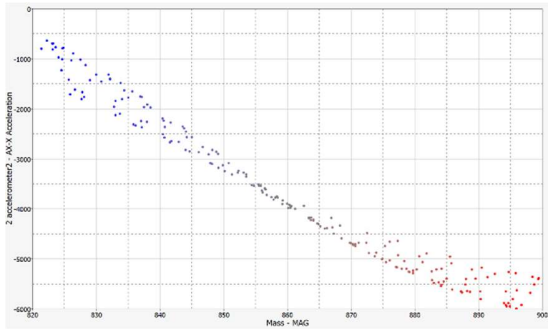

Figure 3.131 - Graphic scatter points with X axis as the weight and Y axis as the acceleration on AX-X.
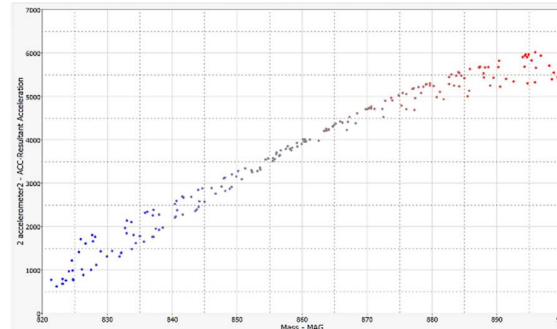

Figure 3.132 - Graphic of scatter points with X axis as the weight and Y axis as the resultant acceleration on ACC.

The variable was plotted on the same goal, to minimize weight, maximize the internal energy approved on the model, reduce the kinetic energy on the model and reduce the acceleration on the central node. With these experiments the optimization method applied was GRSM.

Geometry variables

Similarly to the variable of the thickness, two designs were paired for them to observe the behavior and consist of seven experiments with two runs and the fifth design was experimented on in a separate environment.

In the first pair of the iteration the value of the shapes 1 and 2 were between one and -1, and the values chosen for the design of experiments using MELS.

The optimization on the thicknesses from the shape one and shape two gave scatter points where it was calculated via the mathematical model to have a result on each point, giving a reference on how the outputs of the model behave after increasing the thickness of the shell elements. In each graphic the X axis has the weight of the model.

It is crucial to indicate that the only values on the model that changes are the shape one and chape two, creating the base thickness of the model of shell elements static at 3 mm.

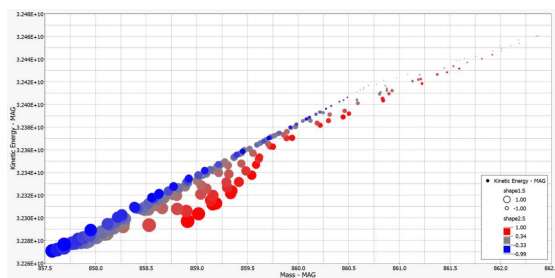The resulting graphics of the shape one is:

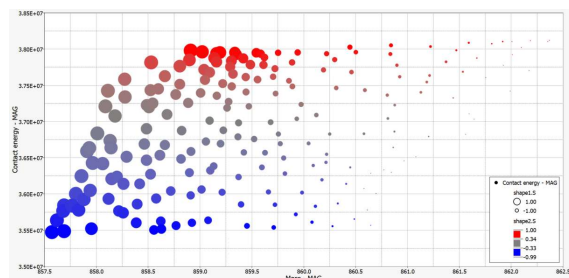Figure 3.133 - Graphic of scatter points with X axis as the weight and Y axis as the kinetic energy.

Figure 3.134 - Graphic of scatter points with X axis as the weight and Y axis as the contact energy.
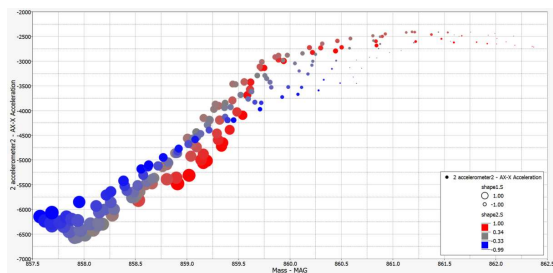
Figure 3.135 - Graphic of scatter points with X axis as the weight and Y axis as the Accelerometer - AX-X Acceleration.
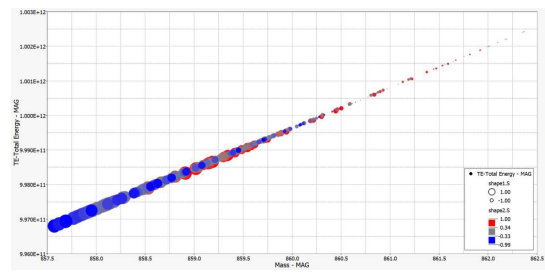

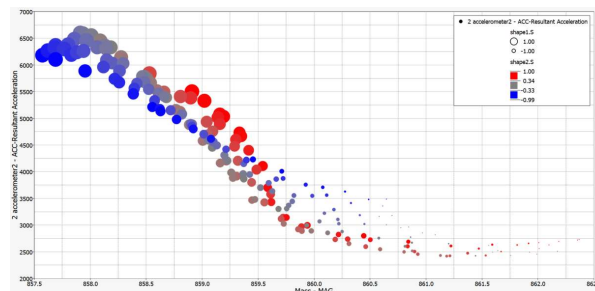Figure 3.136 - Graphic of scatter points with X axis as the weight and Y axis as the total energy.

Figure 3.137 - Graphic of scatter points with X axis as the weight and Y axis as the accelerometer - ACC-Resultant Acceleration.

Both variables were plotted on the same goal, to minimize weight, maximize the internal energy approved on the model, reduce the kinetic energy on the model and reduce the acceleration on the central node. With these experiments the optimization method applied was GRSM.

For the design of the external sheet metal, the best output analysis was:

Table 3-48 - Results of optimal shapes on the design of the external sheet cover

Shape one	-1
Shape two	1

Table 3-49 - Results of optimal thickness on the design of the external sheet cover

EXT-SH	1 mm

3.11.5 Pillar - 1

The process in which the second design of the pillar structure had the next procedure along with the variables, both geometric and from thicknesses, according to each one.

Thickness

The variables in thickness were paired in external and internal, this constitutes the thicknesses that were explored in one experiment with one run.

The optimization on the thickness gave scatter points where it was calculated via the mathematical model to have a result on each point, giving a reference on how the outputs of the model behave after increasing the thickness of the shell elements. In each graphic the X axis has the weight of the model.

It is crucial to indicate that the only value on the model that changes is the EXT-SH, creating the base thickness of the model on the rest of the shell elements static at 3 mm.

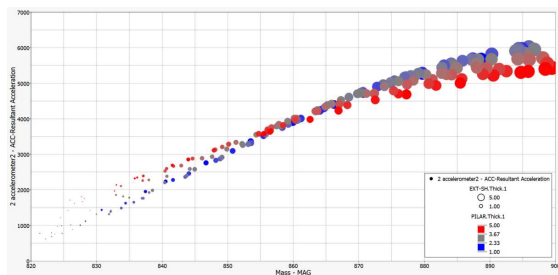The resulting graphics of the Pillar are:

Figure 3.138 - Graphic of scatter points with X axis as the weight and Y axis as the ACC-Resultant Acceleration.
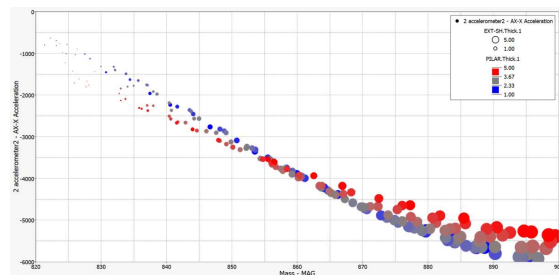

Figure 3.139 - Graphic of scatter points with X axis as the weight and Y axis as the AX-X Acceleration.
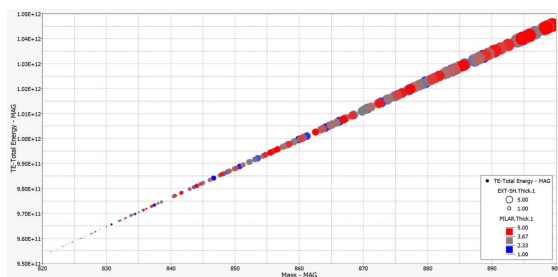

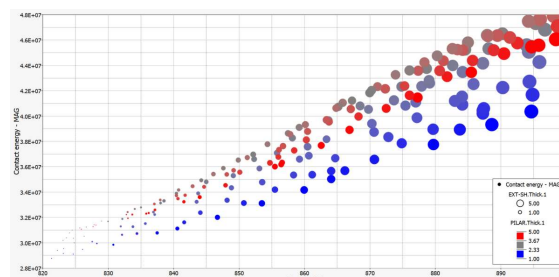Figure 3.140 - Graphic of scatter points with X axis as the weight and Y axis as the total energy

Figure 3.141 - Graphic of scatter points with X axis as the weight and Y axis as the contact energy
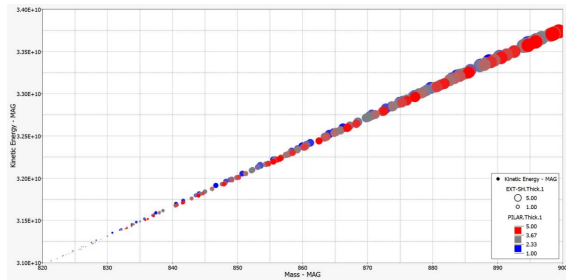
Figure 3.142 - Graphic of scatter points with X axis as the weight and Y axis as the kinetic energy.
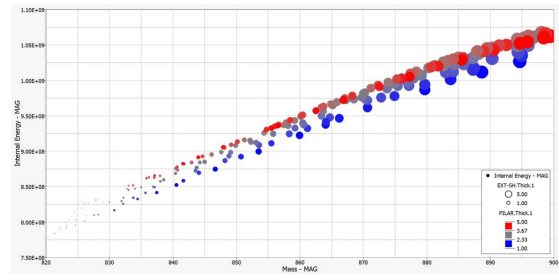

Figure 3.143 - Graphic of scatter points with X axis as the weight and Y axis as the internal energy.

The variable was plotted on the same goal, to minimize weight, maximize the internal energy approved on the model, reduce the kinetic energy on the model and reduce the acceleration on the central node. With these experiments the optimization method applied was GRSM.

Geometry variables

Similarly to the variable of the thickness, two designs were paired for them to observe the behavior and consist of seven experiments with two runs, in the geometric variables there are five variations.

In the first pair of the iteration the value of the shapes 1 and 2 were between one and -1, and the values chosen for the design of experiments using MELS.

The optimization on the thicknesses from the shape one and shape two gave scatter points where it was calculated via the mathematical model to have a result on each point, giving a reference on how the outputs of the model behave after increasing the thickness of the shell elements. In each graphic the X axis has the weight of the model.

It is crucial to indicate that the only values on the model that changes are the shape one and chape two, creating the base thickness of the model of shell elements static at 3 mm.

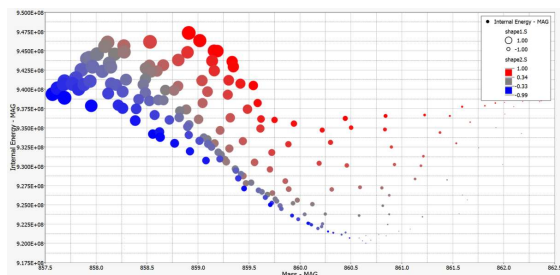The resulting graphics of the shape one is:

Figure 3.144 – Graphic of scatter points with X axis as the weight and Y axis as the kinetic energy.
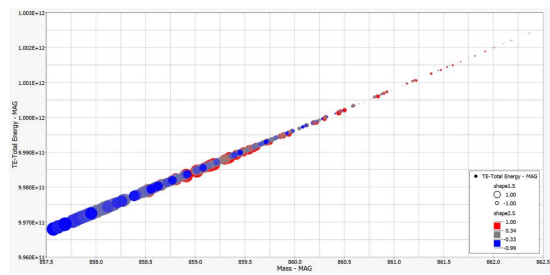

Figure 3.145 - Graphic of scatter points with X axis as the weight and Y axis as the total energy.

Both variables were plotted on the same goal, to minimize weight, maximize the internal energy approved on the model, reduce the kinetic energy on the model and reduce the acceleration on the central node. With these experiments the optimization method applied was GRSM.

For the first design in the pillar, the best output analysis was:

Table 3-50 – Results of optimal shapes on the first design of the pillars

Shape one	N/A
Shape two	-1

Table 3-51 – Results of optimal thickness on the first design of the pillars

PILLAR	2 mm

3.11.6 Pillar - 2

The process in which the second design of the pillar structure had the next procedure along with the variables, both geometric and from thicknesses, according to each one.

Thickness

The variables in thickness were paired in external and internal, this constitutes the thicknesses that were explored in one experiment with one run. The optimization on the thickness gave scatter points where it was calculated via the mathematical model to have a result on each

point, giving a reference on how the outputs of the model behave after increasing the thickness of the shell elements. In each graphic the X axis has the weight of the model.

It is crucial to indicate that the only value on the model that changes is the EXT-SH, creating the base thickness of the model on the rest of the shell elements static at 3 mm.

The resulting graphics of the Pillar are:

Figure 3.146 – Graphic of scatter points with X axis as the weight and Y axis as the internal energy.

Figure 3.147 - Graphic of scatter points with X axis as the weight and Y axis as the kinetic energy.

Figure 3.148 - Graphic of scatter points with X axis as the weight and Y axis as the contact energy.
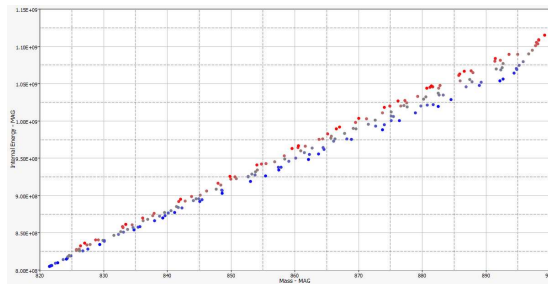

Figure 3.149 - Graphic of scatter points with X axis as the weight and Y axis as the total energy.

Figure 3.150 - Graphic of scatter points with X axis as the weight and Y axis as the integral acceleration of the node.

Figure 3.151 - Graphic of scatter points with X axis as the weight and Y axis as the resultant acceleration of the node.
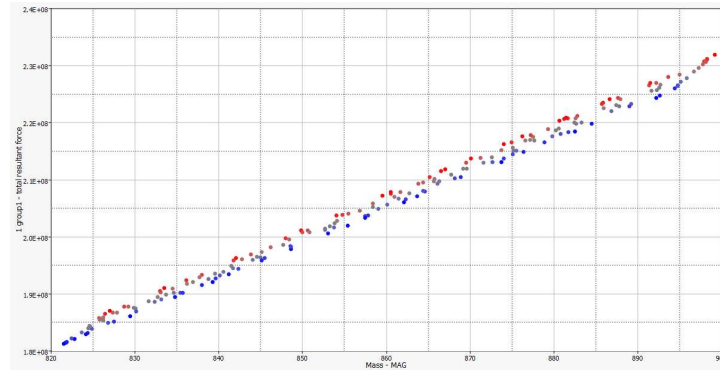
Figure 3.152 - Graphic of scatter points with X axis as the weight and Y axis as the group energy

The variable was plotted on the same goal, to minimize weight, maximize the internal energy approved on the model, reduce the kinetic energy on the model and reduce the acceleration on the central node. With these experiments the optimization method applied was GRSM.

Geometry variables

Similarly to the variable of the thickness, two designs were paired for them to observe the behavior and consist of seven experiments with two runs. In the first pair of the iteration the value of the shapes 1 and 2 were between one and -1, and the values chosen for the design of experiments using MELS.

The optimization on the thicknesses from the shape one and shape two gave scatter points where it was calculated via the mathematical model to have a result on each point, giving a reference on how the outputs of the model behave after increasing the thickness of the shell elements. In each graphic the X axis has the weight of the model. It is crucial to indicate that the only values on the model that changes are the shape one and chape two, creating the base thickness of the model of shell elements static at 3 mm.

The resulting graphics of the shape one is:

Figure 3.153 - – Graphic of scatter points with X axis as the weight and Y axis as the internal energy.

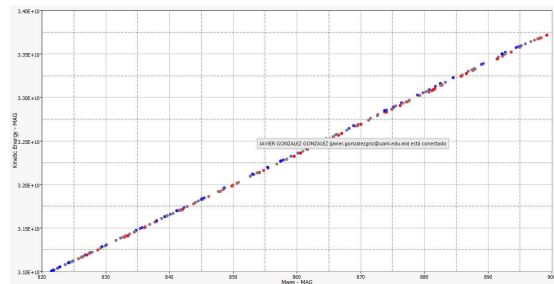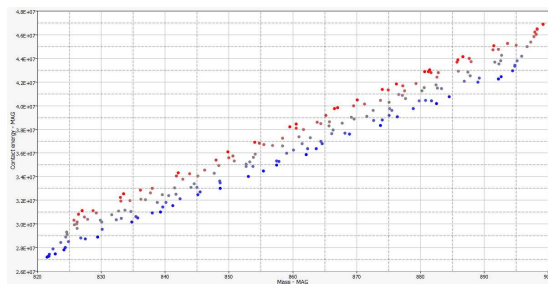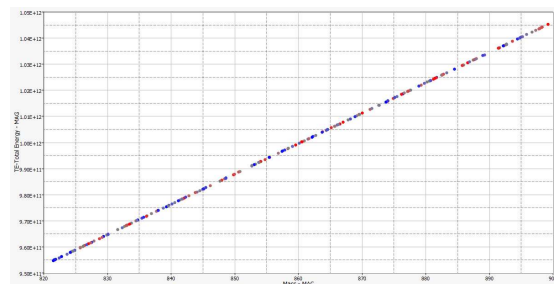Figure 3.154 - Graphic of scatter points with X axis as the weight and Y axis as the total energy.
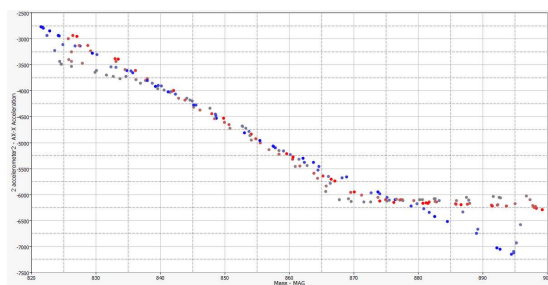

Figure 3.155 - Graphic of scatter points with X axis as the weight and Y axis as the two accelerometer2 - AX-X Acceleration.
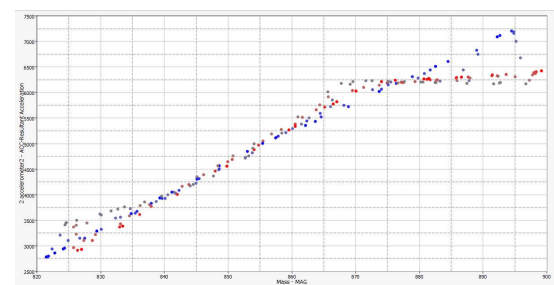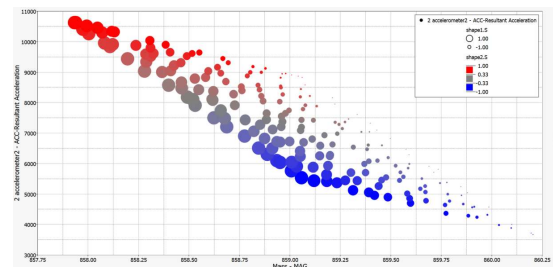

Figure 3.156 - Graphic of scatter points with X axis as the weight and Y axis as the two accelerometer - Resultant Acceleration.

Both variables were plotted on the same goal, to minimize weight, maximize the internal energy approved on the model, reduce the kinetic energy on the model and reduce the acceleration on the central node. With these experiments the optimization method applied was GRSM.

For the second design in the pillar, the best output analyzed was:

Table 3-52 – Results of optimal shapes on the first design of the pillars

Shape one	-1
Shape two	+1

Table 3-53 – Results of optimal thickness on the first design of the pillars

PILLAR	2 mm

3.11.7 Thermal analysis

The process in which thermal analysis had the next procedure along with the variables, both geometric and from thicknesses, according to each one. The design of the upper and lower cover for thermal isolation.

Thickness

The variables in thickness were paired in external and internal, this constitutes the thicknesses that were explored in one experiment with one run.

The optimization on the thicknesses gave scatter points where it was calculated via the mathematical model to have a result on each point, giving a reference on how the outputs of the model behave after increasing the thickness of the shell elements. In each graphic the X axis has the weight of the model.

It is crucial to indicate that the only value on the model changes, creating the base thickness of the model on the rest of the shell elements static at 3 mm.

The resulting graphics of the thickness are:

Figure 3.157 – Graphic of scatter points with X axis as the weight and Y axis as the maximum upper cover temperature.

Figure 3.158 - Graphic of scatter points with X axis as the weight and Y axis as the average upper cover temperature.
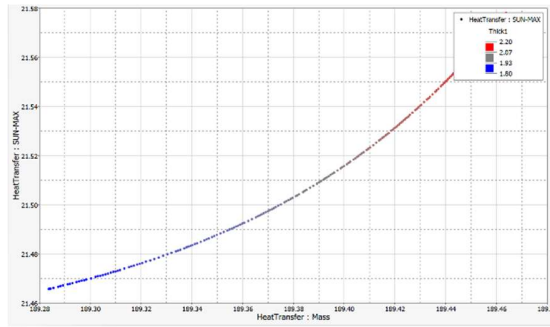
Figure 3.159 - Graphic of scatter points with X axis as the weight and Y axis as the total maximum total temperature.
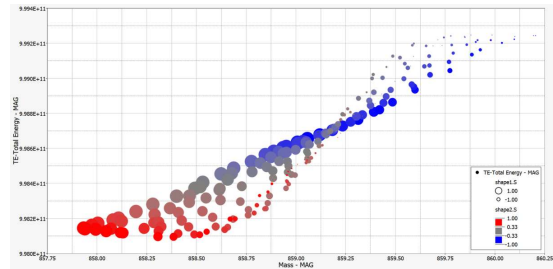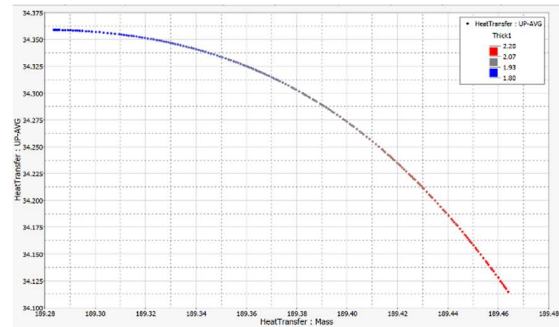

Figure 3.160 - Graphic of scatter points with X axis as the weight and Y axis as the average total temperature.
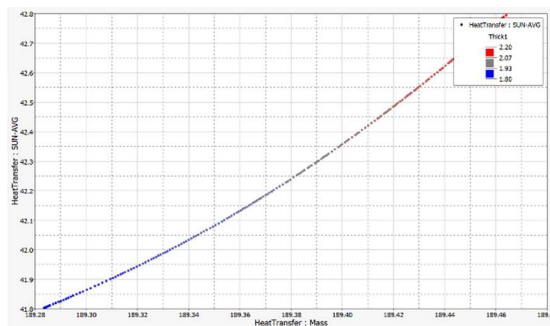
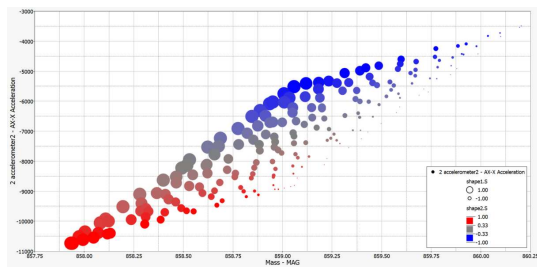Figure 3.161 - Graphic of scatter points with X axis as the weight and Y axis as the maximum bottom temperature.
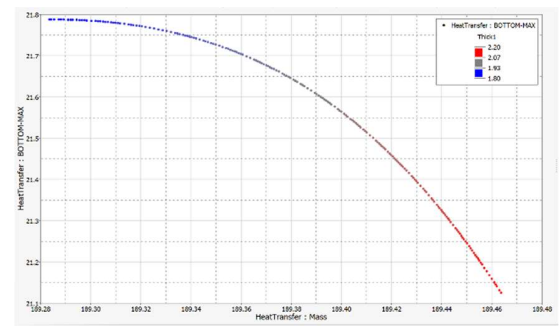
Figure 3.162 - Graphic of scatter points with X axis as the weight and Y axis as the average bottom temperature.

The variable was plotted on the same goal, to minimize weight and minimize the temperature on all outputs. With these experiments the optimization method applied was GRSM.

Geometry variables

Similarly to the variable of the thickness, two designs were paired for them to observe the behavior and consist of seven experiments with two runs and the fifth design was experimented on in a separate environment.

In the first iteration the value of the shape L1 was between 30 and 15, and the values chosen for the design of experiments using MELS.

The optimization on the thicknesses from the shape one and shape two gave scatter points where it was calculated via the mathematical model to have a result on each point, giving a reference on how the outputs of the model behave after increasing the thickness of the shell elements. In each graphic the X axis has the weight of the model.

It is crucial to indicate that in this variable it is not possible to indicate a correlation between the values of L1. The variable was plotted on the same goal, to minimize weight and minimize the temperature on all outputs. With these experiments the optimization method applied was GRSM. In the second iteration the value of the shapes L2 were between 3.5 and 17.5, and the values chosen for the design of experiments using MELS.

The optimization on the thicknesses from the shape L2 gave scatter points where it was calculated via the mathematical model to have a result on each point, giving a reference on how the outputs of the model behave after increasing the thickness of the shell elements. In each graphic the X axis has the weight of the model.

The resulting graphics of the L2 are:
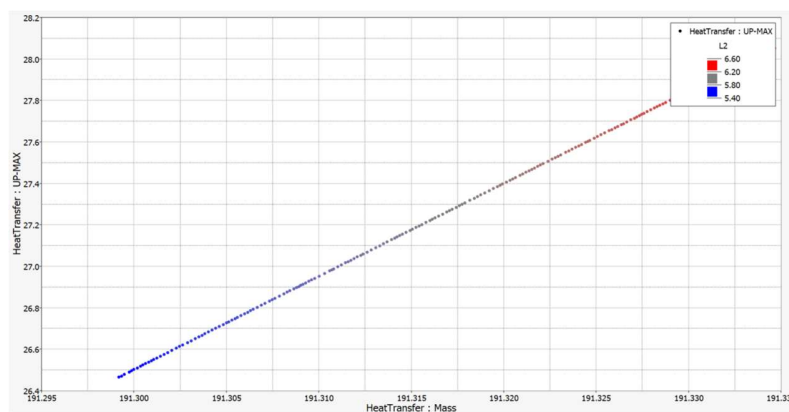
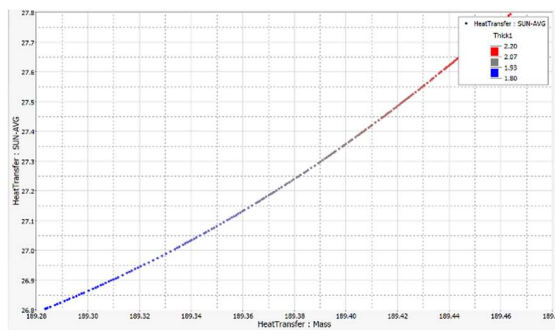Figure 3.163 – Graphic of scatter points with X axis as the weight and Y axis as the maximum upper cover temperature.
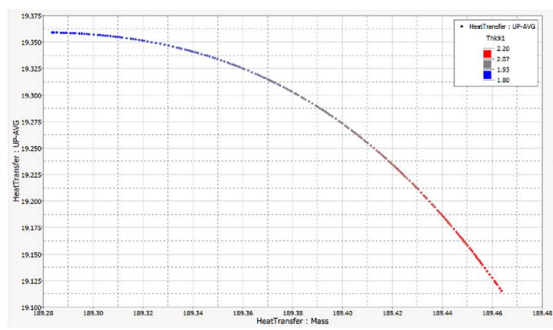
The variable was plotted on the same goal, to minimize weight and minimize the temperature on all outputs. With these experiments the optimization method applied was GRSM. In the third iteration the value of the shape P1 was between 7.5 and 25, and the values chosen for the design of experiments using MELS.

The optimization on the thicknesses from the shape one and shape two gave scatter points where it was calculated via the mathematical model to have a result on each point, giving a reference on how the outputs of the model behave after increasing the thickness of the shell elements. In each graphic the X axis has the weight of the model.

The resulting graphics of P1 are:
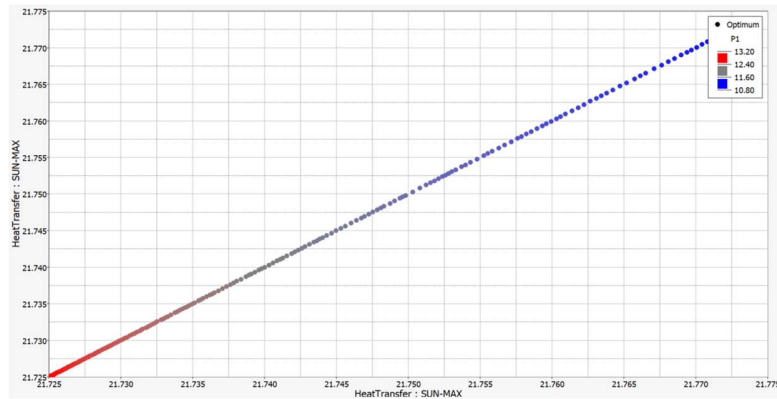
Figure 3.164 – Graphic of scatter points with X axis as the weight and Y axis as the maximum upper cover temperature.

It is crucial to indicate that in this variable it is not possible to indicate a correlation between the values of P1.

Both variables were plotted on the same goal, to minimize weight, maximize the internal energy approved on the model, reduce the kinetic energy on the model and reduce the acceleration on the central node. With these experiments the optimization method applied was GRSM.

For the first design the best output analysis was:

Table 3-54 – Results of optimal shapes on the first design of the pillars

L1	+1
L2	-1
P1	+1

Table 3-55 – Results of optimal thickness on the first design of the pillars

Thermal	1 mm

4. Result and discussion

This chapter summarizes the key findings from the design and optimization processes of battery housing. It evaluates these results concerning research objectives, focusing on safety, efficiency, and the integration of passive and active cooling systems. The findings also highlight the role of multidisciplinary methodologies, such as MDAO and FEA, in achieving the design goals.

The optimization and analysis of the battery housing components reveal notable advancements in safety, efficiency, and structural integrity. These findings validate the proposed designs and highlight the value of multidisciplinary approaches, such as MDAO and FEA, in achieving optimal performance. The implications of these results are discussed below, focusing on crash analysis, thermal performance, and broader design strategies.

Crash analysis of the battery housing system, comprising side panels, pillars, and external sheets, demonstrates the success of optimization strategies in improving energy management and structural integrity.

- **Side Panels:** Finite Element Analysis (FEA) conducted on the side panels highlights significant enhancements in energy absorption and kinetic energy dissipation. Design 3 emerged as the most effective, achieving the lowest resultant acceleration and X-Momentum values. This design ensures superior impact performance while reducing weight.

- **Pillars:** The addition of optimized pillars significantly enhanced crashworthiness by improving energy absorption and reducing force transfer to the structure. These features addressed areas previously lacking support, ensuring greater structural integrity and vehicle safety.

- **External Sheets:** External sheets demonstrated marked improvements in managing impact forces, outperforming the original design in energy absorption while protecting internal components.

4.1 Battery Housing Side Panel

The MDAO framework identified critical variables and optimal configurations for the battery housing side panels. Regression models provided accurate predictions, enabling the optimization of structural integrity and thermal performance.

FEA results summarized in Table 7.1 and the accompanying graphics illustrate performance improvements. Design 3 achieved the greatest energy absorption and dissipation capabilities, enhancing vehicle safety by reducing weight and improving energy management during impacts.

Table 4-1 - Table of results from analysis ran on RADIOSS

	Internal Energy	Masa	X-Momentum	central resultant accel	Kinetic Energy	TE-Total Energy	Resultant Acceleration
BHSP1	3.54E+08	848.10931	-7131606.5	0.058129	3.25E+10	3.28E+10	692003.88
BHSP2	1.86E+07	840.98547	-7143375.5	0.6215682	3.26E+10	3.26E+10	166617.06
BHSP3	3.63E+08	804.57257	-6750335.5	0.464238	3.08E+10	3.11E+10	103743.07

The comparative graphic illustrates the kinetic energy dissipation and internal energy absorption for each design. It provides a visual comparison of the performance improvements achieved by the optimized side panels compared to the original design.

The results confirm that the optimized battery housing side panel designs significantly outperform the original design. Design 3 is particularly effective, demonstrating the greatest energy absorption and dissipation capabilities. These improvements enhance the overall safety and efficiency of the vehicle by effectively reducing weight and increasing energy management during impacts.

The graphical analysis complements the numerical data by providing a clear and immediate comparison, supporting the conclusion that the proposed designs offer superior performance over the original benchmark. This analysis provides valuable insights for future iterations of the battery housing design.
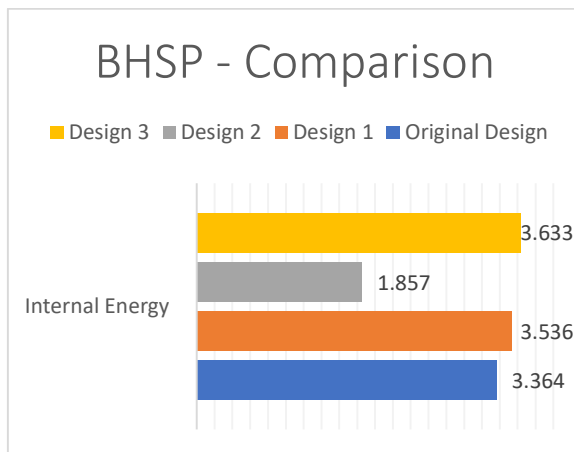
Figure 4.1 – Graphic comparing the internal energy con the original design and the proposed designs
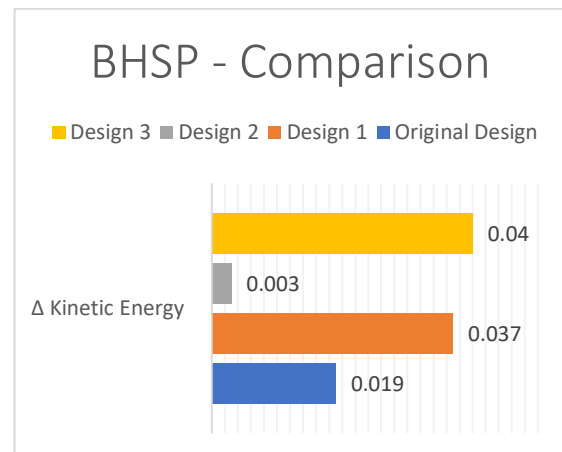
Figure 4.2 - Graphic comparing the kinetic energy con the original design and the proposed designs

In addition to kinetic energy dissipation and internal energy absorption, several key performance metrics provide further insight into the effectiveness of the proposed battery housing side panel designs. X-Momentum (MAG) reflects the momentum change during impact, where Design 3 exhibits the lowest value, indicating improved energy management and structural efficiency. The resultant acceleration values (both central and resultant) highlight the ability of the designs to control dynamic forces; Design 3 achieves the lowest acceleration magnitudes, suggesting superior energy distribution and reduced stress on the structure. Similarly, the total energy (TE - MAG) values confirm the effective dissipation of energy during impact, with Design 3 demonstrating the most significant reduction compared to the original benchmark. These additional metrics underscore the optimized designs' potential to enhance vehicle safety, improve energy management, and contribute to overall performance advancements.
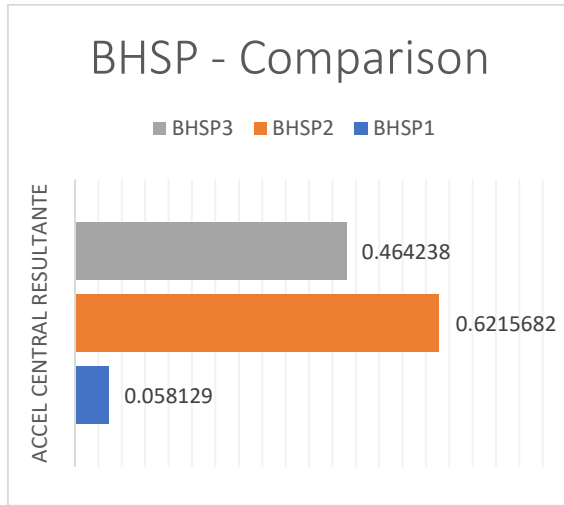
Figure 4.3 - Graphic comparing the resultant acceleration on the proposed designs
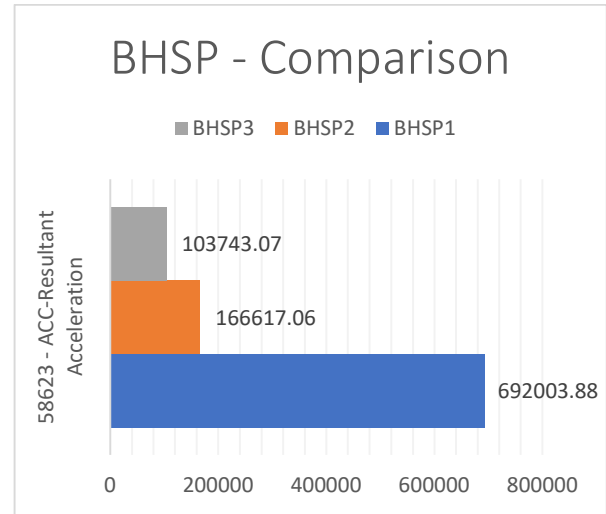
Figure 4.4 - Graphic comparing the resultant acceleration on node 58623 of the proposed designs

4.2 Pillar

To validate the optimization results for the battery housing pillars finite element analysis (FEA) was conducted using the same setup as the original design benchmark. In this case, the original design does not have pillars for energy absorption, this improves significantly the energy absorbed in the general result.

For the pillars, FEA demonstrated significant energy absorption improvements. The results confirm that adding optimized pillars enhances safety and efficiency. These findings provide strategies for reducing weight while improving structural integrity. The results are summarized in the table below and visualized in the accompanying comparative graphic for better clarity:

Table 4-2 - Table of results on the proposed designs of pillars

	Internal Energy - MAG	Kinetic Energy - MAG	Mass - MAG	Contact energy - MAG	TE-Total Energy - MAG	AX-X Acceleration	ACC-Resultant Acceleration
P2	9.40E+08	3.23E+10	858.48462	3.48E+07	9.98E+11	-8435.5234	8438.5449
P1	9.33E+08	3.25E+10	862.09937	3.70E+07	1.00E+12	-2425.1401	2435.3486

192
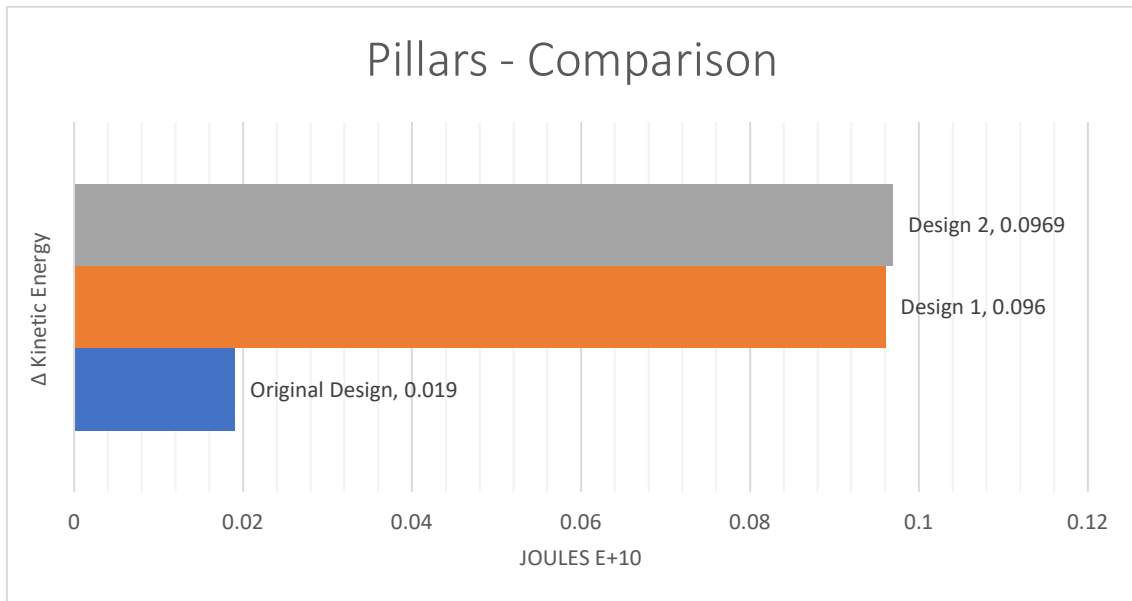
Figure 4.5 - Graphic comparing the kinetic energy con the original design and the proposed designs

These findings provide a deeper understanding of the behavior of the battery housing pillar designs and validate the optimization process as effective in achieving safety and efficiency goals. Furthermore, the results contribute to future iterations by identifying strategies to reduce weight while enhancing vehicle safety.
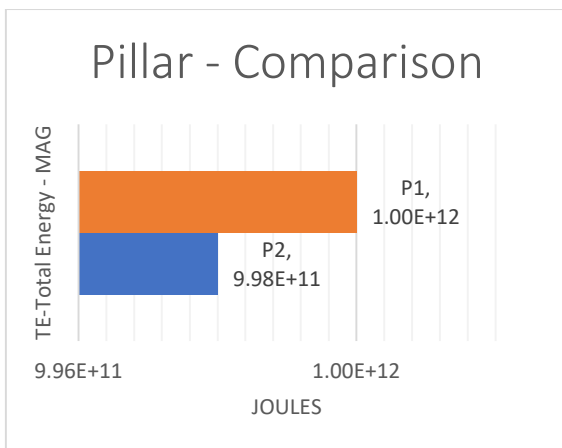
Figure 4.6 - Graphic comparing the total energy con the original design and the proposed designs
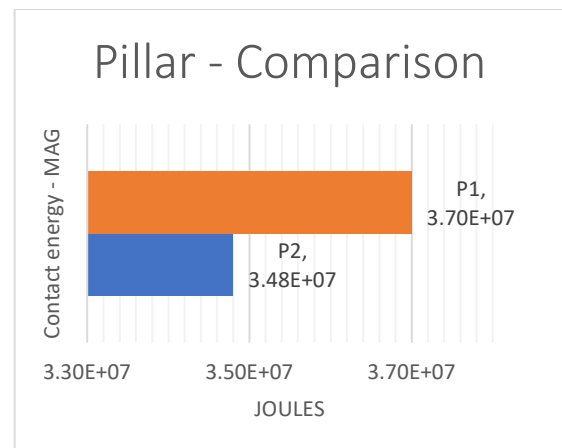
Figure 4.7 - Graphic comparing the contact energy con the original design and the proposed designs
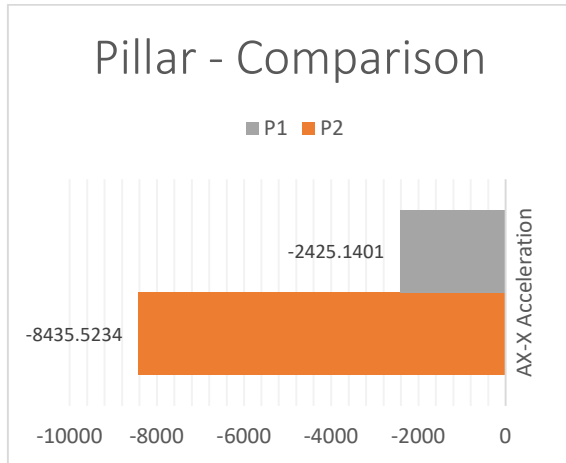
Figure 4.8 - Graphic comparing the acceleration on AX-X con the original design and the proposed designs
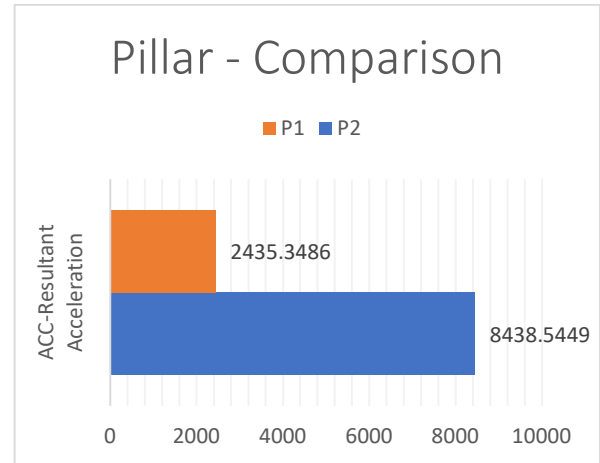
Figure 4.9 - Graphic comparing the resultant acceleration con the original design and the proposed designs

4.3 External Sheet

To validate the optimization results for the battery housing upper and lower cover finite element analysis (FEA) conducted using the same setup as the original design benchmark. In this case, just one design is proposed. The results are summarized in the table below and visualized in the accompanying comparative graphics for better clarity:

Table 4-3 - Table of results on the proposed designs

	Internal Energy – MAG (Joules)	Kinetic Energy – MAG (Joules)
Original design	1.03E+09	3.32E+10
Design 1	3.36E+10	3.33E+10
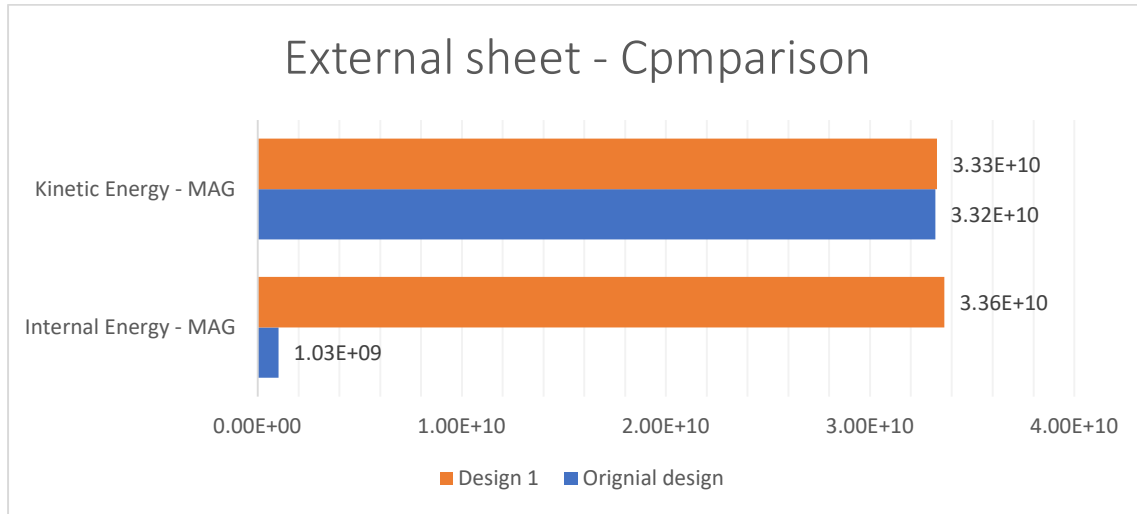
Figure 4.10 - Graphic comparing the kinetic and internal energy con the original design and the proposed designs

4.4 General

The general result of the crash simulation was archived selecting the optimized designs and selecting the most capable to improve the protection of the vehicle, this implies that a selection of the side panel, pillars and the design in the upper and lower cover with the optimized geometry variables as well as their thickness.

The results can be shown in the next graphics:
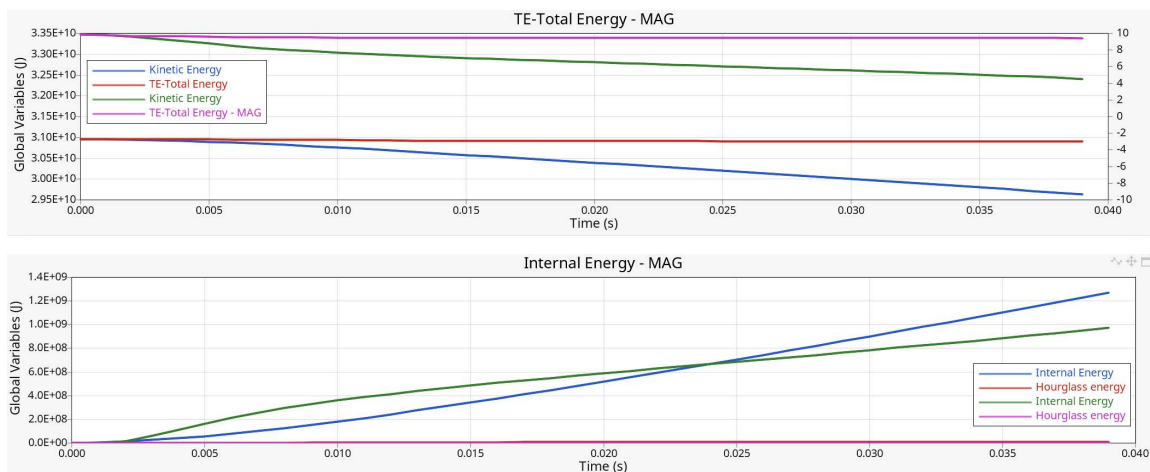
Figure 4.11 - Comparing graphics on the original and proposed integrated designs in internal and kinetic energy

The first graphic presents the results on the analysis on the original design, in this case the original design having the lines in green and magenta, along with the best design and

optimized all the proposed parts. The second graphic represents the internal energy absorption along the time in the simulation that the time .024 s the proposed design improves more than the original and it will improve along the time of the simulation.

The kinetic energy decreased by 36% in the proposed design in comparison to the original as well as the internal energy increased by 31% with only the increase of 36% in the weight or 48.5 kg.

4.5 Thermal

Thermal analysis validated the optimized design, achieving a balance between weight and thermal protection. These improvements ensure battery longevity and reliability while meeting stringent manufacturer requirements. The optimized design achieved thermal performance with only a 2% weight increase.

4.6 Broader Implications and Integration

The integration of optimized geometries, materials, and thicknesses highlights the success of a holistic design approach. Regression models within the MDAO framework enabled accurate predictions without extensive corroboration, demonstrating MDAO's potential as a trusted tool for advanced engineering design. This methodology provides a scalable framework for optimizing other vehicle components, advancing safer and more efficient electric vehicles.

5. Conclusions

This study successfully demonstrates the impact of multidisciplinary design and optimization methods on the development of battery housing systems for electric vehicles. By utilizing MDAO and FEA, significant improvements were made in safety, efficiency, and structural integrity, addressing the critical needs of modern automotive design.

The crash analysis revealed that the optimized side panels, pillars, and external sheets notably enhanced energy absorption and dissipation. Design 3 of the side panels proved most effective, exhibiting superior kinetic energy management and reducing structural stress, while the addition of optimized pillars significantly improved crashworthiness. The external sheets also provided better protection for internal components, enhancing overall vehicle safety.

Thermal analysis further validated the design, striking a balance between weight and thermal protection. The slight increase in weight required to meet thermal performance standards was justified by the improved battery reliability and longevity, ensuring compliance with stringent manufacturer requirements.

The integration of optimized geometries, materials, and thicknesses underscores the success of a holistic design approach. By utilizing mathematical regression models within the MDAO framework, the study demonstrated the accuracy and efficiency of this methodology, reducing the need for extensive physical validation and making it a reliable tool for future engineering designs.

This research not only advances battery housing design but also offers a scalable framework for optimizing other vehicle components. The results contribute to the broader goals of enhancing electric vehicle safety, performance, and sustainability, with promising potential for further applications in the automotive industry.

In conclusion, the study validates the effectiveness of optimization techniques in improving vehicle safety, thermal performance, and energy efficiency, paving the way for future innovations in electric vehicle design.

This work contributes scientifically by demonstrating the effectiveness of MDAO in predicting and optimizing crash and thermal performance, and technologically by delivering

a validated, lightweight, and structurally enhanced battery housing system that integrates passive and active safety improvements for electric vehicles.

6. Bibliography

[1]   B. Foley, K. Degirmenci, and T. Yigitcanlar, "Factors Affecting Electric Vehicle Uptake: Insights from a Descriptive Analysis in Australia," *Urban Science*, vol. 4, no. 4, p. 57, Nov. 2020, doi: 10.3390/urbansci4040057.

[2]   "Audi e-tron vs Jaguar I-PACE battery pack comparison – Electric Revs." Accessed: Nov. 15, 2023. [Online]. Available: https://electricrevs.com/2018/04/21/audi-e-tron-vs-jaguar-i-pace-battery-pack-comparison/

[3]   "Chevy Volt battery pack: Rugged but precise | CompositesWorld." Accessed: Nov. 15, 2023. [Online]. Available: https://www.compositesworld.com/articles/chevy-volt-battery-pack-rugged-but-precise

[4]   "Tesla 5.2kWh Battery Module – Legacy EV." Accessed: Nov. 15, 2023. [Online]. Available: https://legacyev.com/products/49

[5]   J. Tian, R. Xiong, W. Shen, and J. Lu, "State-of-charge estimation of LiFePO4 batteries in electric vehicles: A deep-learning enabled approach," *Appl Energy*, vol. 291, Jun. 2021, doi: 10.1016/j.apenergy.2021.116812.

[6]   M. Brenna, F. Foiadelli, C. Leone, and M. Longo, "Electric Vehicles Charging Technology Review and Optimal Size Estimation," *Journal of Electrical Engineering and Technology*, vol. 15, no. 6, pp. 2539–2552, Nov. 2020, doi: 10.1007/s42835-020-00547-x.

[7]   A. Pesaran Andreas Vlahinos, D. Bharathan, T. Duong, and F. Lauderdale, "Electrothermal Analysis of Lithium Ion Batteries THE 23rd INTERNATIONAL BATTERY SEMINAR & EXHIBIT," 2006.

[8]   S. Huang *et al.*, "In Situ Measurement of Lithium-Ion Cell Internal Temperatures during Extreme Fast Charging," *J Electrochem Soc*, vol. 166, no. 14, pp. A3254–A3259, 2019, doi: 10.1149/2.0441914jes.

[9]   "4680 Battery: Everything You Need to Know About These New Cells - History-Computer." Accessed: Nov. 15, 2023. [Online]. Available: https://history-computer.com/4680-battery-cells/

[10]   "Charged EVs | Audi and Umicore test closed-loop process for recycling EV batteries - Charged EVs." Accessed: Nov. 15, 2023. [Online]. Available: https://chargedevs.com/newswire/audi-and-umicore-tests-closed-loop-process-for-recycling-ev-batteries/

[11]   P. Sun, R. Bisschop, H. Niu, and X. Huang, "A Review of Battery Fires in Electric Vehicles," Jul. 01, 2020, *Springer*. doi: 10.1007/s10694-019-00944-3.

[12]   X. M. Pham, G. Van Bui, H. Pham, and L. H. P. Pham, "Design Process of Electric Vehicle Power System," *Applied Mechanics and Materials*, vol. 907, pp. 101–114, Jun. 2022, doi: 10.4028/p-vkvz26.

[13]   "Tesla Model 3 side pole impact - YouTube." Accessed: Nov. 15, 2023. [Online]. Available: https://www.youtube.com/watch?v=BLxk9l9PhX8

[14]   "Examining the New 2022 Audi Q4 e-tron's Powertrains and the Tech Behind Them - autoevolution." Accessed: Nov. 15, 2023. [Online]. Available: https://www.autoevolution.com/news/examining-the-new-2022-audi-q4-e-trons-powertrains-and-the-tech-behind-them-159627.html

[15]   "First Body-in-White Made from Composites for a Chinese Electric Car." [Online]. Available: www.springerprofessional.com/automotive

[16] P. R. Tete, M. M. Gupta, and S. S. Joshi, "Developments in battery thermal management systems for electric vehicles: A technical review," Mar. 01, 2021, *Elsevier Ltd*. doi: 10.1016/j.est.2021.102255.

[17] X. Tang, R. Bonner, T. Desai, and A. Fan, "A 2-D numerical study of microscale phase change material thermal storage for GaN transistor thermal management," in *Annual IEEE Semiconductor Thermal Measurement and Management Symposium*, 2011, pp. 27–34. doi: 10.1109/STHERM.2011.5767174.

[18] S. Zhang *et al.*, "A review of phase change heat transfer in shape-stabilized phase change materials (ss-PCMs) based on porous supports for thermal energy storage," Jan. 01, 2021, *Elsevier Ltd*. doi: 10.1016/j.rser.2020.110127.

[19] J. Chen, Z. Wang, and A. M. Korsunsky, "A numerical study of the effect of discretization methods on the crystal plasticity finite element method."

[20] A. K. M. N. Mehdy, M. D. Ekstrand, B. P. Knijnenburg, and H. Mehrpouyan, "Privacy as a planned behavior: Effects of situational factors on privacy perceptions and plans," in *UMAP 2021 - Proceedings of the 29th ACM Conference on User Modeling, Adaptation and Personalization*, Association for Computing Machinery, Inc, Jun. 2021, pp. 169–178. doi: 10.1145/3450613.3456829.

[21] T. F. Varley, "Causal Emergence in Discrete and Continuous Dynamical Systems," Mar. 2020, [Online]. Available: http://arxiv.org/abs/2003.13075

[22] R. E. Meethal *et al.*, "Finite element method-enhanced neural network for forward and inverse problems," *Adv Model Simul Eng Sci*, vol. 10, no. 1, Dec. 2023, doi: 10.1186/s40323-023-00243-1.

[23] F. Han and Z. Li, "A peridynamics-based finite element method for quasi-static fracture analysis," Sep. 2021, [Online]. Available: http://arxiv.org/abs/2109.11099

[24] H. Fu, "A characteristic finite element method for optimal control problems governed by convectiondiffusion equations," *J Comput Appl Math*, vol. 235, no. 3, pp. 825–836, Dec. 2010, doi: 10.1016/j.cam.2010.07.010.

[25] C. Zhang, S. An, W. Wang, and D. Lin, "A novel meshing method based on adaptive size function and moving mesh for electromagnetic finite element analysis," *Symmetry (Basel)*, vol. 13, no. 2, pp. 1–16, Feb. 2021, doi: 10.3390/sym13020254.

[26] J. Rowbottom *et al.*, "G-Adaptive mesh refinement -- leveraging graph neural networks and differentiable finite element solvers," Jul. 2024, [Online]. Available: http://arxiv.org/abs/2407.04516

[27] H. Xu, Z. Nie, Q. Xu, and X. Liu, "SuperMeshing: A Novel Method for Boosting the Mesh Density in Numerical Computation within 2D Domain," Mar. 2021, [Online]. Available: http://arxiv.org/abs/2104.01138

[28] L. Lévesque, "Law of cooling, heat conduction and Stefan-Boltzmann radiation laws fitted to experimental data for bones irradiated by CO2 laser," *Biomed Opt Express*, vol. 5, no. 3, p. 701, Mar. 2014, doi: 10.1364/boe.5.000701.

[29] H. S. Lima, C. Tsallis, D. Eroglu, and U. Tirnakli, "Fourier's law breakdown for the planar-rotor chain with long-range coupling," Jul. 2024, [Online]. Available: http://arxiv.org/abs/2407.13843

[30] G. Gadzirayi Nyambuya and G. G. Nyambuya, "On the Fundamental Theoretical Foundations of Newton's Law of Cooling." [Online]. Available: https://www.researchgate.net/publication/316158763

[31]   A. F. Santos, S. C. Ulhoa, and F. C. Khanna, "On Stefan-Boltzmann law and the Casimir effect at finite temperature in the Schwarzschild spacetime," Apr. 2020, doi: 10.1142/S0217751X20500669.

[32]   F. J. Abellán, J. A. Ibáñez, R. P. Valerdi, and J. A. García, "The Stefan-Boltzmann constant obtained from the I-V curve of a bulb," *Eur J Phys*, vol. 34, no. 5, pp. 1221–1226, 2013, doi: 10.1088/0143-0807/34/5/1221.

[33]   K. Ozeritskiy and A. Gunar, "Understanding the influence of boundary conditions and thermophysical soil parameters on thermal modelling in permafrost regions." [Online]. Available: https://www.researchgate.net/publication/374843228

[34]   P. K. Kythe and D. Wei, *An Introduction to Linear and Nonlinear Finite Element Analysis*. Birkhäuser Boston, 2004. doi: 10.1007/978-0-8176-8160-9.

[35]   M. B. Wakchaure, M. Misra, and P. L. Menezes, "A Comprehensive Review on Finite Element Analysis of Laser Shock Peening," Sep. 01, 2024, *Multidisciplinary Digital Publishing Institute (MDPI)*. doi: 10.3390/ma17174174.

[36]   B. Dhas, J. Kumar, D. Roy, and J. N. Reddy, "A mixed method for 3D nonlinear elasticity using finite element exterior calculus," Aug. 2021, [Online]. Available: http://arxiv.org/abs/2109.01491

[37]   T. Xu, K. Wang, and S. Song, "Measurement uncertainty and representation of tensile mechanical properties in metals," Nov. 01, 2021, *MDPI*. doi: 10.3390/met11111733.

[38]   T. Takayama and Y. Nagasawa, "Poisson's Ratio Prediction of Injection Molded Thermoplastics Using Differential Scanning Calorimetry," *Polymers (Basel)*, vol. 16, no. 14, Jul. 2024, doi: 10.3390/polym16141956.

[39]   "6 Linear Elasticity."

[40]   O. M. Elmardi and S. Khayal, "The Importance of Studying Mechanical Properties of Engineering Materials", doi: 10.13140/RG.2.2.22654.60489.

[41]   Z. Chen, H. J. Bong, D. Li, and R. H. Wagoner, "Elastic-plastic transition: A universal law", doi: 10.1051/matecconf/201.

[42]   D. Roylance, "STRESS-STRAIN CURVES," 2001.

[43]   D. Gonfa Tolasa, "Hooke's Law Through Experimental Analysis", doi: 10.13140/RG.2.2.12119.89762.

[44]   M. T. Islam, S. Tang, C. Liverani, S. Saha, E. Tasciotti, and R. Righetti, "Non-invasive imaging of Young's modulus and Poisson's ratio in cancers in vivo," *Sci Rep*, vol. 10, no. 1, Dec. 2020, doi: 10.1038/s41598-020-64162-6.

[45]   "Chapter 26 Elastic Properties of Materials."

[46]   "Linear elasticity."

[47]   B. Review and J. D. Achenbach, "Journal of Applied Mechanics," 2014. [Online]. Available: http://asmedigitalcollection.asme.org/appliedmechanics/article-pdf/81/4/046501/6079724/jam_81_04_046501.pdf

[48]   M. A. Meyers and K. K. Chawla, "Mechanical Behavior of," 2005.

[49]   R. Cypher, F. M. A. Der Heide, C. Scheideier, and B. Vöcking, "Universal algorithms for store-and-forward and wormhole routing," in *Proceedings of the Annual ACM Symposium on Theory of Computing*, Association for Computing Machinery, Jul. 1996, pp. 356–365. doi: 10.1145/237814.237982.

[50]   M. Y. Kumar and M. V. R. Reddy, "Structural & Thermal Analysis of Different Materials of Steam Turbine Blade Shaft using Finite Element Methods," in *AIP Conference Proceedings*, American Institute of Physics Inc., Nov. 2022. doi: 10.1063/5.0114558.

[51] T. Huang, M. Wang, S. Feng, Z. Peng, X. Huang, and Y. Song, "Study on the Coupled Heat Transfer of Conduction, Convection, and Radiation in Foam Concrete Based on a Microstructure Numerical Model," *Buildings*, vol. 14, no. 5, May 2024, doi: 10.3390/buildings14051287.

[52] A. Kumar[1], A. Sharma, and A. Kumar, "Advances in Heat Transfer Mechanisms: A Comprehensive Review," vol. 1, p. 339, doi: 10.48047/nq.2021.19.1.NQ21045.

[53] Sd. Barathi, Ig. Valdharis, and A. professor, "STRUCTURAL AND THERMAL ANALYSIS OF STEAM TURBINE BLADES USING FEM," *IJRAR23A1569 International Journal of Research and Analytical Reviews*, 2023, [Online]. Available: www.ijrar.org

[54] P. Kale, S. Deshkhaire, S. Gurjar, I. Sadamate, and P. Yadav, "Thermal Analysis of Steam Turbine Blade," 2023. [Online]. Available: www.ijres.org

[55] K. Adithya *et al.*, "Structural and Thermal Research of Steam Turbine Blades by Finite Element Method," *International Journal of Innovative Technology and Exploring Engineering*, vol. 9, no. 5, pp. 2275–2278, Mar. 2020, doi: 10.35940/ijitee.E2495.039520.

[56] S. Q. Miao, H. P. Li, and G. Chen, "Temperature dependence of thermal diffusivity, specific heat capacity, and thermal conductivity for several types of rocks," *J Therm Anal Calorim*, vol. 115, no. 2, pp. 1057–1063, Feb. 2014, doi: 10.1007/s10973-013-3427-2.

[57] M. K. Howlader, M. H. Rashid, and T. Haque, "Effects of aggregate types on thermal properties of concrete," 2012. [Online]. Available: https://www.researchgate.net/publication/287467364

[58] K. Chen, L. Fan, Z. Hu, and Y. Xu, "Dual-phase-lag heat conduction analysis of a three-dimensional finite medium heated by a moving laser beam with circular or annular cross-section," Aug. 2023, [Online]. Available: http://arxiv.org/abs/2308.02532

[59] T. Huang, M. Wang, S. Feng, Z. Peng, X. Huang, and Y. Song, "Study on the Coupled Heat Transfer of Conduction, Convection, and Radiation in Foam Concrete Based on a Microstructure Numerical Model," *Buildings*, vol. 14, no. 5, May 2024, doi: 10.3390/buildings14051287.

[60] L. Sun, R. Diao, F. Yang, and B. Lin, "Analysis of the Thermal Performance of the Embedded Composite Phase Change Energy Storage Wall," *ACS Omega*, vol. 5, no. 28, pp. 17005–17021, Jul. 2020, doi: 10.1021/acsomega.9b04128.

[61] A. Alsakarneh, T. Tabaza, G. Kelly, and J. Barrett, "Impact Dynamics of Nonlinear Materials: FE Analysis," *Journal of Applied and Computational Mechanics*, vol. 9, no. 3, pp. 728–738, 2023, doi: 10.22055/jacm.2022.41487.3760.

[62] R. Lakshminarayanan, "CAE Simulation of Non-Linear Analysis-Modeling of Material Model using Isotropic Material Hardening Law Simulation of Non-Linear Analysis in ANSYS," 2014, doi: 10.13140/2.1.1202.8167.

[63] Y. S. Kong, M. Z. Omar, L. B. Chua, and S. Abdullah, "Explicit nonlinear finite element geometric analysis of parabolic leaf springs under various loads," *The Scientific World Journal*, vol. 2013, 2013, doi: 10.1155/2013/261926.

[64] M. Fragiadakis, "Response Spectrum Analysis of Structures Subjected to Seismic Actions," in *Encyclopedia of Earthquake Engineering*, Springer Berlin Heidelberg, 2013, pp. 1–18. doi: 10.1007/978-3-642-36197-5_133-1.

[65]   S. Jayaraman, M. Trikha, Somashekar, D. Kamesh, and M. Ravindra, "Response Spectrum Analysis of Printed Circuit Boards Subjected to Shock Loads," *Procedia Eng*, vol. 144, pp. 1469–1476, 2016, doi: 10.1016/j.proeng.2016.06.710.

[66]   J. Guerrero and J. H. Muñoz, "Revisiting the Newton's second law and Lagrange's equations in orthogonal curvilinear coordinates: some remarks." [Online]. Available: https://www.researchgate.net/publication/344456087

[67]   J. E. Moran and D. S. Weaver, "On the damping in tube arrays subjected to two-phase cross-flow," *Journal of Pressure Vessel Technology, Transactions of the ASME*, vol. 135, no. 3, 2013, doi: 10.1115/1.4023421.

[68]   F. Mostafa Amin *et al.*, "Stability Analysis of Ubiquitous Direct Time Integration Methods www.ijser.in Licensed Under Creative Commons Attribution CC BY Stability Analysis of Ubiquitous Direct Time Integration Methods," vol. 7, no. 5, 2018, [Online]. Available: https://www.researchgate.net/publication/333176231

[69]   C. Yang, B. zhu Yang, T. Zhu, and S. ne Xiao, "Comparison and assessment of time integration algorithms for nonlinear vibration systems," *J Cent South Univ*, vol. 24, no. 5, pp. 1090–1097, May 2017, doi: 10.1007/s11771-017-3512-y.

[70]   M. Bello, A. A. Adedeji, M. Bello, A. A. Adedeji, R. O. Rahmon, and M. A. Kamal, "Dynamic Analysis of Multi-Storey Building under Seismic Excitation by Response Spectrum Method using ETABS," 2017. [Online]. Available: https://www.researchgate.net/publication/323153920

[71]   Y. Zeng, S. Ding, J. Xu, Q. Hu, and X. Cui, "Dynamic Analysis of Percussion Drilling System under Harmonic Impact," *Shock and Vibration*, vol. 2021, 2021, doi: 10.1155/2021/8892144.

[72]   S. E. Abdel Raheem and T. Hayashikawa, "Parametric study on steel tower seismic response of cable-stayed bridges under great earthquake ground motion," *Structural Engineering/Earthquake Engineering*, vol. 20, no. 1, 2003, doi: 10.2208/jsceseee.20.25s.

[73]   Q. Meng, K. Zhong, and M. Sun, "Dynamic Response Analysis of Airport Pavement under Impact Loading," *Applied Sciences (Switzerland)*, vol. 13, no. 9, May 2023, doi: 10.3390/app13095723.

[74]   Z. Qiao, D. Xiaochang, and T. Wei, "An adaptive random experiment design method for engineering experiment."

[75]   S. Kucherenko, A. Saltelli, and D. Albrecht, "Exploring multi-dimensional spaces: a Comparison of Latin Hypercube and Quasi Monte Carlo Sampling Techniques," 2015. [Online]. Available: https://www.researchgate.net/publication/276210905

[76]   G. F. N. Gonçalves *et al.*, "Data-driven surrogate modeling and benchmarking for process equipment," *Data-Centric Engineering*, vol. 1, no. 5, Sep. 2020, doi: 10.1017/dce.2020.8.

[77]   E. H. Gürkan, Y. Tibet, and S. Çoruh, "Application of full factorial design method for optimization of heavy metal release from lead smelting slag," *Sustainability (Switzerland)*, vol. 13, no. 9, May 2021, doi: 10.3390/su13094890.

[78]   S. Bhattacharya, K. Kalita, R. Čep, and S. Chakraborty, "A comparative analysis on prediction performance of regression models during machining of composite materials," *Materials*, vol. 14, no. 21, Nov. 2021, doi: 10.3390/ma14216689.

[79]   H. Shi, X. Zhang, Y. Gao, S. Wang, and Y. Ning, "Robust Total Least Squares Estimation Method for Uncertain Linear Regression Model," *Mathematics*, vol. 11, no. 20, Oct. 2023, doi: 10.3390/math11204354.

[80] W. Y. Tey, N. A. C. Sidik, Y. Asako, M. W. Muhieldeen, and O. Afshar, "Moving Least Squares Method and its Improvement: A Concise Review," *Journal of Applied and Computational Mechanics*, vol. 7, no. 2, pp. 883–889, Mar. 2021, doi: 10.22055/jacm.2021.35435.2652.

[81] X. Shi, Y. Wang, H. Wu, and A. Wang, "A hybrid sparrow optimization Kriging model and its application in geological modeling," *Sci Rep*, vol. 14, no. 1, p. 24610, Dec. 2024, doi: 10.1038/s41598-024-75347-8.

[82] C. Groth, S. Porziani, and M. E. Biancolini, "Radial basis functions vector fields interpolation for complex fluid structure interaction problems," *Fluids*, vol. 6, no. 9, Sep. 2021, doi: 10.3390/fluids6090314.

[83] "Introduction into Fit Approximations with Altair HyperStudy TM eBook / Introduction into Fit Approximations with Altair HyperStudy TM."

[84] D. J. Pate, J. Gray, and B. J. German, "A graph theoretic approach to problem formulation for multidisciplinary design analysis and optimization," *Structural and Multidisciplinary Optimization*, vol. 49, no. 5, pp. 743–760, 2014, doi: 10.1007/s00158-013-1006-6.

[85] C. M. Heath and J. S. Gray, "OpenMDAO: Framework for flexible multidisciplinary design, analysis and optimization methods," in *Collection of Technical Papers - AIAA/ASME/ASCE/AHS/ASC Structures, Structural Dynamics and Materials Conference*, American Institute of Aeronautics and Astronautics Inc., 2012. doi: 10.2514/6.2012-1673.

[86] J. Gray, K. T. Moore, T. A. Hearn, and B. A. Naylor, "A standard platform for testing and comparison of MDAO architectures," in *53rd AIAA/ASME/ASCE/AHS/ASC Structures, Structural Dynamics and Materials Conference 2012*, American Institute of Aeronautics and Astronautics Inc., 2012. doi: 10.2514/6.2012-1586.

[87] D. Meng *et al.*, "Multidisciplinary design optimization of engineering systems under uncertainty: a review," *International Journal of Structural Integrity*, vol. 13, no. 4, pp. 565–593, Jul. 2022, doi: 10.1108/IJSI-05-2022-0076.

[88] D. Meng *et al.*, "Multidisciplinary design optimization of engineering systems under uncertainty: a review," *International Journal of Structural Integrity*, vol. 13, no. 4, pp. 565–593, Jul. 2022, doi: 10.1108/IJSI-05-2022-0076.